Terahertz Fibres and Functional Fibrel-Based Devices

Bao, Hualong; Bang, Ole; Jepsen, Peter Uhd

Publication date:
2014

Document Version
Publisher's PDF, also known as Version of record

Department of Photonics Engineering
Technical University of Denmark

TERAHERTZ FIBRES AND FUNCTIONAL FIBRE-BASED DEVICES

by

Hualong Bao

November 2014

Abstract

The area of Terahertz (THz) radiation has been proved to be a very promising utility for a wide range of applications. However, since current THz systems predominantly utilize free-space propagation, the large size and requirement of careful alignment thus increasing the complexity are the drawbacks on using such systems. Consequently, it is in urgent need to develop waveguides/devices, similar with the fiber waveguides in infrared region, in THz region, which holds great promise for driving this technology further. In this thesis, we have investigated several different dielectric waveguides/devices that rely on different wave-guiding mechanisms to guide THz radiation.

We first focus on Photonic bandgap gap (PBG) THz fibers. To overcome the fabrication problems of traditional PBG type fibers, which caused by the imbalance of hole dimensions, we investigate a novel porous-core honeycomb bandgap type THz fiber. The fabrication and experimental characterization of such a PBG THz fiber are also performed. The fiber is made of polymer TOPAS and confirm that it allows to fabricate long lengths of fiber with a near-perfect periodic structure and thus very clear bandgap guidance. The fundamental bandgap at 0.75-1.05 THz is found to have losses lower than 1.5 dB/cm, whereas the loss is below 1.0 dB/cm in the reduced bandgap 0.78-1.02 THz. The particular fiber we present has an outer diameter of 3.65 mm, and is thus already flexible. The outer diameter can be further reduced and thus these fibers may also be bent and cleaved.

We then focus on tube waveguides. Three different methods are used to improve the transmission bandwidth and dispersion properties, while the propagation loss can be kept generally low. The first way is to deliberately introduce high material absorption to the cladding material, thus efficiently removing the interfering fields that bounce through the cladding and back into the core in a traditional low-loss ARROW tube waveguide. The same effect has been obtained by adding a thin layer of a suitable absorber around the tube surface, here exemplified with water. We also designed and demonstrated another kind of tube waveguides consist of a uniform air-core and a cladding layer with tapered thickness.

Results show that the same effect of the highly absorbing cladding material tube waveguides can also be obtained, thus breaking the cladding material limitation.

Finally, we investigate a special design of a broadband THz fiber directional coupler, which uses mechanical down-doping of the two cores. We show how the proposed coupler provides a broad bandwidth with relative low device loss and perform detailed optimizations of the coupler design to maximize bandwidth and minimize loss. Optimum parameters have been found. Moreover, we verify that the optimum coupler is single-moded and we investigate the robustness of its performance to structural changes.

Resume

Området omkring terahertz (THz) stråling har vist sig at være et meget lovende værktøj til en bred vifte af applikationer. Men da nuværende THz systemer primært bevæger sig i frit rum, giver det store krav til størrelsen og nøjagtig kalibrering. Der er derfor et presserende behov for at udvikle bølgeledere/udstyr, lignende fiberbølgeledere i det infrarøde område, i THz-området, hvilket vil være afgørende for at drive denne teknologi videre. I denne afhandling har vi undersøgt flere forskellige dielektriske bølgeledere/enheder, der benytter forskellige bølgeledende mekanismer til at guide THz-stråling.

Vi fokuserer først på fotoniske båndgab (PBG) THz fibre. For at overvinde de traditionelle fabrikationsproblemer med PBG type fibre, som skyldes forskelligheder i huldimensionerne, undersøger vi en ny porøs-kerne bikube båndgabs THz fiber. Fremstillingen og eksperimentel karakterisering af et sådant PBG THz fiber udføres også. Fiberen er fremstillet af polymer TOPAS og viser, at det er muligt at fremstille lange fibre med en næsten perfekt periodisk struktur og dermed meget klart båndgab bølgeledning. Det fundamentelle båndgab på 0,75-1,05 THz viser sig at have tab på mindre end 1,5 dB/cm, mens tabet er under 1,0 dB/cm i det reducerede båndgab omkring 0,78-1,02 THz. Denne fiber har en ydre diameter på 3,65 mm, og er således allerede fleksibel. Den ydre diameter kan reduceres yderligere, og sådanne fibre kan også bøjes og spaltes.

Som det næste fokuserer vi på rørbølgeledere. Tre forskellige metoder benyttes til at forbedre transmissionsbåndbredden og dispersionsegenskaberne, mens udbredelsestabet kan holdes på et lavt niveau. Den første måde er ved bevidst at introducere et materiale med høj absorption i kappen, således at de interfererende felter, der hopper mellem kernen og ud i kappen, effektivt fjernes, som i en lav-tabs ARROW rørbølgeleder. En lignende virkning er opnået ved tilsætning af et tyndt lag af en egnet absorber omkring røret, i dette tilfælde vand. Vi har også designet og demonstreret en anden type af rørbølgeledere bestående af en ensartet luftkerne og et kappelag med konisk tykkelse. Resultaterne viser,

at den samme effekt som sås ved den stærkt absorberende kappe også kan opnås her, og derved kan begrænsningen ved kappematerialet undgås.

Endelig undersøger vi et specielt design af en bredbånds retningsbestemt THz kobler, som benytter mekanisk ned-doping af de to kerner. Vi viser, hvordan den foreslåede kobler giver en stor båndbredde med et lille koblingstab og udfører detaljerede optimeringer af koblerens design for at maksimere båndbredden og minimere tabet. Optimale parametre er blevet fundet. Desuden har vi kontrolleret, at den optimale kobling er single-moded og vi undersøger robustheden af dens ydeevne i forhold til strukturelle ændringer.

Preface

This Ph.D. thesis is the summary of the work conducted during my employment as Ph.D. student at the Technical University of Denmark (DTU) in the period November 15th 2011–November 14th 2014, under supervision of Professor Ole Bang and Professor Peter Uhd Jepsen, both from DTU Fotonik. The project was financed by the basic funding of DTU Fotonik. Expenses connected to travels for international conferences were partially financed by Otto Mønsted Fond.

.

Acknowledgment

This thesis is the result of my Ph.D project performed in collaboration between *Fiber Sensors and Supercontinuum* group and *Terahertz Technologies and Biophotonics group* located at Technical University of Denmark, the Department of Fotonik (DTU Fotonik).

First I would like to express my highest gratitude to my two supervisors, Professor Ole Bang and Professor Peter Uhd Jepsen, for their insightful guidance and fruitful discussions throughout the project during the past three years. I learned innumerable lessons from them in how to go about curiosity-driven research. In addition to every week's regular meeting, their office doors have always been open to discuss and help with any problem I might have had. I also would like to thank Henrik K. Rasmussen from DTU MECHANICAL for sharing interesting knowledge about polymer materials and providing Topas polymer rods for the THz fiber drawing.

I would like to thank all group members from *Fiber Sensors and Supercontinuum* group and *Terahertz Technologies and Biophotonics group*. During my initial PhD stage, I thank former PhD student Christian Agger for sharing the modeling knowledge, Dr. Krzysztof Iwaszczuk for the THz-TDS system Characterization, Dr. Alessio Stefani for THz fiber fabrication. I also thank Dr. Jonas D. Buron for sharing the knowledge on the Photoconductive antenna based THz-TDS system. I also want to thank Dr. Uffe Møller, Dr. Christos Markos, Dr. Kristian Nielsen and Dr. Jonas D. Buron, for the proof-reading of partial thesis chapters as the work looks much better now. Thank Dr. Kristian Nielsen and Dr. Christos Markos for providing valuable comments on related papers and presentations. Thank Irnis Kubat for fruitful discussions on general modeling knowledge for the whole three years.

A special thanks to Martine Nielsen and Frank Persson from mechanical workshop at DTU Electro for the precise manufacture.

I would like to thank all my friends and colleges in Denmark. I will remember those good time we spent.

Finally, I would like to express my gratitude to my parents and sister. Although they won't understand what is written in this thesis, their love and support were essential for the completion of my work in a distant country-Denmark. It is to them I would like to dedicate this thesis.

Contents

1 Introduction

1.1 Brief introduction of THz

Terahertz (THz) radiation lies between infrared radiation and microwave radiation in the electromagnetic spectrum, corresponding to frequencies range from about 0.1 THz to 30 THz or wavelength range from 3000 to 10 μm (1 THz = 10^{12}Hz = 300 μm = 1 ps = 10^{-12} s = 33.3 cm^{-1} = 4.14 meV), which is shown in Fig. 1.1.

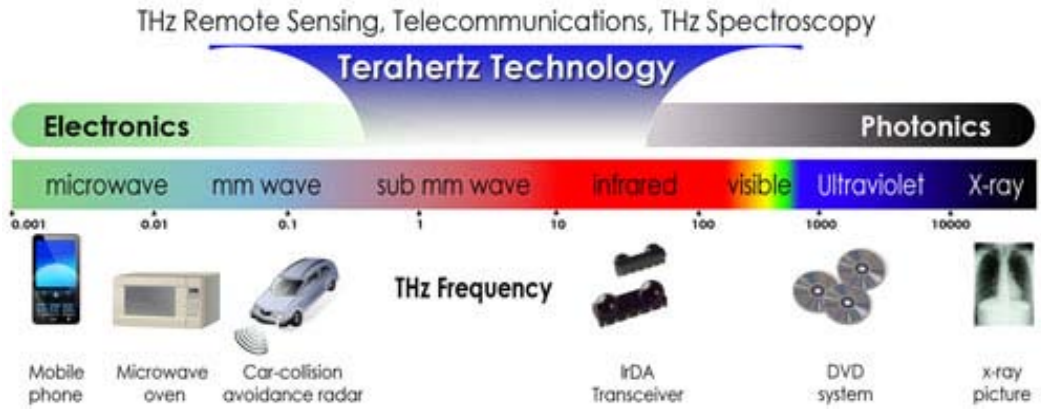

Figure 1.1 The electromagnetic spectrum, red region represent THz band in the electromagnetic spectrum.

THz radiation has several special and interesting physics properties. (a) Safe and non-ionizing due to the low photon energies (1 THz = 4.14 meV) of THz wave. This means that THz radiation is safe for potential sensing and imaging (unlike for example X-rays). (b) Relative large penetration depth for many non-conductive materials (similar with microwave radiation but exhibits a better spatial resolution). This allows us to get the information of the inner structure of samples by THz imaging. (c) Unique spectral fingerprints for many chemical and biological molecules. Moreover, spectroscopy is more flexible and sensitive in Terahertz range due to the oscillator strength of the resonant rotational or libration transitions. This allows us to identify and characterize these substances by THz-spectroscopy. (d) Both time domain and frequency domain information can be measured simultaneously, this is a distinct advantage over optical spectroscopy, which typically measure the intensity of the light field because there are no detectors that can directly measure electromagnetic fields in the optical range.

Terahertz radiation interacts strongly with systems that have characteristic lifetimes in the ps range or energy transitions in the meV range. Examples of such systems include bound electrical charges [1], free charge plasma [2], hydrogen bonds in chemicals [3], phonons in crystalline solids [4], molecular crystals [3], relaxations in liquids [5] and biological matter [6]. Time-resolved, pulsed terahertz spectroscopy is also a powerful tool to study charge carrier dynamics in semiconductors [7-10] over the past decades. Because of the its spectroscopic properties and its ability imaging in hidden objects, as well as the non-ionizing property, along with the advent of efficient THz generation and detection, there has finally been an explosion of research on THz applications. Applications include biomedicine (such as tooth, cancer detection[11, 12]), pharmaceutical industries [13, 14], in biochemistry and remote gas sensing, security and defense (body scanner or package inseption at airport security checkpoints) [15], inline monitoring of polymeric compounding process [16, 17], art conservation[18] , communication[19, 20].

As the growth in scientific applications at THz frequencies, moderate progress has been made in THz generation and detection. However, since current THz systems predominantly utilize free-space propagation, the large size and requirement of careful alignment thus increasing the complexity are the drawbacks on using such systems. Consequently, it is in urgent need to develop waveguides/devices with good guiding performance, similar with the fiber waveguides in infrared region, in THz region, which holds great promise for driving this technology further. Recently, waveguides for terahertz (THz) operational frequencies have been extensively investigated, both based on metals and dielectrics.

1.2 Metallic THz Waveguides

Metallic waveguides in THz region mostly borrow idea from well known guiding devices in microwave frequencies and radio frequencies. Examples include Hollow-core metallic waveguides, Parallel-plate metallic waveguides, and Metal-wire waveguides.

In 1999 and 2000, circular or rectangular waveguides [21, 22] in Terahertz region were investigated. The generally small air-core size result in high propagation loss [23]. Another issue is that dominant mode in Hollow-core metallic waveguides is TE and thus exist inherent

low-frequency cutoff, which will lead to strong group velocity dispersion nearby the cut-off frequency.

In fact, the transmission loss in such waveguides normally is largely dependent on the core size and they are inversely proportional to third power of core size. Hence, one approach to lower the loss is to use large core instead of the small core (Fig. 1.2(a)). Meanwhile, the cut-off frequencies of TE mode can be shifted towered lower by the enlarging the core size, thus lowering the group velocity dispersion.

Recently, the flexibility of large-core metallic tube waveguides was also studied. Borrowing the idea from infrared regime, a metallic layer was coated inside the capillary by the liquid-phase coating method [24-26] (Fig. 1.2(b)). Since skin depths of metals at THz frequencies are in 10-100nm, which means a very thin coated metal is required. As a result, this type metallic tube waveguide can be flexible, while at the same time good properties of the hollow-core pure metallic waveguides can be kept.

Another approach to improve the property of hollow-core metallic waveguides is to use dielectric-line hollow metallic waveguide (Fig. 1.2(c)), where coating a thin dielectric layer inside inner metallic surface [27-34]. The loss property is improved due to the change of the power distribution of dominant waveguide mode from TE01 mode to HE11 mode, which can be seen from Fig. 1.2 (a) and (b). Similar with a thin metallic layer coated inside the capillary. Flexibility can also be improved by depositing both metal and dielectric films inside thin wall polymer capillary (Fig. 1.2(d)) by using liquid-phase chemistry techniques.

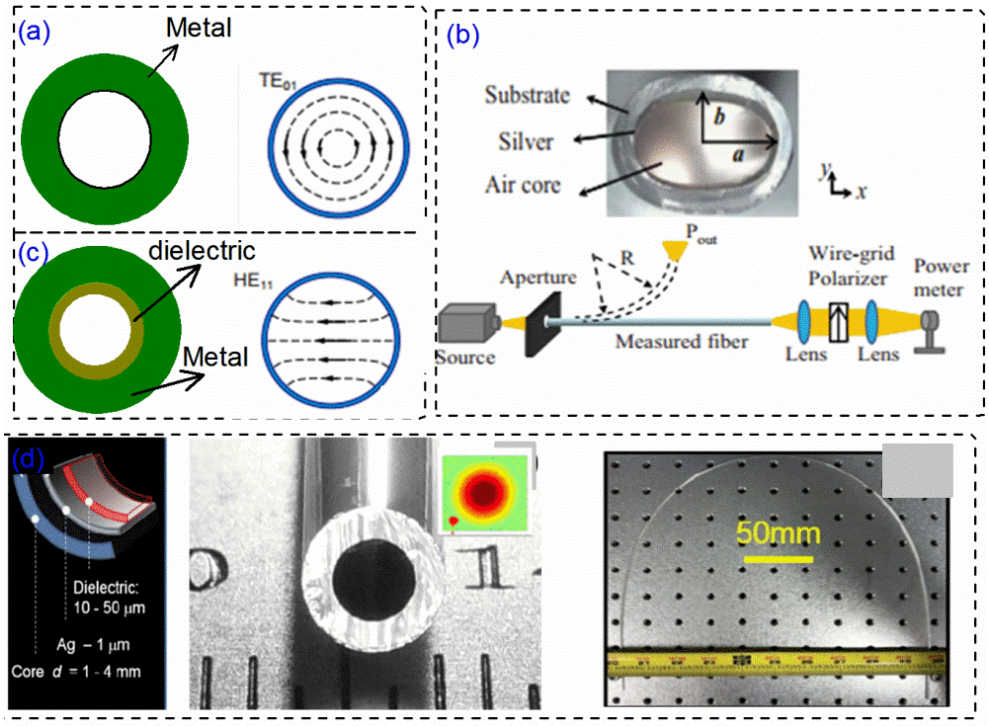

Figure 1.2 cross section of circular metallic waveguide. (b) Metal coated inside dielectric tube; adapted from [28, 32] (c) dielectric coated inside metal tube; (d) dielectric-line hollow metallic waveguide; [32]

Parallel-plate metallic waveguides (PPWG) normally consist of two slab-type metals separated by a distance [35-42]. The supported mode is mostly dependent on the excited polarization. For the input polarization perpendicular to the two plates, TEM mode can be excited. TEM mode is lowest order TM mode thus has no cut-off frequencies and posses almost negligible group-velocity dispersion (GVD) associate with the fact that the transmitted THz pulses propagating through the waveguides with almost no pulse distortion, which is very useful for time domain investigation. Meanwhile, the use of the transverse electromagnetic (TEM) mode of a parallel-plate waveguide (PPWG) can provide low loss and good coupling with the linearly polarized free-space Gaussian beam. An disadvantage is that it cannot provide complete confinement, due to the one-dimensional nature of the guide [36]. For the input beam with parallel polarization to the plates, TE mode can be excited. Similar with bared metal tube waveguides, TE mode has cut-off frequencies for the plate waveguides with small separation. This will result in strong dispersion and is not desired in some practical applications. Recent works show the feasibility to use single TE1 mode of the PPWG with much lower cut-off frequency by enlarging the plate separation and thus almost

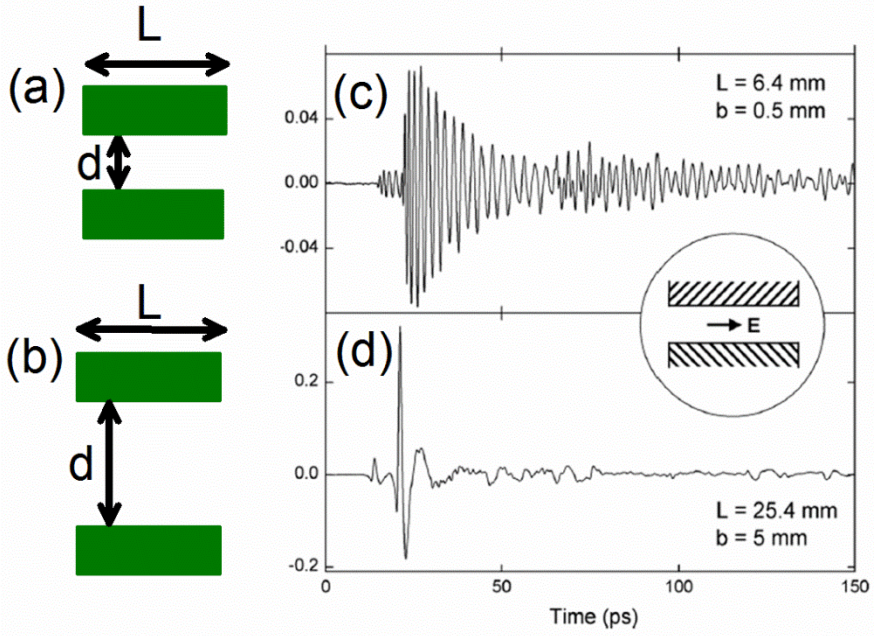

Figure 1.3 Cross section of PPWG with (a) b=0.5 mm (b) b=5 mm. (c) TE1-mode propagation in 6.4 mm long PPWG with b=0.5 mm, and (d) TE1-mode propagation in 25.4 mm long PPWG with b=5 mm. adapted from [35]

undistorted THz pulse propagation can work under this mode. Fig. 1.3 clearly demonstrates the dispersion has been significantly reduced by increasing the separation from 0.5 mm to 5 mm.

Another kind of metallic waveguides is the bare metal wire [43-49], which is just one single thin metal wire suspended in the air. The supported lowest order mode of this type waveguides is radially polarized. The guided wave called Sommerfeld wave because Sommerfeld found the first rigorous solution of Maxwell's equation for wave propagation on a single wire. It can propagate with low loss and low dispersion due to the fact that the mode has extends far into surrounded air. However, the radial polarization is very difficult to excite by using typical THz source with linear polarization, e.g., in [43], less than 1% coupling ratio has been obtained by employing a scattering mechanism from the linearly polarized terahertz radiation to the radially polarized surface wave that propagates along the metal wire and experimental setup shown in Fig. 1.4(a). Later, radially polarized emitter was proposed to increase the excitation efficiency, 50% coupling ration has been obtained by coupling from the emitter to metal-wire waveguide directly, and experimental set-up is shown in Fig. 1.4(b) [48]. But such sources are very complicated. Another method to increase

the excitation of metal-wire waveguide is to develop two-metal-wires waveguides [50-54]. In this case, the supported mode becomes linearly polarized when placing two metal wires with a constant distance, thus can be excited directly by typical THz sources with linear polarization. To make the metal-wire waveguides more practical for applications, some dielectric formed materials or microstructure dielectric [53, 55-60] (Fig. 1.4(c-g)) were introduced as an optical cladding for a classic two-wire THz waveguides. Generally good guidance properties of a two-metal-wires waveguide can also be kept. An added advantage is that it is more tolerant to bend loss because of the electromagnetic energy can be confined in a small area between the two wires.

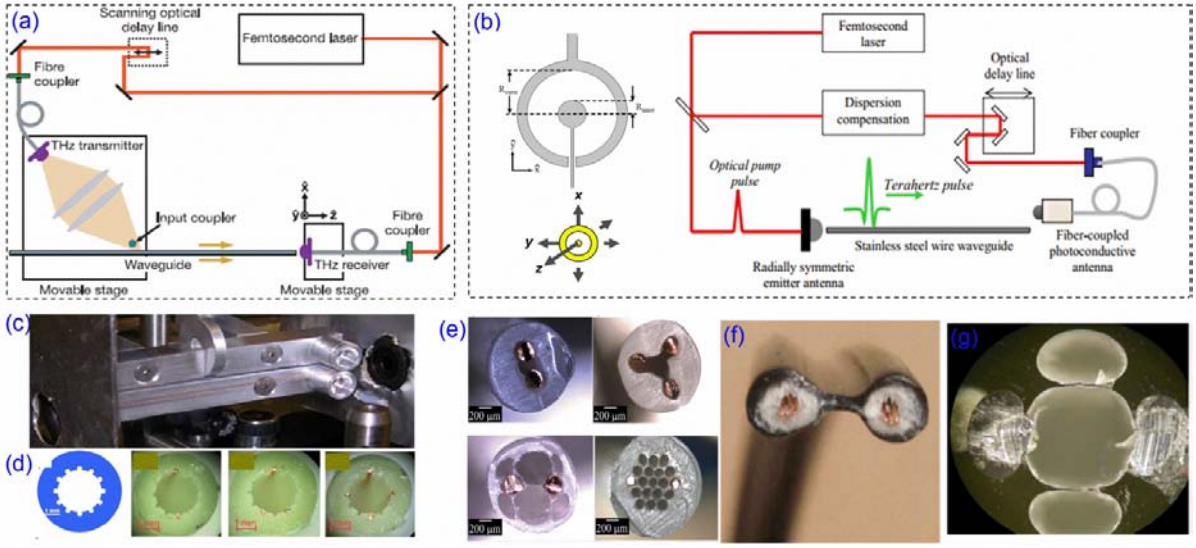

Figure 1.4 Experimental set-up for characterization of metal-wire waveguide by using (a) normal linear polarized THz source [43] and (b) radially polarized THz source; adapted from [48] (c) two-metal-wire; adapted from [60] (d-g) two-metal-wires waveguides with dielectric as holder; adapted from [54, 59, 60]

1.3 Dielectric waveguides

Apart from metallic waveguides, the dielectric material is a good choice for making terahertz waveguides. This thesis is focused on waveguides with cylindrical dimensions. The structure of the cylindrical waveguides could be solid core PCF, sub-wavelength fibers, Hollow-core waveguides.

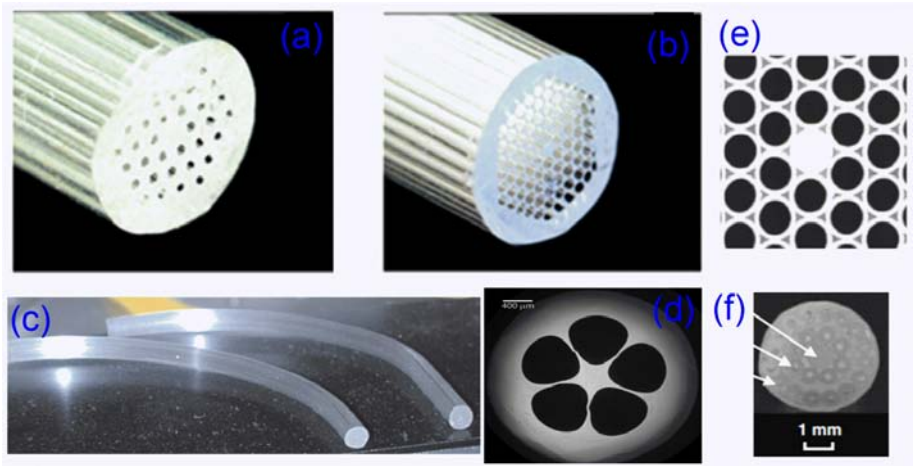

Figure 1.5 Microscope image of the transverse cross section of (a) Topas large mode area solid core PCF (b) Topas small mode area solid-core PCF fiber (c)bending Topas PCF; adapted from [61] (d) Zeneox fiber rectangular porous fiber; adapted from [62] (e) HDPE solid-core PCF fiber adapted from [63] (f) Teflon solid-core PCF fiber; adapted from [64]

One popular type dielectric THz waveguides is solid-core photonic crystal fibers (PCF). They normally consist of a solid core surrounded by an array of air holes, which modulate the cladding index. The guiding properties of the solid-core PCF can be roughly understood with an effective index model: the region with the missing hole has a higher effective index, similar to the core in a conventional fiber. Solid-core THz PCFs based on high-density polyethylene (HDPE) material was experimentally demonstrated in 2002 [63] (Fig. 1.5(e)). Since most power concentrated inside the solid core, the attenuation largely depends on the core material absorption. Following this work, host materials were replaced with lower absorption loss materials, such as Teflon [64] (Fig. 1.5 (f)), Zeonex [61] (Fig. 1.5(d)) and Topas [62] (Fig. 1.5(a-c)) were used so that the attenuation can be reduced. Besides loss information, dispersion can also be tailored by varying the cladding porosity [62]. Based on the guiding mechanism of this type PCF, several dual-core PCF THz couplers have also been proposed [65-67].

Polymer materials posses some of the lowest losses in the THz region; However, the loss is still high and cannot be neglected. It is well known that dry air is the most transparent medium in the THz region. In order to lower the propagation loss of a THz waveguide, an effective approach is therefore to maximize the fraction of the power propagating in air, while at the same time maintaining a tight confinement of the propagating mode. Several methods towards this have been proposed.

One strategy is to use a sub-wavelength core surrounded by an air cladding [68-70] (Fig. 1.6(a)). A solid sub-wavelength plate or rod [70, 71] acts as a high refractive index core and surrounding air acts as cladding. The field of the guided mode extends far into the surrounding air cladding thus significantly lowering the absorption loss. This type fibers pushed large fraction of power into the surrounded air thus have the disadvantage that they are difficult to handle, on other hand, such property is also beneficial for applying to other areas such as sensing [72] and making fiber-based couplers [73]. Besides, this type of fibers has also been successfully applied to a raster scanning imaging system [74, 75] and a near filed microscope [76]. Recently, several THz components based on sub-wavelength fiber, such as TFBGs [77-80] and THz notch filters [78, 79], were reported using laser inscription on THz sub-wavelength fiber.

In order to further reduce the loss, a porous structure of sub-wavelength holes was introduced into the already sub-wavelength solid core of the fiber [81-87] as first predicted numerically by Hassani *et al*. [81, 88] and then demonstrated by Dupuis et al. [87] and later Atakaramians *et al*. [84]. Some typical structure of porous-core subwavelength fibers are shown in Fig. 1.6(b, d, e, f). Due to the boundary conditions in the electric flux density the refractive index step between material and air in the sub-wavelength holes pushes the field into the lower index holes, thereby increasing the fraction of power in air and reducing the absorption losses [88]. Propagation losses as low as 0.04 dB/cm near 0.3THz have been reported [87].

However, irrespective of the fine details of the design, such sub-wavelength air-clad fibers are still limited in their practical applicability due to their susceptibility to perturbations. One way to shield the fiber from external perturbations is to have it be the core of a so-called suspended core fiber, which can be seen from Fig. 1.6(c), as reported by Rozé *et al*. [89], who demonstrated losses less than 0.09 dB/cm in the 0.28-0.48 THz range. This design has the added advantage that the three large holes constituting the air cladding may be purged with dry air to avoid losses due to moisture. The suspended core type THz fiber can be made to have a porous core, this has been demonstrated for relatively large cores [89]. One disadvantage of the suspended-core THz fiber is that it is rather difficult to cleave.

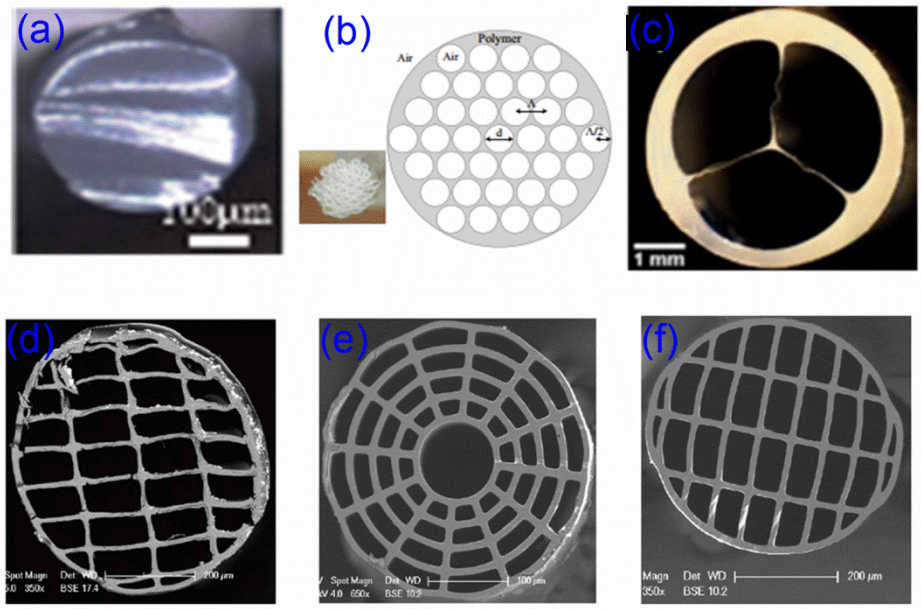

Figure 1.6 Microscope image of the transverse cross section of (a) sub-wavelength fiber; adapted from [69] (b) triangular prous-core fiber; adapted from [81] (c) Porous-core honeycomb structured fiber; adapted from [89] (d) rectangular porous fiber; adapted from [84] (e) spider-web porous fiber; adapted from [84] (f) rectangular air-hole porous fiber.; adapted from [84]

Another strategy to minimize the material losses of THz waveguides is to use hollow-core structures. This type of waveguides, which normally consist of an air-core and a structured cladding, can alleviate external disturbances as most of the field is guided within the air core region.

For PBG type THz fibers, they normally consist of a hollow core and surrounded period structure cladding, which run along the length of the fiber. The mode is confined within the air core with the help of periodic photonic crystal reflectors or multilayer dielectric materials reflectors. The former is periodic array of small air holes [90-95] (Fig. 1.7 (a))and the latter are composed of period alternating of high and low refractive index layers [96-99] (Fig. 1.7 (b-e)). Noted that Bragg fibers could also be achieved by using single material and low index layers can be obtained by air or air-holes modulation [96]. PBG fibers are particularly versatile candidates for THz wave-guiding due to the flexibility in the design of critical parameters such as center frequency, bandwidth, and dispersion. In general, the PBG type THz fibers allows low loss propagation within the cladding band-gap. However, the high air filling fraction (photonic band-gap fibers) or high contrast refractive index (Bragg fibers) as well as a strictly periodic cladding structure are needed to obtain an efficient and broad

bandgap. Porous-core honeycomb PBG fibers [100] were proposed to some extent to alleviate such problems of air core fibers, at the expense of bringing more material.

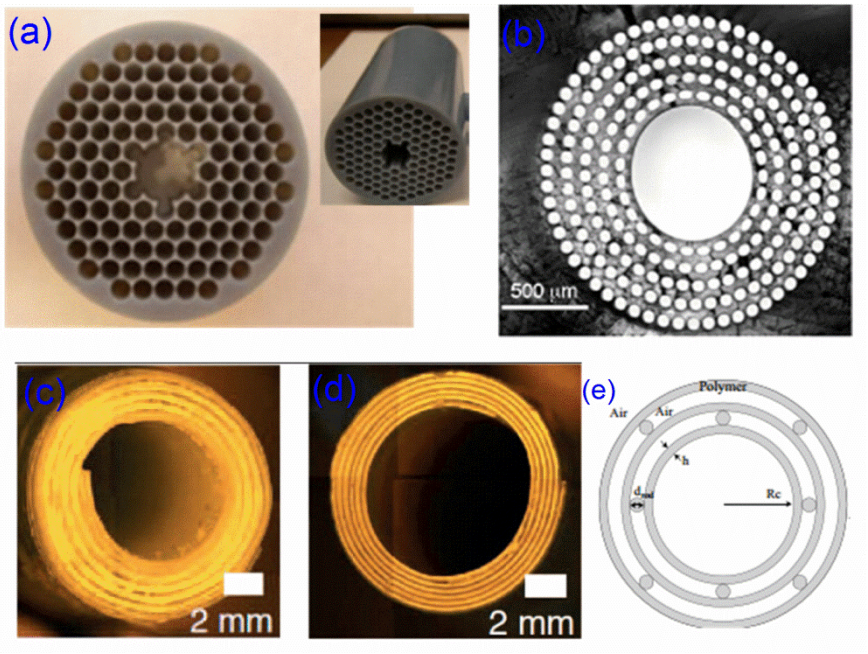

Figure 1.7 Microscope image of the transverse cross section of (a) 3D printed PMMA photonic crystal fiber; adapted from [94] (b) Ring structured Bragg fiber; adapted from [90] (c) air-polymer Bragg fiber; adapted from [101] (d) polymer-doped polymer Bragg fiber adapted from [101] (e) Cross section of air-polymer structured Bragg fiber; adapted from [81]

For Kagome-type fibers [91, 102-107], the cladding can be seen as composed of an array of hollow tubes with different shapes (Fig. 1.8 (a-c)). Unlike the PBG type fibers that guide light by means of a photonic band gap in the cladding, guiding in Kagome-type fibers is based on inhibited coupling mechanism due to the low density of cladding modes and small spatial overlap of cladding modes with core modes. Consequently, cladding structure precision and periodicity are not as strict as PBG type fibers. Leakage loss for Kagome fiber can be negligible compared with fiber material absorption loss. In fact, one ring of tubes around the core is generally enough to obtain Kagome guidance mechanism, resulting in the reduction of fiber dimension. The disadvantage of this type fiber is that this kind of guiding usually shows abrupt transmission dips within the transmission band caused by the weak but still finite coupling between core modes and cladding modes.

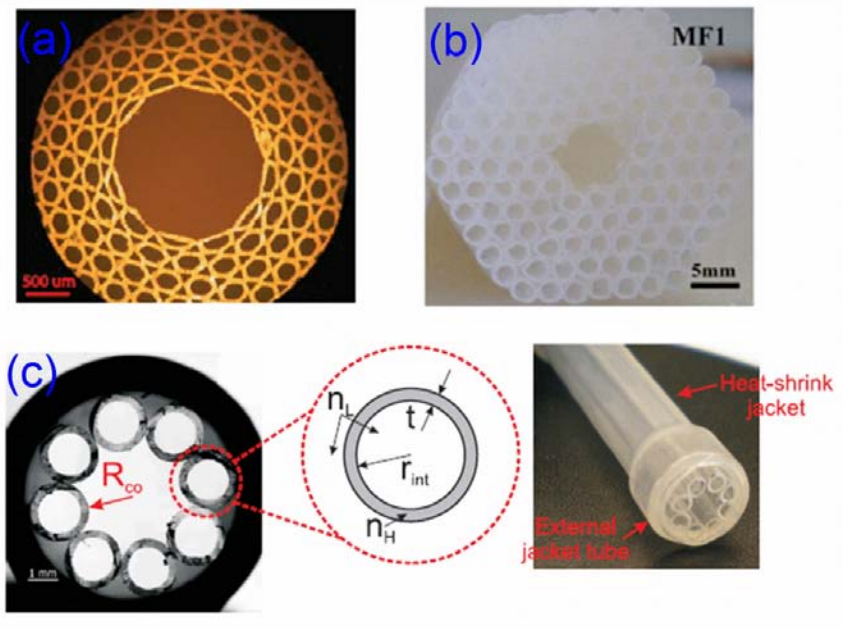

Figure 1.8 Microscope image of the transverse cross section of (a) PMMA Kagome THz fibers; adapted from [107]. (b) THz hollow-core microstructure fiber; adapted from [91] (c) Tube lattice THz fiber; adapted from [105]

In contrast to hollow-core THz fibers with complex cladding structure discussed above, THz tube waveguides are very simple and normally only consist of a large air-core and thin dielectric layer [108-112]. The guiding mechanism of the tube waveguides is that of an anti-resonant reflecting optical waveguide (ARROW) [112] with a leaky nature, which was first proposed by Miyagi and Nishida in 1980 [113] and first experimentally demonstrated in THz region by Lai et al [108, 113]. The first experimental tube waveguide structure and experiment set-up on straight THz tube are shown in Fig. 1.9 (a-b). Low loss has been successfully achieved nearby anti-resonant frequency regions. In [111], bend loss was also characterized and shown in Fig. 1.9 (c). Moreover, Tube waveguides are also extended to sensing [114] and couplers [115], In [115], a tube waveguide based directional coupler was achieved by placing two identical square pipe waveguides close to each other and using the mechanism of (ARROW) [114]. The proposed directional coupler was shown to work efficiently with low loss by choosing a proper cladding thickness of the pipe waveguides. However, the transmission bandwidth is limited by the spacing of the resonant frequencies, which is proportional to the refractive index and inversely proportional to the cladding thickness. One way to improve the transmission bandwidth is to reduce the cladding thickness [112]. One disadvantage is that a uniformly thin cladding is in practice difficult to

fabricate due to its low mechanical strength. Moreover, tube waveguides with thin walls are fragile and sensitive to external perturbation, as the propagating mode extends significantly outside the cladding.

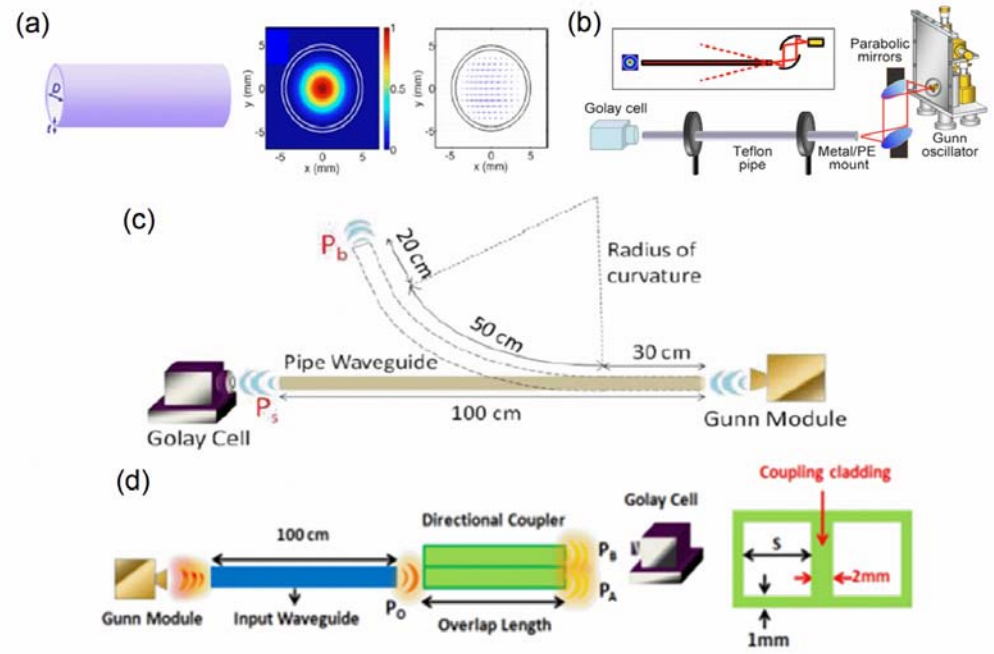

Figure 1.9 (a) Structure, intensity distribution and electric-field vector distribution of the fundamental core mode of the pipe waveguide at 420 GHz with D=9 mm and t=0.5 mm. (b) Experiment setup; adapted from [108]. (c) Bend loss adapted from [110]. (d) Experimental setup for the directional couplers; adapted from [115].

1.4 Scope of thesis

The goal of this PhD project was to design, fabricate, and characterize state-of-the-art waveguides and waveguides-based devices in THz region.

Chapter 2 introduces wave equations derived from Maxwell's equation for waveguides design. Fabry-Perot model is also described. Polymer fibers fabricated by using draw tower are also presented.

Chapter 3 describes the main principle of terahertz time-domain spectroscopy (THz-TDS) systems and characterization of the dielectric materials and basic waveguides are also presented.

Chapter 4 demonstrates both numerically and experimentally a novel band-gap THz fiber design, which consists of a honeycomb cladding structure with a porous core.

Chapter 5 presents the study of THz tube waveguides. Three strategies were proposed and investigated to suppress the ARROW mechanism. The first strategy is to deliberately introduce a high-loss, thick cladding which serves to effectively absorb the cladding field. We then show how the surrounded water jacket (which is a high absorbing materials in THz regime) reduces the interference effect between cladding and core fields and a detailed investigation on the added water effect is also presented. Finally, we demonstrate a slight angle on the outer tube wall can almost totally remove the so called ARROW mechanism. All of these strategies results in a broad transmission band with low dispersion and low propagation loss. Simulations based on both Finite Element Method (FEM) and Fabry-Perot (F-P) model in combination with experimental characterization with terahertz time-domain spectroscopy verify our findings.

Chapter 6 presents a special design of a broadband THz directional coupler, which uses mechanical down-doping of the two cores. We show how the proposed coupler provides a broad bandwidth with relative low device loss and perform detailed optimizations of the coupler design to maximize bandwidth and minimize loss.

Finally, chapter 7 gives an overall summary of this thesis and then a conclusion with an outlook.

2 Waveguide design and Polymer fibers fabrication

2.1 Maxwell Wave Equation

Maxwell's equations [116, 117] are known for more than a century and form the basis for much of the current progress in electromagnetic:

$$\begin{aligned} \nabla \times E &= -\frac{\partial B}{\partial t} \\ \nabla \times H &= J_f + \frac{\partial D}{\partial t} \\ \nabla \cdot B &= 0 \\ \nabla \cdot D &= \rho_f \end{aligned} \tag{2. 1}$$

Where ∇ is the Laplace operator, E and B are the electric filed and magnetic field, respectively. D and H are electrical displacement and magnetizing fields. ρ_f is the free charge density and J_f is the free current density. In many cases they can be written as simply as

$$D = \varepsilon_0 \mathrm{E} + \mathrm{P} = \varepsilon E \tag{2. 2}$$

$$B = \mu_0 \mu H \tag{2. 3}$$

$$J_f = \sigma E \tag{2. 4}$$

ε_0 and μ_0 are the electrical permittivity and magnetic permeability of vacuum, ε and μ is the relative electrical permittivity and magnetic permeability of material considered. σ is the introduced conductivity of the material.

In this derivation, we assume there has no free charges and current, thus $J_f = 0$ and $\rho_f = 0$. Hence Maxwell's equation are simplified to

$$\begin{aligned} \nabla \times E &= -\frac{\partial B}{\partial t} \\ \nabla \times H &= \frac{\partial D}{\partial t} \end{aligned} \tag{2. 5}$$

$$\nabla \cdot B = 0$$

$$\nabla \cdot D = 0$$

Applying curl operator ($\nabla \times$) at both side of first two equations of Eq. (2. 5) .

$$\nabla \times \nabla \times E = -\nabla \times \frac{\partial B}{\partial t} \tag{2. 6}$$

$$\nabla \cdot D = \nabla \cdot (\varepsilon E) = \varepsilon \nabla \cdot E + E.\nabla \varepsilon \tag{2. 7}$$

The left term of Eq. (2. 7) combine with the last equation of Eq. (2. 5) will result in follow relations:

$$\nabla \times \nabla \times E = \nabla(\nabla \bullet E) - \nabla^2 E = \nabla(-\frac{E \cdot (\nabla \varepsilon)}{\varepsilon}) - \nabla^2 E \tag{2. 8}$$

The right term Eq. (2. 7) combine with the second equation of Eq. (2. 5) will result in follow relations:

$$-\nabla \times \frac{\partial B}{\partial t} = -\frac{\partial(\nabla \times \mu H)}{\partial t} = \mu \frac{\partial(\nabla \times H)}{\partial t} = \mu \frac{\partial(\frac{\partial(\varepsilon E)}{\partial t})}{\partial t} = \mu\varepsilon \frac{\partial^2 E}{\partial t^2} \tag{2. 9}$$

Hence, final wave equation govering the electrical filed is derived, based on Eq. (2. 8) and Eq. (2. 9), as follows:

$$\nabla^2 E + \nabla(E \frac{\nabla \varepsilon}{\varepsilon}) = \mu\varepsilon \frac{\partial^2 E}{\partial t^2} \tag{2. 10}$$

Similarly,

$$\nabla^2 H - \frac{\nabla \varepsilon}{\varepsilon} \times \nabla \times H = \mu\varepsilon \frac{\partial^2 H}{\partial t^2} \tag{2. 11}$$

These equations combined with the appropriate boundary conditions can be used to calculate the field distribution inside the waveguides.

Scale invariance is an important property of Maxwell's equations. Suppose we know the solution for a given ε -distribution, and the scaling version can be written as $\varepsilon'(r) = \varepsilon(r') = \varepsilon'(\Lambda r)$

$$\nabla^2 'H - \frac{\nabla '\varepsilon(r')}{\varepsilon(r')} \times \nabla ' \times H(r') = \frac{w^2}{c^2} H(r') \tag{2. 12}$$

Where

$$\nabla^2 ' = \frac{\partial^2}{\partial x'} + \frac{\partial^2}{\partial y'} + \frac{\partial^2}{\partial z'} = \frac{1}{\Lambda^2}(\frac{\partial^2}{\partial x} + \frac{\partial^2}{\partial y} + \frac{\partial^2}{\partial z}) \tag{2. 13}$$

$$\nabla ' = \frac{\partial}{\partial x'} + \frac{\partial}{\partial y'} + \frac{\partial}{\partial z'} = \frac{1}{\Lambda}(\frac{\partial}{\partial x} + \frac{\partial}{\partial y} + \frac{\partial}{\partial z}) \tag{2. 14}$$

Thus the equation can be written as

$$\nabla '^2 H(\Lambda r) - \frac{\nabla '\varepsilon(\Lambda r)}{\varepsilon(\Lambda r)} \times \nabla ' \times H(\Lambda r) = \frac{w'^2}{(\Lambda c)^2} H(\Lambda r) \tag{2. 15}$$

Moreover, given solutions of Maxwell's equations when $w' = \Lambda w$.

This means if the structure scale up Λ times, the same solutions can be calculated as the frequency become times smaller.

2.2 Finite Element solver-COMSOL

The FEM solver is a commercial available software program called COMSOL, it solve the equation in frequency domain

$$\nabla \times \frac{\nabla \varepsilon}{\varepsilon} \nabla \times H = \frac{\omega^2}{c^2} \frac{\partial^2 H}{\partial t^2} \tag{2. 16}$$
$$H = H(x, y) e^{uz}$$

Where ω is the angular frequency, c is speed of light in vacuum. u is the eigenvalue and can be described as $u = -i\beta - \delta_z$. If the material has negligible absorption, the permittivity of the material can be represented by $\varepsilon = n^2$. If the absorption cannot be neglected and the

refractive index become complex value and can be written as complex value: $\tilde{n} = n - i\kappa$. In this case, the relation between refractive index, absorption and ε will be shown as following:

$$\varepsilon = (n + i\kappa)^2 = n^2 - \kappa^2 + 2n\kappa i \tag{2. 17}$$

Once the magnetic field is solved, the electric field can be found from the Maxwell equations.

To solve wave equation in an unbounded domain on a computer, one approach is to truncate the unbounded domain by using an artificial absorbing layer called 'perfectly matched layer (PML)'. The key property of a PML is that the part of the index is the same as adjoining dielectric medium while its absorption gradually increases. This property allows the PML to absorb propagation waves without reflecting back into the modeling space. Meanwhile, PML can absorb evanescent fields thus can also be used to extract the confinement loss of the mode. Under such condition, proper solution can be kept.

For waveguides with four-fold symmetry the structure can be simplified as one quarter using proper boundary conditions of the symmetry axis. Note that the selection of symmetry axis boundary conditions will result in calculated modes with different polarizations. The corresponding modes calculated based on different symmetry axis boundary conditions combinations are shown in Fig. 2.1. This method allows one to model a waveguide using only one quarter of the mesh elements of the full structure. Thus the computational resources and time can be significantly reduced.

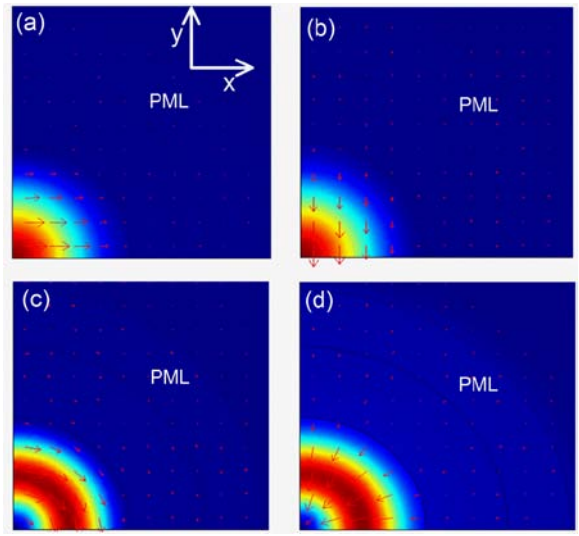

Figure 2.1 The modes calculated based on different symmetry axis boundary conditions combinations (a) x: PEC + y: PMC (b) x: PMC + y: PEC (c) x: PEC + y: PEC (d) x: PMC + y: PMC

2.3 Fabry–Pérot model

Besides The FEM solver (COMSOL), Fabry–Pérot model can also be an alternative to calculate the attenuation of tube waveguides. The derivation starts from the mode effective index. Based on the basic waveguide knowledge, the relation between propagation constant and effective index can be written as $\beta = \mathrm{neff} \cdot \sin\theta_1$, where θ_1 is the initial incident angle for the waveguide (shown in Fig. 2.2). Thus initial incident angle θ_1 can be written as

$$\theta_1 = \sin^{-1}\left(\frac{\mathrm{n_{eff}}}{n_1}\right) \tag{2. 18}$$

According to Snell's law, θ_2 and θ_3, shown in Fig. 2.2 can be express as following:

$$\theta_2 = cos^{-1}\sqrt{(1-(n_1 sin\theta_1 / n_2)^2)} \tag{2. 19}$$

$$\theta_3 = cos^{-1}\sqrt{(1-(n_1 sin\theta_1 / n_3)^2)} \tag{2. 20}$$

According to Fresnel equation, corresponding reflection and refraction coefficients of a plane wave for both TE and TM polarizations are given by

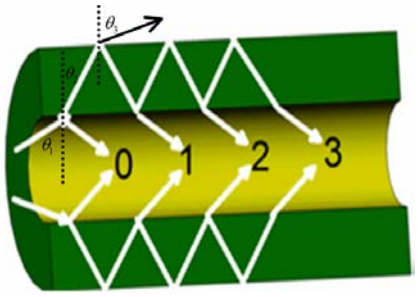

Figure 2.2 Profiles of the uniform tube waveguides. Ray-optic model are also overlapped on the cross-section of the tube waveguides.

$$r_{TE1\to2}=\frac{n_1\cos\theta_1-n_2\cos\theta_2}{n_1\cos\theta_1+n_2\cos\theta_2} \qquad r_{TE2\to3}=\frac{n_2\cos\theta_2-n_3\cos\theta_3}{n_2\cos\theta_2+n_3\cos\theta_3} \qquad r_{TE2\to1}=\frac{n_2\cos\theta_2-n_1\cos\theta_1}{n_2\cos\theta_2+n_1\cos\theta_1}$$
$$r_{TM1\to2}=\frac{n_2\cos\theta_1-n_1\cos\theta_2}{n_2\cos\theta_1+n_1\cos\theta_2} \qquad r_{TM2\to3}=\frac{n_3\cos\theta_2-n_2\cos\theta_3}{n_3\cos\theta_2+n_2\cos\theta_3} \qquad r_{TM2\to1}=\frac{n_1\cos\theta_2-n_2\cos\theta_1}{n_1\cos\theta_2+n_2\cos\theta_1} \tag{2.21}$$

$$t_{TE1\to2}=\frac{2n_1\cos\theta_1}{n_1\cos\theta_1+n_2\cos\theta_2} \qquad t_{TE2\to3}=\frac{2n_2\cos\theta_2}{n_2\cos\theta_2+n_3\cos\theta_3} \qquad t_{TE2\to1}=\frac{2n_2\cos\theta_2}{n_2\cos\theta_2+n_1\cos\theta_1}$$
$$t_{TM1\to2}=\frac{2n_1\cos\theta_1}{n_2\cos\theta_1+n_1\cos\theta_2} \qquad t_{TE2\to3}=\frac{2n_2\cos\theta_2}{n_3\cos\theta_2+n_2\cos\theta_3} \qquad t_{TE2\to1}=\frac{2n_1\cos\theta_1}{n_1\cos\theta_2+n_2\cos\theta_1} \tag{2.22}$$

The cladding layer can be seen as Fabry–Pérot etalon, thus the power reflectivity at the core-cladding interface for TE polarized light can be achieved by [118]

$$R_{TE}=\left|\frac{A_{TE}}{A}\right|^2=\left|\frac{A_0+A_1+A_2+\ldots.A_n}{A}\right|^2=\left|[r_{te12}+\frac{t_{TE1\to2}r_{TE2\to3}t_{TE2\to1}\exp(\Delta\phi)\exp(\alpha/2)}{1-r_{TE2\to3}t_{TE2\to1}\exp(\Delta\phi)\exp(\alpha/2)}]\right|^2 \tag{2. 23}$$

Where $\Delta\phi=2\pi f/c\cdot 2n_2t\cos\theta_2$ and $\alpha=-2t/\cos(\theta_2)\alpha_{PMMA}$. t is the cladding thickness, c is the speed of light in vacuum.

Similarly, the power reflectivity at the core-cladding interface for TM polarized light can be achieved by

$$R_{TM}=\left|[r_{TM12}+\frac{t_{TM1\to2}r_{TM2\to3}t_{TM2\to1}\exp(\Delta\phi)\exp(\alpha/2)}{1-r_{TM2\to3}t_{TM2\to1}\exp(\Delta\phi)\exp(\alpha/2)}]\right|^2 \tag{2. 24}$$

Here we set the waveguide length as l, R is reflectivity for each bound and N is bound number at the core-cladding interface within the propagation length l, following relation can be obtained

$$P_{z=l} = P_{z=0} e^{-\alpha l} = R^N \tag{2. 25}$$

Hence the propagation loss relative to TE and TM mode can be expressed as

$$\begin{aligned} \alpha_{te} &= -\frac{\ln R_{te}}{D \tan \theta_1} \\ \alpha_{tm} &= -\frac{\ln R_{tm}}{D \tan \theta_1} \end{aligned} \tag{2. 26}$$

The hybrid modes involve TE and TM modes and the total loss of the hybrid modes can be approximately calculated as the average of TE and TM losses [109]

$$\alpha = \frac{\alpha_{te} + \alpha_{tm}}{2} = -\left(\frac{\ln R_{te}}{D \tan \theta_1} + \frac{\ln R_{tm}}{D \tan \theta_1}\right) / 2 \tag{2. 27}$$

2.4 Polymer fibers fabrication

Fiber drawing is one of the most important parts for making the success of this work. We draw the fibers using our polymer fiber draw tower and the resulting THz fiber can be 2-8mm thick and meters long. A figure of draw tower is shown in Fig. 2.3. It mainly consists of two ovens (infrared oven and resistive oven, respectively), one preform holder and one fiber puller. Unstructured polymer preforms were obtained from different places. E.g., performs made of Topas were fabricated by Henrik K. Rasmussen at DTU Mechanics, which is a very complicated process requires precise control of pressure and temperature. A preform is simply a solid rod with roughly 6 cm in diameter and 10 cm in length. Other polymers are directly bought from industry provider.

Figure 2.3 Photograph of DTU Fotonik draw tower

The unstructured polymer preform will be passed to our workshop and the wanted hole pattern is drilled into the preform by using a computer-controlled CNC machine. One major advantage of this technique is that it allows us to get various irregular and complex shaped structured patterns. The disadvantage is time-consuming and the limited number of holes can be introduced due to the drilled size. Note that the drill with small bit size cannot be

drilled sufficiently deep due to drill bending during the process. E.g., 50mm for 1.5 mm drill bit and 100mm for 2mm.

The structured polymer preform is fixed to the holder and placed into the center of resistive oven, where the temperature is sufficiently above the polymer transition temperature so that the polymer preform can be deformed. The soften time normally take 1/2-1 hour, which mostly depend on the oven temperature and preform materials. When it softens enough and the drop is formed due to the weight gravity of bottom part (below hot zone) of preform. After that, THz fiber is drawn using the fiber puller and neck down stays in the hot zone along with the drawing process.

Under stead-state operating conditions, the final fiber diameter is determined based on simple mass conservation, the feeding speed multiply cross section of original preform is the same as the pulling speed multiply cross section of drawn fiber. The relation can be described as [119].

$$D_{preform}^2 v_{preform} = d_{fiber}^2 v_{feed} \tag{2. 28}$$

However, during the real drawing process, hot zone (the zone above transition temperature) is relative long and this will result in instable drawing due to the movement of the preform neck-down region within hot-zone. The length of the hot-zone can be reduced by introducing a preheat section or using radiative heat transfer instead of convection, leading to a more stable operation of the drawing process.

3 Terahertz time domain spectroscopy

3.1 Introduction to terahertz spectroscopy

Since the first THz time-domain spectroscopy (THz-TDS) was demonstrated in 1984 by Auston and Cheung at Bell Laboratories [120], the field has been growing rapidly and resulting in numerous practical applications. Until now, THz-TDS have been developed based on different methods [121, 122]. Here we focus on generation and detection by means of photoconductive (PC) switches. In this chapter, we briefly describe the generation and detection of THz pulses in the THz-TDS setup, and describe some basic methods for extraction of frequency-dependent parameters of dielectric material and waveguide samples from the measured signals.

3.2 Terahertz pulse generation and detection by photoconductive switch

3.2.1 Terahertz generation

Generating coherent THz radiation using photoconductive antenna is a very popular way. This technique was invented by D. H. Auston [123] and further developed later in [124-129].

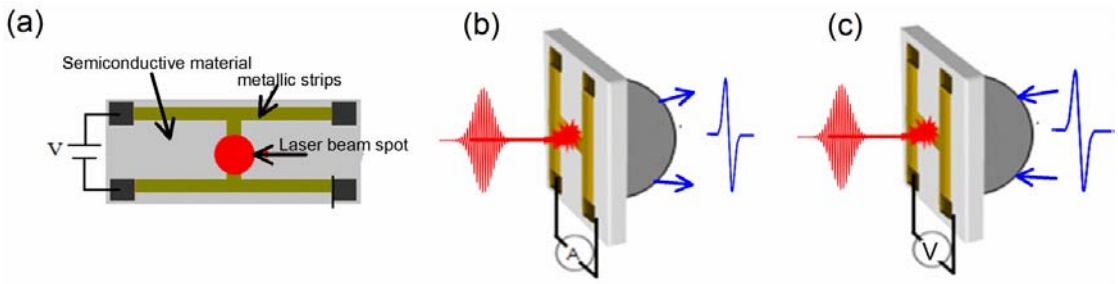

Figure 3.1 Schematic of photoconductive switch. (a) Front view of the photoconductive switch. Side view of the photoconductive switch used for (b) emitter and (c) detector, respectively.

A typical photoconductive antenna consists of two metallic stripes with a small gap in between and a semiconductor material. The geometry of the typical photoconductive antenna is shown in Fig. 3.1.

Substrate materials for ultrafast photoconductive switching require properties such as short free carrier lifetime, high carrier mobility and high breakdown field. Radiation-damaged silicon on sapphire (RD-SOS), GaAs or low-temperature grown GaAs are most common materials for this purpose. A DC voltage bias is applied to the metallic stripes and ultra-short duration laser (typically $<1ps$) with above band-gap E_g energy is impinged on the small gap. Free charge carriers are created by interband photon absorption and accelerated by the applied DC bias, by which mechanism a transient current flowing along the direction of the applied electrical filed is generated. Since the mobility of electrons is often significantly higher than that of holes, the major contribution to the photo-current comes from the electrons. The current density J(t) can be expressed as

$$J(t) = N(t)e\mu E_b \tag{3.1}$$

Where $N(t)$ is the density of photo-carriers, e is the electron charge, μ is the mobility of the carriers and E_b is the applied bias field.

The emitted THz field E_{THz} is proportional to the time derivation of this current and combine Eq. (3.1) can be written as

$$E_{THz} = \frac{1}{4\pi\varepsilon_0}\frac{A}{c^2 z}\frac{\partial J(t)}{\partial(t)} = \frac{Ae}{4\pi\varepsilon_0 c^2 z}\frac{\partial N(t)}{\partial t}\mu E_b \tag{3.2}$$

Where A is the area of illumination, ε_0 is the permittivity in vacuum, c is the speed of light, E_b is the bias field. Eq. (3.2) indicates that the THz field is linearly proportional with applied bias field and laser pulse energy. In fact, this linear relationship is only approximately true under weak excitation and low bias field. When the substrate of the PC antenna is excited, it is no longer a semi-insulating material, but rather a conductive medium. Therefore, the biased field is suppressed by the induced field, and the relation of the final THz filed and pulse energy is modified from Eq. (3.2) to Eq. (3.3)

$$E_{THz} \propto \frac{I_0}{(1+kI_0)^2} \tag{3.3}$$

Where k is the ratio between intensity-functioned conductivity of the substrate and excitation laser intensity. Eq. (3.3) clearly shows that the THz field becomes saturating when the excitation laser is strong enough.

Note that there exists a maximum for the applied bias field to prevent the material from breaking down. This maximum value is related to several factors, such as the gap size, laser fluence, and carrier density.

Alternatively, the generated electromagnetic radiation caused by transient current can also be explained via Maxwell's equations [130]

$$\nabla \times E_{THz}(t) = -\mu \frac{\partial H_{THz}(t)}{\partial t} \tag{3. 4}$$

$$\nabla \times H_{THz}(t) = J(t) - \frac{\partial \varepsilon(t) H_{THz}(t)}{\partial t} \tag{3. 5}$$

Where E_{THz} is radiated electrical field and H_{THz} is radiated magnetic field, ε and μ are permittivity and permeability, respectively. The generated THz radiation is an almost single-cycle pulse in the time domain, thus leading to a broadband spectrum [131, 132].

3.2.2 Terahertz detection

Photoconductive detection of THz pulse shares similar mechanism as photoconductive emission. The only major difference is that as a detector, instead of applying a bias voltage to metallic stripes for the emitter, two metallic strips are connected by a current sensor. Typically a lock-in-amplifier is used to amplify the signal so that even small signals can be detected accurately. Similarly to the case of a photoconductive emitter, a laser pulse impinges the gap and generates photo-carriers. The THz field to be detected induces a charge movement and thus photo-current is generated. A time delay is introduced between

the pump and probe laser pulse and the recorded photocurrent J(t) will be a time convolution between $E_{THz}(t)$ and the response function of the detector $\sigma(t)$ [121]

$$J(\tau) = \int_{-\infty}^{t} \sigma(t-\tau) E_{THz}(\tau) d\tau \tag{3. 6}$$

If the carrier lifetime and the laser pulse duration are very short, the detector will response like a delta function and the detected photocurrent will be proportional to the time dependent electrical field $E_{THz}(t)$.

3.2.3 Silicon lens

Since the photoconductive switch is a point source terahertz radiation will be emitted in a wide range of angles. Therefore, it is necessary to use lens to collect and collimate the highly divergent THz radiation. One popular material for the lens is high resistivity silicon, which has similar index as substrate conductive materials so that can significantly reduce the interfacial reflection losses. The hyperhemispherical lens [133] is commonly used for efficiently collecting the THz field, which are shown in Fig. 3.2.

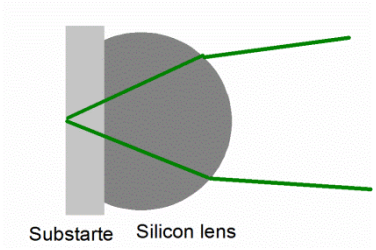

Figure 3.2 A hyper-hemisphercal lens placed on a substrate with matched refractive index along with the ray tracing.

3.2.4 Photoconductive antenna based THz-TDS system at DTU Fotonik

Figures 3.3 (a) (b) show a commercial fiber-coupled THz-TDS. It provides an effective spectral range 0.1-2.0 THz under the average of 10.000 to 100.000 individual scans. Waveforms with a time window of 320 ps are recorded every 10 ms, thus an average of 10.000 require 100 seconds of measurement time. Subsequent Fourier analysis of the spectral content of the transmitted signals is then used to get the frequency-dependent signals. System signal of time domain and frequency domain are shown in Fig. 3.4 (a) and (b), respectively.

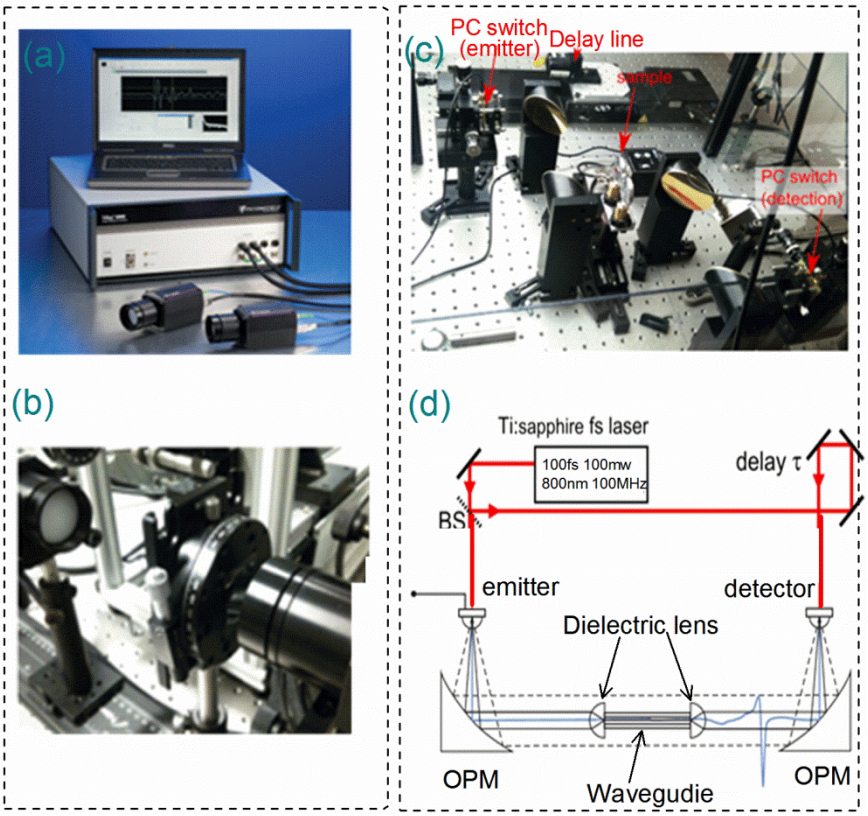

Figure 3.3 Photograph and schematic illustration of THz-TDS systems using photoconductive antennae. (Left) Picometrix 4000 commercial fiber-coupled terahertz time-domain spectrometer (Right) custom made THz-TDS system.

DTU Fotonik also has a custom made THz-TDS system. Photograph and schematic illustration of THz-TDS systems using photoconductive antennas are shown in Fig. 3.3 (c) and (d), respectively. A pulse train consisting of femtosecond optical laser pulses with short pulse duration of around 100 fs and a wavelength of 800 nm is split into two parts by a beam splitter. One of two parts is referred as the pump beam and the other one is referred as the probe beam. The pump beam illuminates the emitter to generate the THz pulses and the probe beam is used to detect the THz pulse through the inverse process for the THz generation. A delay line is used to make the optical pulse at the detector arrive at the same time as the THz pulse and gate the detector. The THz field can be recorded as a function of time by varying the delay line.

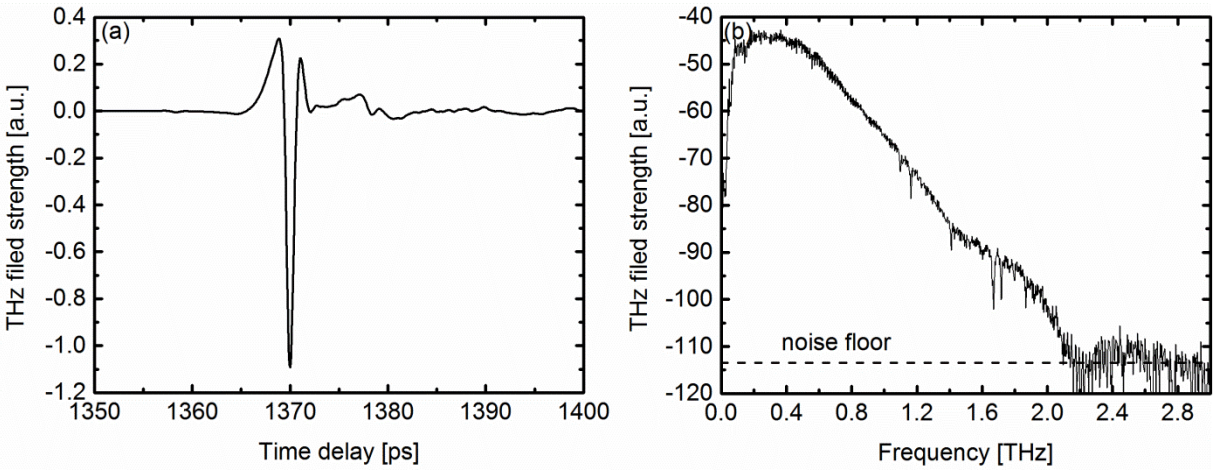

Figure 3.4 Recorded (a) time domain and (b) frequency domain signal from Picometrix 4000. 6 inch dielectric lens were used during the measurement and 10000 waveforms averaged.

3.3 Refractive index and absorption measurement in THz range

In the THz time-domain spectroscopy, THz pulses are measured with and without a sample. Since THz-TDS rely directly on measurement of the electric field, not only the absorption but also the refractive index of the sample can be obtained by analyzing the Fourier transforms of the waveform. In other words, the real and imaginary parts of the dielectric constant of a material can be measured directly without indirect methods such as the use of the Kramers-Kronig relation [134].

3.3.1 Case of low absorbing sample

For the low absorbing samples, thick samples are allowed for the measurement. In this case, echoes caused by multiple reflections inside the sample are well separated. Hence, it becomes possible for only considering the terahertz pulse transmitted directly through the sample, while neglecting the multiple reflections inside the sample, as shown in Fig. 2.4.

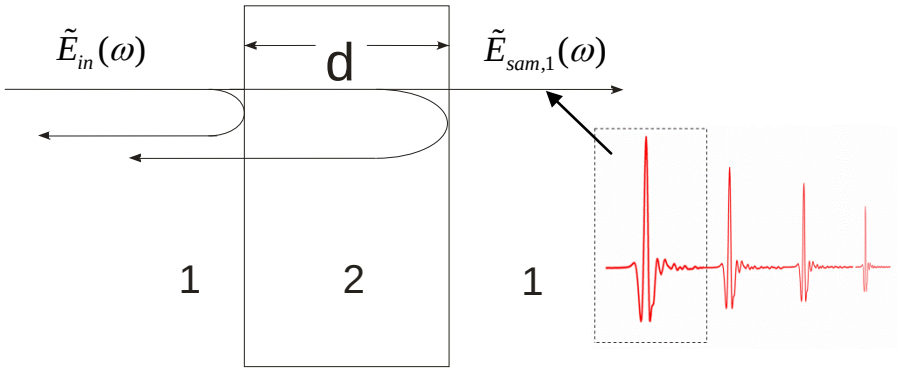

Figure 2.4: Schematic illustration of the geometries for transmission and reflection spectroscopy. $\tilde{E}_{in}(\omega)$ is the incident field, $\tilde{E}_{sam,1}(\omega)$ is the transmitted field.

For the transmission experiment, the THz system response of a sample can be determined by the ratio between the sample frequency response $\tilde{E}_{sam,1}(\omega)$ and the reference frequency response $\tilde{E}_{ref}(\omega)$. The system response can be shown with the following equation:

$$\tilde{E}_{ref}(\omega) = \tilde{E}_{in}(\omega) p_{air}(\omega, l) \tag{3. 7}$$

$$\tilde{E}_{sam,1}(\omega) = \tilde{E}_{in}(\omega) p_{air}(\omega, l-d) \tilde{t}_{12} p_{sample}(\omega, d) \tilde{t}_{21} \tag{3. 8}$$

$$\frac{\tilde{E}_{sam}(\omega)}{\tilde{E}_{ref}(\omega)} = T(\omega) e^{i\phi(\omega)} = \tilde{t}_{12}\tilde{t}_{21} e^{-\alpha d/2} e^{i(n-1)wd/c} \tag{3. 9}$$

Where $p_{air}(\omega, l) = e^{i\frac{\omega}{c} n_{air} l}$ and $p_{sample}(\omega, d) = e^{i\frac{\omega}{c} n_{sam} d}$. For materials with negligible absorption, the Fresnel transmission coefficients are real-valued. Thus the formula of the extracted index and absorption can be given by [135]

$$n(\omega) = 1 + \frac{\phi(\omega) c}{\omega d} \tag{3. 10}$$

$$\alpha(\omega) = -\frac{2}{d} \ln\left(\frac{(n+1)^2}{4n} T(\omega)\right) \tag{3. 11}$$

During the material parameter extraction, phase unwrapping is applied to ensure the extracted phase is continuous and has no 2π jumps. Another issue is that since the phase is

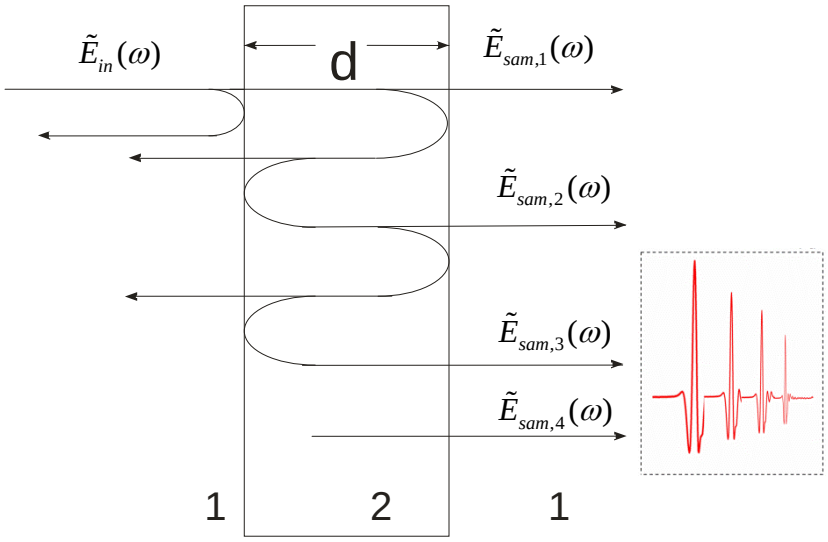

Figure 2.5: shows the ray propagation through the investigated sample in seven different stages and is governed by the following relation

linear function versus frequency and the phase should be zero at zero frequency. For its compensation, we firstly make a line fit curve to the phase data and then make an integrated times 2π offset to ensure the phase at zero frequency as close as possible to zero.

3.3.2 Case of highly absorbing sample

For a highly absorbing sample, we have to prepare a thin sample for characterization in order to get enough power with broadband frequencies for analyzing. In this case, terahertz pulse echoes are superimposed that prevents us from breaking up the terahertz signal transmitted through the sample into successive echoes. The only way to extract the sample parameters is based on the entire time domain signal. In other words, we have to consider the multiple reflections inside the sample for the extraction. To solve this problem, we need a special method for real-time analysis of the THz waveform. The transmission THz fields are related to transmission, reflection and propagation coefficients for each of the temporally separated echoes, caused by multiple internal reflections in the sample, as shown in Fig. 2.5.

$$\tilde{E}_{sam,1}(\omega) = \tilde{E}_{in}(\omega)\, p_{air}(\omega, l-d)\tilde{t}_{1\to 2}\, p_{sample}(\omega, d)\tilde{t}_{2\to 1} \tag{3. 12}$$

$$\tilde{E}_{sam,2}(\omega) = \tilde{E}_{in}(\omega)\, p_{air}(\omega, l-d)\tilde{t}_{1\to 2}\, p_{sample}(\omega, d)\left[\tilde{r}_{2\to 1}\tilde{r}_{2\to 1}\, p_{sample}(\omega, d)\right]\tilde{t}_{2\to 1} \tag{3. 13}$$

$$\tilde{E}_{sam,3}(\omega) = \tilde{E}_{in}(\omega)\, p_{air}(\omega, l-d)\tilde{t}_{1\to 2}\, p_{sample}(\omega, d)\left[\tilde{r}_{2\to 1}\tilde{r}_{2\to 1}\, p_{sample}(\omega, d)\tilde{r}_{2\to 1}\tilde{r}_{2\to 1}\, p_{sample}(\omega, d)\right]\tilde{t}_{2\to 1} \tag{3. 14}$$

$$\tilde{E}_{sam,n}(\omega) = \tilde{E}_{in}(\omega)\, p_{air}(\omega, l-d)\tilde{t}_{1\to 2}\, p_{sample}(\omega, d)\left[\tilde{r}_{2\to 1}\tilde{r}_{2\to 1}\, p_{sample}(\omega, d)\right]^{n-1}\tilde{t}_{2\to 1} \tag{3. 15}$$

$$\begin{aligned}\tilde{E}_{total}(\omega) &= \tilde{E}_{sam,1}(\omega) + \tilde{E}_{sam,2}(\omega) + \tilde{E}_{sam,3}(\omega) + \ldots \\ &= E_{in}(\omega)\, p_{air}(\omega, l-d)\tilde{t}_{1\to 2}\, p_{sample}(\omega, d)\tilde{t}_{2\to 1}\left[1 + \sum_{2}^{n-1}(\tilde{r}_{2\to 1}\tilde{r}_{2\to 1}\, p_{sample}(\omega, d))^{n-1}\right]\end{aligned} \tag{3. 16}$$

Where $p_{air}(\omega, l) = e^{i\frac{\omega}{c}\tilde{n}_{air}l}$ and $p_{sample}(\omega, d) = e^{i\frac{\omega}{c}\tilde{n}_{sam}d}$. $\tilde{r}_{12}, \tilde{r}_{21}, \tilde{t}_{12}, \tilde{t}_{21}$ represent the reflection and transmission from air to sample and sample to air, respectively.

$$\tilde{r}_{1\to 2} = \frac{\tilde{n}_2 - \tilde{n}_1}{\tilde{n}_1 + \tilde{n}_2} \tag{3. 17}$$

$$\tilde{r}_{2\to 1} = \frac{\tilde{n}_1 - \tilde{n}_2}{\tilde{n}_1 + \tilde{n}_2} \tag{3. 18}$$

$$\tilde{t}_{1\to 2} = \frac{2\tilde{n}_1}{\tilde{n}_1 + \tilde{n}_2} \tag{3. 19}$$

$$\tilde{t}_{2\to 1} = \frac{2\tilde{n}_2}{\tilde{n}_1 + \tilde{n}_2} \tag{3. 20}$$

$$H(\omega) = \frac{\tilde{E}_{sample}(\omega)}{\tilde{E}_{ref}(\omega)} \tag{3. 21}$$

Where $\tilde{n}_1$ and $\tilde{n}_2$ is complex index of refraction of related material. And the theoretical transfer function can be expressed by

$$H_{theory} = \frac{\tilde{E}_{sam,1}(\omega)}{\tilde{E}_{ref}} = p_{air}(\omega,-d)\tilde{t}_{12}p_{sample}(\omega,d)\tilde{t}_{21}\left[1+\sum_{2}^{n-1}(\tilde{r}_{21}\tilde{r}_{21}p_{sample}(\omega,d))^{n-1}\right] \quad (3.22)$$

Then we define the error by taking the absolute difference between the magnitude and the unwrapped phase of the measured data versus the model

$$D = \left\| H(\omega)| - |\tilde{H}(\omega) \right\| + \left| \angle |H(\omega)| - \angle |\tilde{H}(\omega) \right| \quad (3.23)$$

Guessed thickness should be provided firstly and then get the optimum complex refractive index for each frequency based on the minimum total error D in Eq. 3.23. Therefore, the complex refractive index versus frequency curve can be obtained. We extract the curves for a range of values of the sample thickness d and accurate thickness is determined from the smoothest material parameter curve. Extracted refractive index and absorption of PMMA with 1mm (black) and 5mm (red) thick are shown in Fig. 2.6. Results extracted from 5mm PMMA based on the terahertz pulse transmitted directly through the sample (without considering multiple reflection). The extracted data is in good correnspondance with each other indicating the method in this section is accurate. Note that the extracted parameters of the 5mm sample are only shown below 0.8 THzbecause of the high absorption of the 5mm sample at high frequencies.

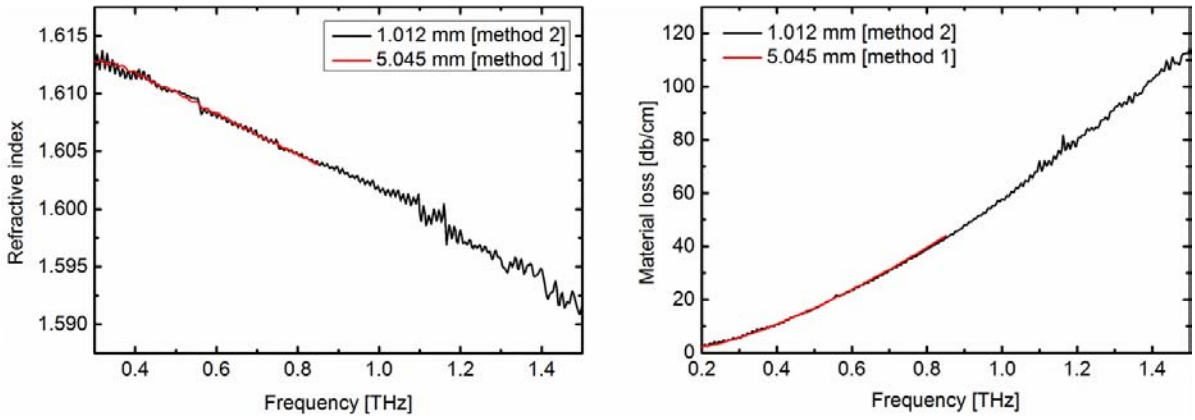

Figure 2.6: Refractive index and material loss of the PMMA sample with thickness of 1 mm and 5 mm. Red curve: 5 mm thick sample is extracted based on the terahertz pulse transmitted directly through the sample; Black curve: 1mm thick sample is extracted with the consideration of the Fabry–Pérotreflection.

3.3.3 THz-TDS characterization of Waveguides

The propagation loss of waveguides can be obtained by using cut-back method. The reference signal is measured without a waveguide in the setup and with two lenses placed so that the waist overlap and entire system is confocal, and it can be expresses as

$$\tilde{E}_{ref}(\omega) = \tilde{E}_{in}(\omega) e^{i\frac{\tilde{n}_{air}\omega}{c}l} \tag{3.24}$$

After the insertion of the waveguides, transmission signal for the waveguides with length L_1 and L_2 can be described as

$$\begin{aligned} \tilde{E}_{waveguide,l1}(\omega) &= \tilde{E}_{in}(\omega) C_{in} C_{out} e^{i\frac{\tilde{n}_{air}\omega}{c}\frac{L_{air}}{2}} e^{i\frac{\tilde{n}_{waveguide}\omega}{c}\frac{L_1}{2}} \\ &= \tilde{E}_{in}(\omega) C_{in} C_{out} e^{i\frac{\omega}{c}[\tilde{n}_{air}\frac{L_{air}}{2} + i\tilde{n}_{waveguide}L_1]} e^{i\frac{\alpha L_1}{2}} \end{aligned} \tag{3.25}$$

$$\begin{aligned} \tilde{E}_{waveguide,L_2}(\omega) &= \tilde{E}_{in}(\omega) C_{in} C_{out} e^{i\frac{\tilde{n}_{air}\omega}{c}\frac{L_{air}}{2}} e^{i\frac{\tilde{n}_{waveguide}\omega}{c}\frac{L_2}{2}} \\ &= \tilde{E}_{in}(\omega) C_{in} C_{out} e^{i\frac{\omega}{c}[\tilde{n}_{air}\frac{L_{air}}{2} + i\tilde{n}_{waveguide}L_2]} e^{i\frac{\alpha L_2}{2}} \end{aligned} \tag{3.26}$$

Finally the power attenuation coefficient and dispersion data can be calculated by comparing the transmission of waveguide with different lengths.

$$T(\omega) e^{i\phi(\omega)} = \frac{\tilde{E}_{waveguide,L_2}(\omega)}{\tilde{E}_{waveguide,L_1}(\omega)} = e^{-\alpha(L_2 - L_1)/2} e^{i(n-1)\frac{\omega}{c}(L_2 - L_1)} \tag{3.27}$$

Where $\tilde{E}_{ref}(\omega)$ is measured reference signal, $\tilde{E}_{in}$ and is the field C_{in} and C_{out} are the input and output coefficients with respect to waveguide.

Correspondingly, coupling loss can also be extracted by combining Eq. (3.24) Eq. (3.25) and Eq. (3.26).

4 Porous-core Honeycomb band-gap THz fibers

4.1 Introduction

Photonic bandgap gap (PBG) fibers are particularly versatile candidates for THz waveguiding due to the flexibility in the design of critical parameters such as center frequency, bandwidth, and dispersion. In the meanwhile, they are interesting due to the fact that the THz field is guided within the air-core region, and consequently propagation loss and environmental disturbance can be significantly reduced.

Several different designs related to PBG cladding structures in THz region have been realized, such as a hexagonal cladding hole structure [91, 94] or an omnidirectional Bragg-stack type cladding with rings of hole structures [90] or continuous layers of alternating materials [90, 96, 97].

Looking at the state-of-the-art in fabricated THz PBG fibers [90, 91, 94, 96, 97], no fiber has yet been reported, which has good broadband transmission around 1 THz, may be bent and cleaved, and which can be (mass) fabricated in long length. The stacking+tubing [94] and polymer jetting [94] techniques provide good periodic (hexagonal) hollow-core PBG structures, but at the expense of very thick fibers that do not display broadband low loss guiding and do not easily allow bending, cleaving and fabrication of long lengths. The rolling+solidification technique [96, 97] can make low loss PBG Bragg fibers, but the fibers are very big and extremely fragile. The only technique that allows mass fabrication of long lengths of THz fiber is conventional fiber drawing [90] (see also [61, 81] for solid-core THz fibers). However, good-quality hollow-core PBG THz fibers have so far been difficult to draw due to the different expansion rates of holes of different diameter at elevated temperatures, which leads to deformation of the smaller holes during the drawing process, unless special precautions are taken. The imbalance of hole dimensions can to some extent be alleviated by applying pressure to the holes during drawing. However, such a procedure can only be applied to a limited extent and obviously adds to the complexity of fabrication.

In this chapter, a novel porous-core honeycomb bandgap THz fiber is investigated to overcome the fabrication problems caused by the imbalance of hole dimensions. This type fiber consists of a hollow-core PBG THz fiber cladding structure with a porous core (the same

air-hole size as the cladding holes) inserted into the hollow core. This allows PBG guidance, while still keeping the loss low due to the porous core. Due to the increased effective index of the core, the cladding PBG structure is a honeycomb structure, which from optical fibers is known to more easily allow broad bandgaps [107, 136, 137]. The fabrication and experimental characterization of such a PBG THz fiber are also performed. The fiber is made of polymer TOPAS and confirm that it allows to fabricate long lengths of fiber with a near-perfect periodic structure and thus very clear bandgap guidance. The fundamental bandgap at 0.75-1.05 THz is found to have losses lower than 1.5 dB/cm, whereas the loss is below 1.0 dB/cm in the reduced bandgap 0.78-1.02 THz. The particular fiber we present has an outer diameter of 3.65 mm, and is thus already flexible. The outer diameter can be further reduced and thus these fibers may also be bent and cleaved.

4.2 Fiber structure

Fig. 4.1(a) shows the idealized structure of the proposed porous-core honeycomb bandgap terahertz fiber for simulation and Fig. 4.2(b) shows a microscope image of the end facet of the fabricated fiber. The fiber consists of a honeycomb lattice of air holes with hole diameter d, and lattice pitch Λ, D_c is the effective core diameter, and D is the outer diameter of the whole fiber.

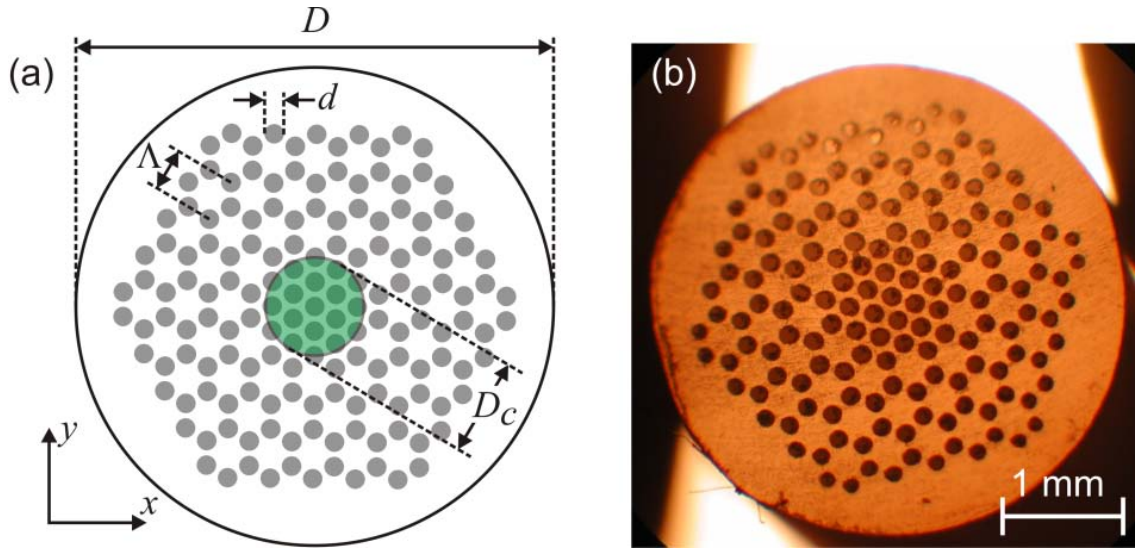

Figure 4.1 Idealized structure used in the simulation. (b) Microscope image of the actual fiber. Dark regions represent air and green central region in (a) represents the low index porous core region. d = 165 µm, Λ = 360 µm, D_c = 0.8 mm.

The low-index porous core (indicated by green circle in Fig. 4.1(a)) is formed by introducing a hexagonal array of air holes with the same diameter as the holes in the cladding. We fabricated the proposed fiber by using a cyclic olefin copolymer (COC) with the trade name TOPAS® COC 8007, obtained from Topas Advanced Polymers, Inc. The polymer granulates - were cased into cylinders and then used as preforms. The desired photonic crystal hole structure was drilled into the polymer preform, and this structure was then preserved throughout the drawing process.

The bulk dielectric properties (absorption coefficient and refractive index) of TOPAS® were characterized by THz time-domain spectroscopy (THz-TDS) on a disk with a thickness of 0.9992 cm and a diameter of 6 cm. The absorption coefficient and index of refraction are shown in Fig. 4.2.

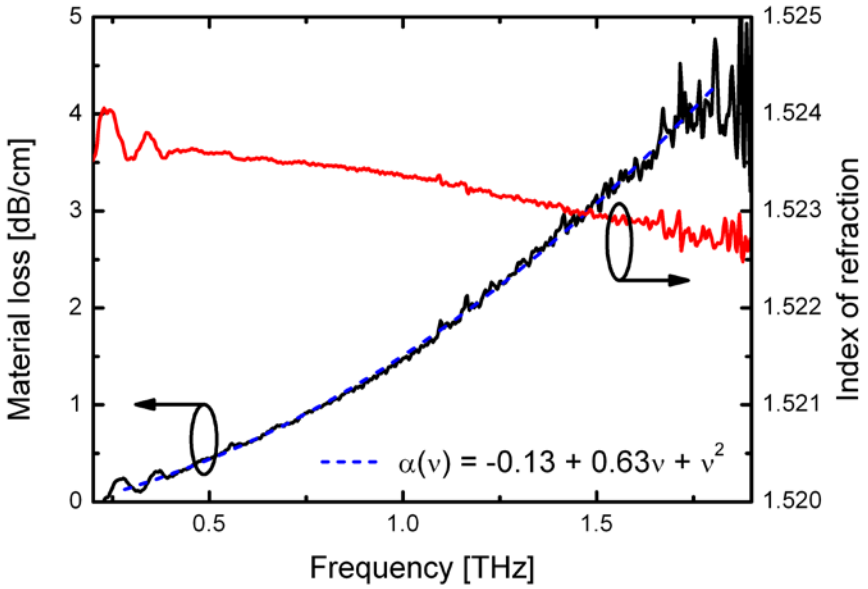

Figure 4.2 Refractive index (red curve) and material loss (black curve) of the TOPAS® polymer used for fiber fabrication, measured on a disk with a thickness of 0.9992 cm and a diameter of 6.0 cm. Blue dashed curve is a phenomenological quadratic fit to the loss used in Figure 4.3.

The material has an almost constant refractive index in the 0.2-2 THz range (near 1.5235, in excellent agreement with previously reported values [62]) and low loss (<1 dB/cm up to 0.8 THz, and <4 dB/cm up to 2 THz). In addition to the detailed methods you need to describe in this section, you need to provide specific objectives and an overview of your approach if they have not already been presented.

The honeycomb-cladding, limited to three rings by the diameter of the preform, and the porous core structure was drilled into the preform and then drawn to the final diameter. The structure is preserved during the drawing process and Fig.4.1b) shows a cross-sectional image of the fabricated THz fiber. The following parameters describe the fabricated THz fiber: D = 3.65 mm, d = 165 μm, Λ = 360 μm, and D_c = 0.8 mm. These are average values, with very small fluctuations across the fiber, as evident from Fig. 4.1(b).

4.3 Simulation and experimental results

Simulation of the fabricated fiber were carried out by using commercial software based on the plane-wave method (BandSolve, RSoft Design) for the band gap of the cladding unit cell and the commercially available FEM solver (COMSOL3.5a) for the fundamental core mode (green lines) and cladding modes (black dots) of the fiber. The resulting two band gaps are shown in gray in Fig. 4.3. The full geometry of the fiber was considered, including the finite outer diameter D. A 1 mm thick layer of air was placed around the fiber, again surrounded by a perfectly matched layer (PML) to be able to calculate the confinement loss. The resulting frequency-dependent effective refractive index of the fundamental mode in the two band gaps is shown in Fig. 4.3 (black curve), and the frequency-dependent fraction of the total power of the fundamental mode that is localized within the core region is shown in Fig. 4.4 (red curve). The small insets below Fig. 4.3 show the S_z energy flux distribution of the fundamental mode of the fiber at four different frequencies (0.7, 0.9, 1.4 and 1.6 THz). Numerous sharp resonant features are visible in the core power ratio, indicative (as will be discussed below) of resonant coupling between the reflected field from the outer interface of the fiber and the core mode. To illustrate this coupling, the two insets in Fig. 4.4 show the S_z energy flux distribution of the fundamental modes at two nearby frequencies at 0.80 THz (with low core power ratio) and at 0.82 THz (high core power ratio). Comparison of these two insets shows that at specific resonant frequencies, a large fraction of the power is located near the outer perimeter of the fiber, while the mode profile away from these resonances is confined to the core region.

To shed further light on the effect of a finite fiber diameter and the effect of the reflection at the fiber/air interface we performed simulations where we eliminated the reflective polymer/air interface by applying a PML directly to the outer surface of the TOPAS fiber, thereby effectively modeling an infinitely large fiber. The calculated frequency dependent core power ratio of the fundamental mode is shown in Fig. 4.4 (blue curve). The band gaps are identical to the finite fiber simulation discussed previously (red curve). However, the infinite fiber simulation lacks the resonant coupling between the core mode and the outer diameter of the fiber, resulting in a consistent high power fraction in the core region within the two band gaps.

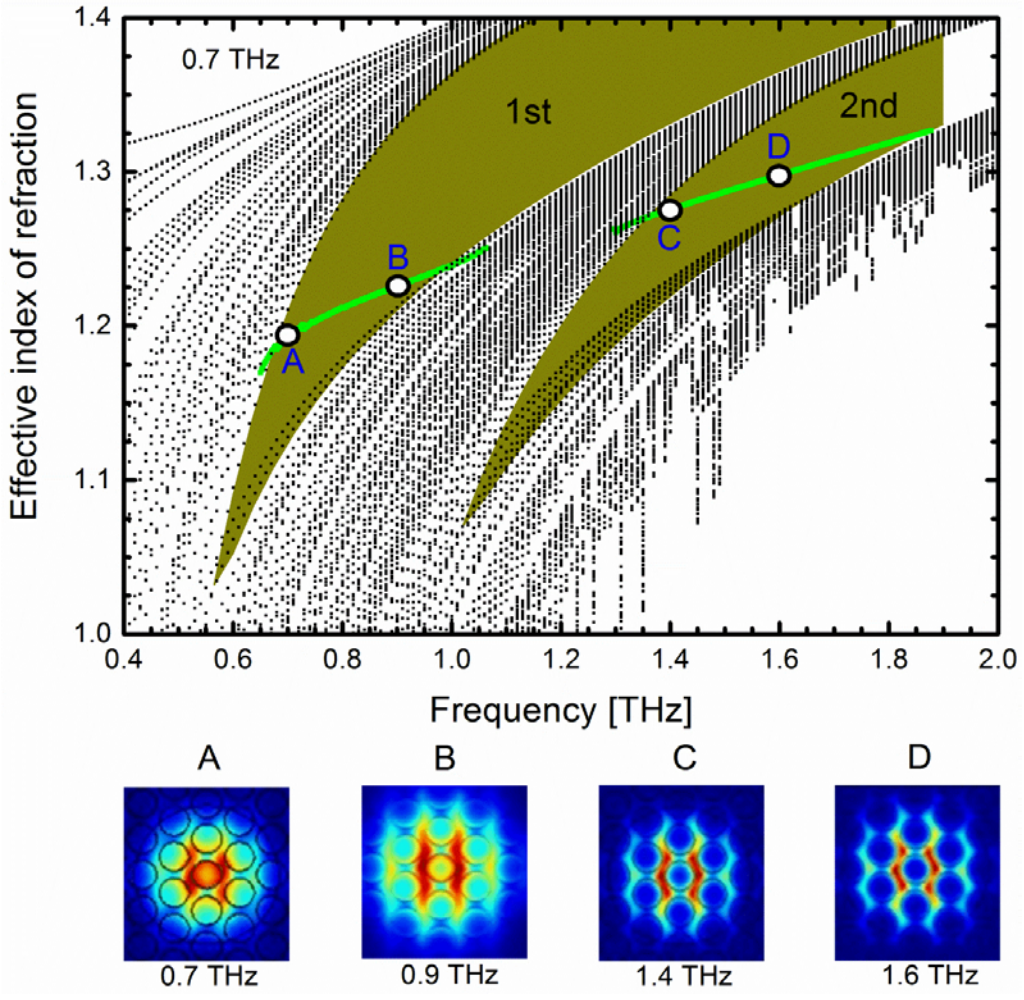

Figure 4.3 Calculated bandgaps (grey zones) and effective index of the fundamental mode (black curves). Insets show the S_z energy flux distribution of the fundamental mode at four different frequencies (0.7, 0.9, 1.4 and 1.6 THz). The scale of each inset is 885×960 µm

For experimental characterization of the fabricated fibers we performed transmission measurements with a commercial fiber-coupled THz-TDS system (Picometrix T-Ray 4000) with an effective spectral range 0.1-2.0 THz, determined by losses in the 1-in. focal length polymer lenses used for focusing of the THz pulses into the TOPAS fibers. The entrance facet of the fiber was placed immediately behind a small, variable aperture (~0.8-0.9 mm diameter) in the focal plane of the tightly focused THz beam. The aperture ensured a preferential excitation of core modes in the fiber. The THz signal transmitted through the fiber was detected by the THz receiver head of the Picometrix system, aligned with the fiber exit facet in its focal plane.

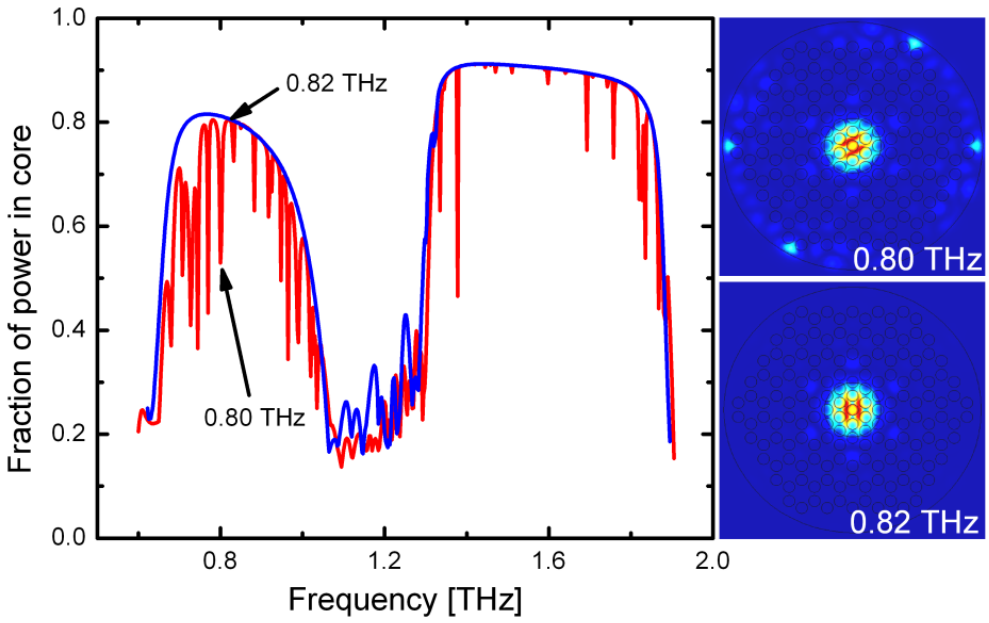

Figure 4.4 Calculated fraction of power localized in the core of the honeycomb fiber with TOPAS (blue curve) and air (red curve) surrounding the fiber surface. The two insets to the right show the S_z energy flux distribution of the fundamental modes at nearby frequencies. One is at a resonant frequency due to reflection from the fiber/air interface (0.80 THz) and the other shows a well-confined mode (0.82 THz). The dimensions of the insets are 3.65×3.65 mm.

The reference pulse transmitted through the aperture is shown in Fig. 4.5(a), and consists mainly of a single cycle of the electric field. The time trace of THz pulses after propagation through a 5-cm long segment of fiber is shown in Fig. 4.5(b) (blue curve). The THz waveform transmitted through the fiber is dispersed in the time domain. As discussed above, we see numerical indication of strong interaction between cladding modes and core modes for finite-diameter fibers. In order to get more detailed information on this coupling we

repeated the transmission experiment while adding some water (a strong absorber at THz frequencies) around the fiber surface. The transmitted pulse in this situation is shown as the red curve in Fig. 4.5(b). We observe significantly less pronounced oscillations at times later than 20 ps, while the initial part of the transmitted pulse is much less influenced by the absorbing water layer around the fiber. Further insight is obtained by performing a short-time Fourier transform (STFT) of the two time-domain traces in Fig. 4.5(b), as shown in Fig. 4.5(c) and (d), representing the transmission through the fiber surrounded by air and water, respectively. The frequencies below approximately 0.6 THz are attenuated by adding a layer of water, while the transmission in the two band gaps in the 0.7-1.1 THz and 1.3-1.7 THz regions are unaffected by the water, clearly demonstrating that the absorptive water layer effectively strips the cladding modes from the fiber.

Based on the effective index shown in Fig. 4.2 we can calculate the arrival time of the various frequency components within the two band gaps after propagation through the 50-mm fiber section. The group delay is given by $t_g = n_g L / c$, where the group index is calculated from the effective propagation index as $n_g = n_{eff} + \nu \cdot dn_{eff} / d\nu$. This group delay is shown in Fig. 4.5(c) and (d) as black squares (identical data sets). There is excellent agreement between the simulated and the observed arrival time of the frequency components, and in particular the experiment reproduces the steep dispersion at the lowest frequencies of the first band gap as well as the delayed arrival of the signal in the second band gap.

Fig. 4.6 quantifies the experimental transmission spectrum after transmission through the 5 cm long fiber segment, calculated as the ratio of the Fourier transforms of the signals in Fig. 4.5(b) and (a). After adding water around the fiber surface to attenuate cladding modes, transmission in the regions outside the band gaps (below 0.6 THz and between 1.1 and 1.3 THz) is reduced (red curve compared to black curve), as already indicated in the STFT trace in Fig. 4.5(d). The location of the two transmission band are in good agreement with the simulation (blue curve), which shows the fraction of the power residing on the core region, and thus indicates confinement of the field by the bandgap effect. The small discrepancy between predicted and observed bandgap positions may be caused by the small non-

uniformity along the fiber length and imperfect uniformity of air-hole diameters across the fiber.

In addition to the detailed methods you need to describe in this section, you need to provide specific objectives and an overview of your approach if they have not already been presented in the introductory chapters. The best place to put those items can vary among theses. Sometimes the background and lit review is really necessary to justify and substantiate the specific objectives and approach and, therefore, it is best to save those details for the beginning of this chapter.

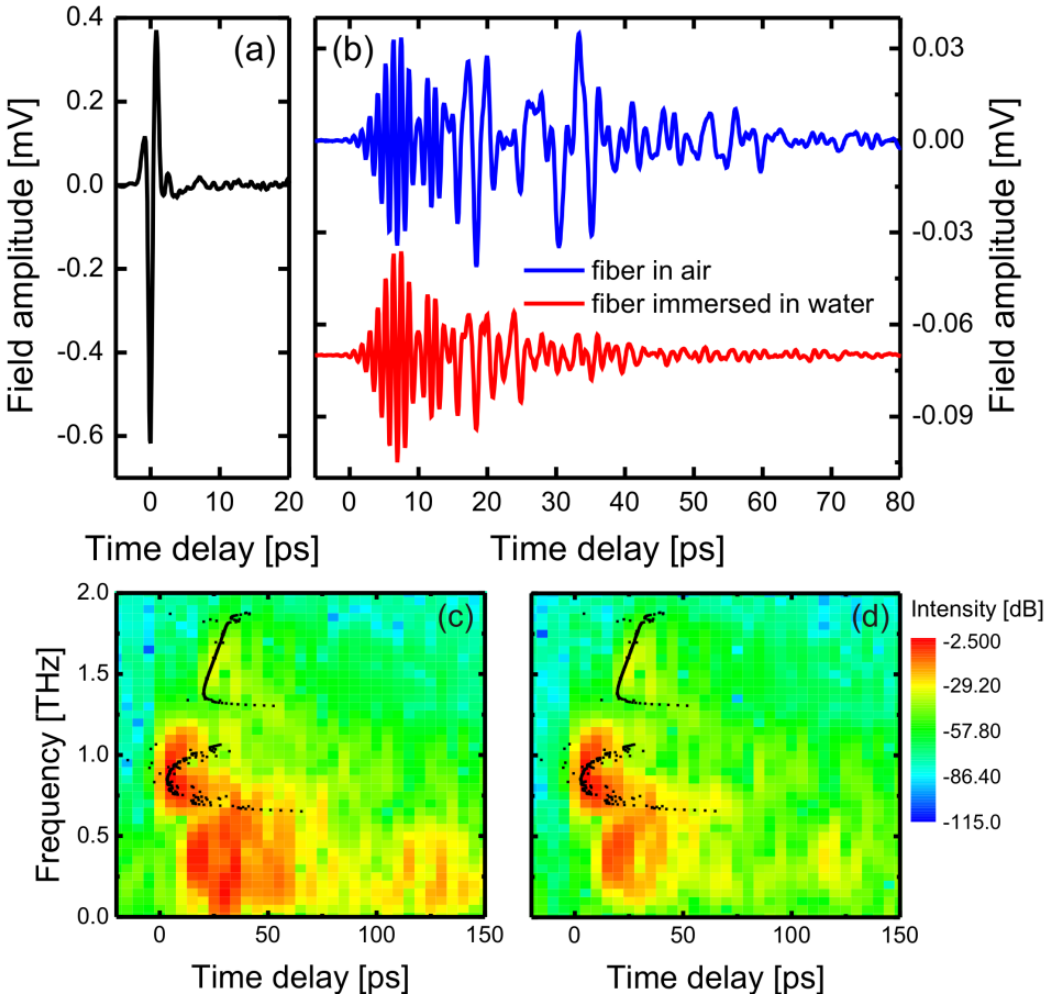

Figure 4.5 Measured THz pulse for (a) reference signal (black curve) and (b) transmitted pulse through a 5 cm long honeycomb fiber with water (red curve) and air (blue curve) around the surface. Short-time Fourier transforms of the transmitted waveforms in (b) are shown in (c) and (d), respectively, with simulated group velocity arrival times of the spectral components overlaid.

Importantly the experimental transmission spectra in Fig. 4.6 (red and black curves) show that transmission in the second band gap is much lower (approximately 9.5 dB) than that of the first band gap. To investigate this strong attenuation we calculated the fraction of power in the polymer material (green circles in Fig. 4.7) and multiplied this fraction with the measured material absorption coefficient (Fig. 4.2) to obtain the effective material loss due to absorption of light in the polymer (red circles in Fig. 4.7). As indicated in Fig. 4.7 we see that the fiber displays much higher material absorption loss (approximately 1.5 dB/cm, corresponding to 7.5 dB for the 5 cm fiber length) in the second band gap compared to the first band gap. The fact that the fraction of power in the polymer and thus the effective material loss is seen to increase with frequency is because of the porous core of our honeycomb bandgap fiber, which confines more and more of the light into the solid material between the holes as the wavelength gets smaller [81, 82]. Additional attenuation may be caused by the smaller overlap integral between the free-space mode and the mode profile in the second band (see Fig. 4.3) compared to the first band gap.

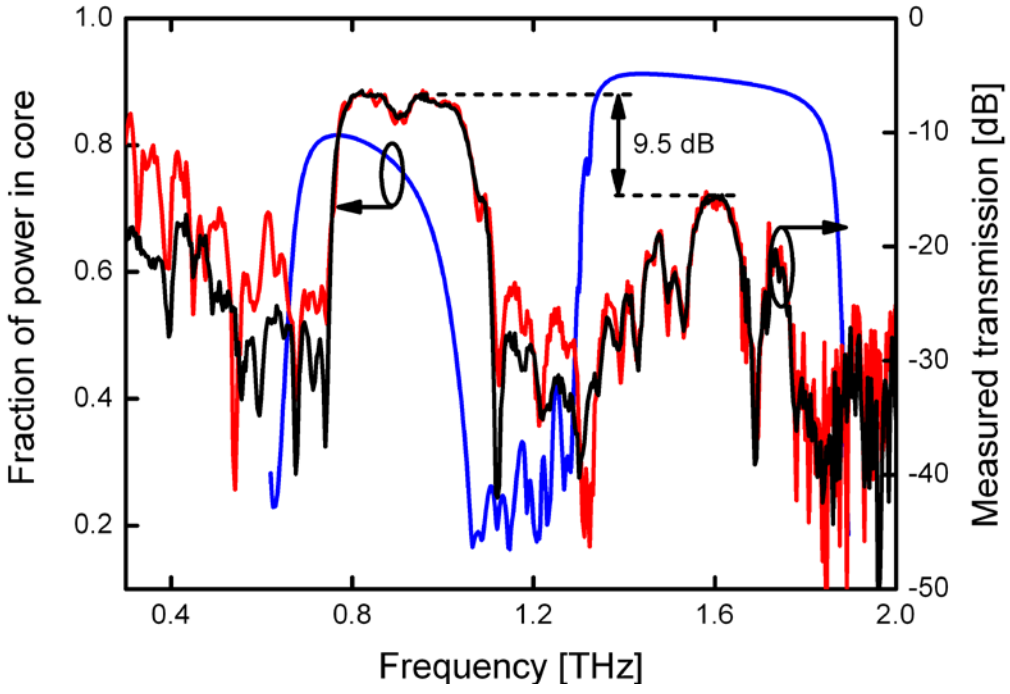

Figure 4.6 Calculated fraction of power localized in the core of the honeycomb fiber with the TOPAS PML (blue curve). Measured relative transmission of the honeycomb fiber with air (red curve) and with water (black curve) around the fiber surface.

Finally we discuss fiber loss measurements. The measurements were performed with a cutback method where transmission was measured on the same piece of fiber (initially 15 cm long), sequentially cut shorter in steps of 2.5 cm and repositioned in the experimental setup. Gentle milling after cleaving assured a uniform and high quality of the cleaved facet at each measurement. Care was taken to assure the same rotational orientation of the fiber at each measurement. Figure 4.8(a) shows the transmission at selected frequencies in the first band gap as function of fiber length. The slopes of the linear fits to these loss data give the propagation loss, as shown in Fig. 4.8(b), and the interception with the ordinate axis at zero propagation distance of the fit curve gives the coupling loss, as shown in Fig. 4.8(c). The error bars indicate the standard deviation of the fit parameters.

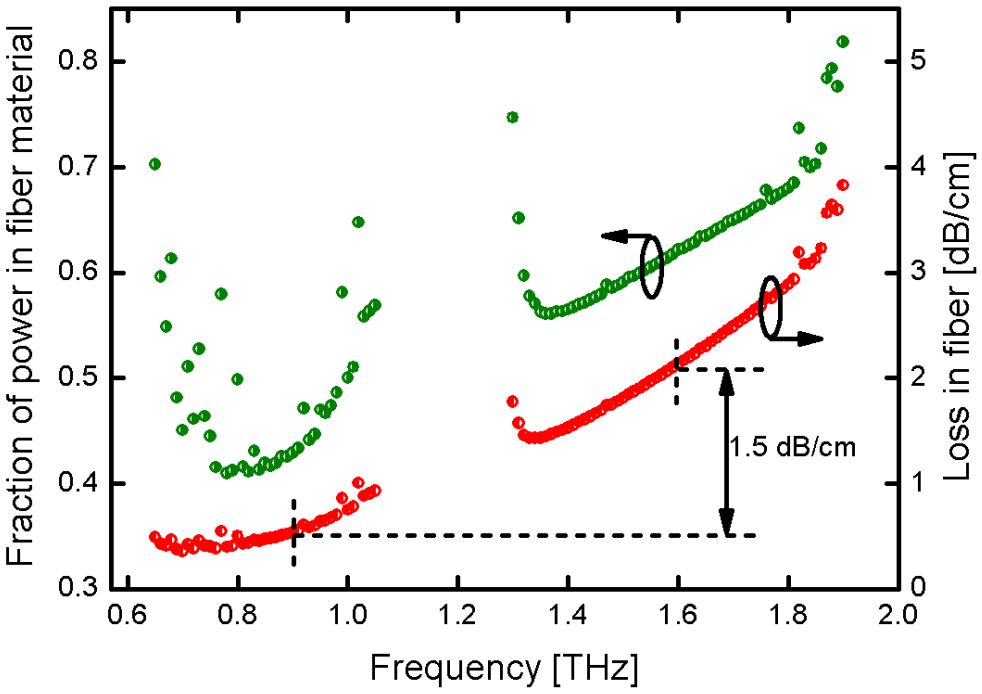

Figure 4.7 Calculated fraction of power in the fiber material (green half-solid circle) and material loss in fiber (red half-solid circle), respectively.

The dips in the transmission spectrum in the second band gap may be caused by interference between the fundamental mode and higher order modes. Such interference is not observed in the first band gap. This may be due to the fact that coupling to the fundamental mode in the second band gap is more sensitive to alignment than in the first

band gap, and slight off-center coupling could lead to an increased fraction of power being coupled into higher order modes.

We find a propagation loss, which is lower than the bulk material loss, as can be expected for the fundamental mode with a significant fraction of power residing within the air holes of the fiber. The modulation of the loss across the band gap is most probably caused by interference with cladding modes also observed in simulation (cf. Fig. 4.4), as the cutback measurements were performed without attempting to attenuate the cladding modes. The frequency-dependent coupling loss shows a maximum of 5 dB at 0.88 THz, coinciding with the small dip in transmission seen in Fig. 6. Outside this region the coupling loss is 2-3 dB, consistent with the overlap integral between a free-space Gaussian beam profile and the fundamental mode of the first band gap (Fig. 4.3).

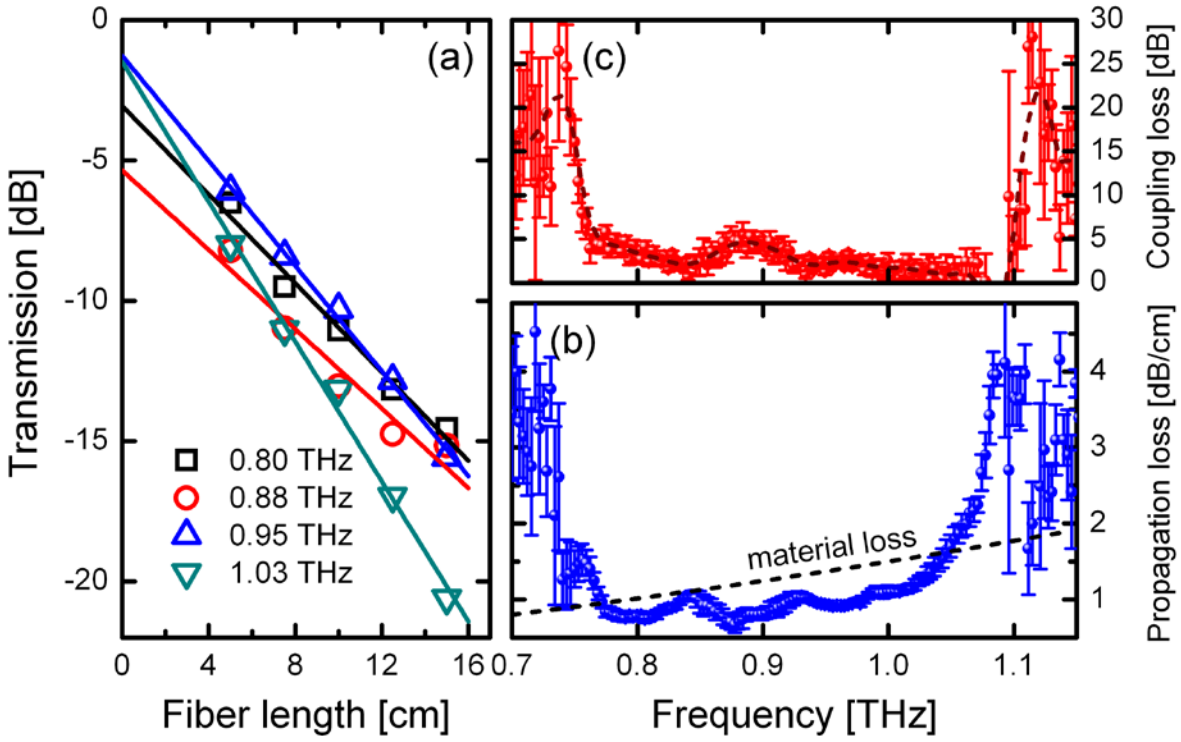

Figure 4.8(a) Relative transmission of the fiber with different lengths together with linear fits at four frequencies (0.8, 0.88, 0.95, 1.03 THz). (b) Frequency dependent propagation loss of the fiber (blue data markers) and material loss of TOPAS (quadratic fit - dashed line). (c) Coupling loss (red symbols) and solid line to guide the eye (running average of 5 data points).

4.4 Summary

In Summary, we have fabricated a low-loss porous-core honeycomb PBG THz fiber with a near perfect hole structure by drill-and-draw technology, and characterized the optical properties of the fiber with experimental THz-TDS techniques and numerical modelling. We demonstrated that the fiber had a fundamental transmission band of 0.78-1.02 THz in which the loss is below 1.0 dB/cm, with the minimum loss of 0.7 dB/cm being at 0.88 THz. The manufactured fiber is not based on an optimized geometry, so we expect that the performance can be improved through optimizing fiber parameters, such as pitch and air-hole diameter.

5 Tube waveguides

5.1 Introduction

Designing compact, broadband, mechanically stable and environmentally shielded THz waveguides is still a challenge due to high losses of both metals and dielectrics in this frequency range. Hollow-core waveguides are deemed as excellent candidates for THz delivering due to the fact that it can confine most power inside the large air (absorption loss can be neglected in THz region) core and thus are very useful in many practical applications. Several designs based on this kind of structure have been proposed, such as photonic band gap (PBG) type fibers [94, 96, 97, 100], Kagome type fibers [106, 107, 138] and metal/dielectric tubes[25, 31, 91, 108, 109, 111, 112]. For PBG type fibers, the mode is confined within the air core with the help of dielectric reflectors or band-gap reflectors, which prohibit the field from extending into the plane of the PBG reflectors. However, the high air filling fraction (photonic bandgap fibers) or high refractive index contrast (Bragg fibers), as well as a strictly periodic cladding structure, are needed to obtain an efficient and broad bandgap[94, 96, 97], which are all factors that increase the difficulty of fabrication. For Kagome-type fibers [106, 107, 138], the cladding can be seen as composed of an array of hollow tubes with different shapes. Porous-core honeycomb PBG fiber can to some extent alleviate such problems but at the expense of bringing more material loss. Unlike the PBG type fibers that guide light by means of a photonic band gap in the cladding, guiding in Kagome-type fibers is based on the inhibited coupling mechanism due to the low density of cladding modes and small spatial overlap of cladding modes with core modes. This kind of guiding usually shows abrupt transmission dips within the transmission band caused by the weak but still finite coupling between core modes and cladding modes.

THz tube waveguides are very simple and normally only consist of a large air-core and a thin dielectric layer[108-110, 112]. The guiding mechanism of the tube waveguides is that of an anti-resonant reflecting optical waveguide (ARROW)[139] with a leaky nature. Low loss has been successfully achieved nearby anti-resonant frequency regions. However, the transmission bandwidth is limited by the spacing of the resonant frequencies, which is proportional to the refractive index and inversely proportional to the cladding thickness. One way to improve the transmission bandwidth is to reduce the cladding thickness.

However, a uniformly thin cladding is in practice difficult to fabricate and cleave due to its low mechanical strength. Moreover, tube waveguides with thin walls are fragile and sensitive to external perturbation, as the propagating mode extends significantly outside the cladding. All these disadvantageous aspects could appear as a limiting factor for many practical applications. Note that the tube cladding layer can also be metal[25] and low loss can be obtained by virtue of its superior reflecting surface for TE modes. However, dispersion is very strong in such waveguides, which limits their use in narrow-band applications. Further improvement for metal tube is to add thin dielectric layer inside the metal tube [27, 34, 140], and they are normally obtained by using the liquid-phase deposition technique, which make the fabrication complex.

In this chapter, three different methods are investigated to improve the transmission bandwidth and dispersion properties, while the propagation loss can be kept generally low. Three methods share the common point, which is to prevent the propagating field in the cladding to be reflected back into the core where it otherwise would interfere with the core mode by the normal ARROW mechanism.

5.2 Dielectric tube waveguides with absorptive and uniform cladding

Here we present a new class of THz tube waveguides where we deliberately introduce a high-loss, thick cladding, which serves to absorb the propagating field in the cladding and thus prevents it to be reflected back into the core where it otherwise would interfere with the core mode by the normal ARROW mechanism. A very broad transmission band and low dispersion can be obtained, while at the same time The propagation loss can be kept low due to the high (although not total) reflection that occurs at the core-cladding interface. Moreover, the proposed tube waveguide is robust, insensitive to external perturbations and easy to handle. Finally, bending loss of this tube is also investigated. We use a combination of simulation approaches based on both the Finite Element Method (FEM) and the analytical Fabry-Perot (F-P) model, and experimental characterization with terahertz time-domain spectroscopy (THz-TDS) to verify our findings. Briefly, the F-P model uses the calculated

modal index of refraction (the effective index) to calculate the frequency-dependent attenuation of a tube waveguide, based on the total number of bounces of the electric field in the cladding of the material.

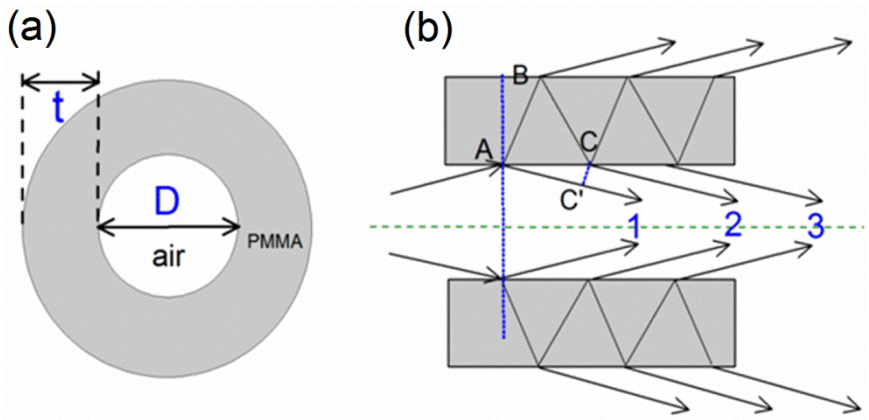

Figure 5.1 Profiles of the (a) PMMA tube waveguide and (b) F-P etalon.

5.2.1 Waveguide principle and PMMA characterization

Fig. 5.1(a) shows the cross section of a PMMA tube waveguide. It has an air core with diameter *D* surrounded by a cladding layer with thickness *t*, the cladding layer is made of standard Poly(methyl methacrylate) (PMMA). PMMA is specifically chosen because of its high loss, as compared to for example the low loss cyclic olefin copolymers, such as TOPAS and ZEONEX. The tube waveguide can be described by the ARROW guiding mechanism and its cladding effectively forms an F-P etalon with frequency spacing given by the inverse of its optical thickness. A cross section along the tube waveguide is shown in Fig. 5.1(b). The light propagates at an angle θ_1, defined by $\sin\theta_1=n_{\text{eff}}/n_{\text{core}}$, with respect to the normal of the core-cladding interface. Both reflection and transmission occur at the interface between the core and cladding. The reflected part of the light continues to propagate in the core. The part of the light transmitted into the cladding bounces back and forth between the outer and inner interfaces of the cladding, thereby gradually losing its energy to the surrounding and gradually leaking back into the core where it can interfere with the core mode. In the following, we refer to the light that always propagates inside the core, as the first order pulse. The light that experiences a single F-P reflection in the cladding is referred to as the

2nd order pulse, and higher-order reflections from the cladding that experience *n* times F-P reflection is defined as the pulse of order (n-1).

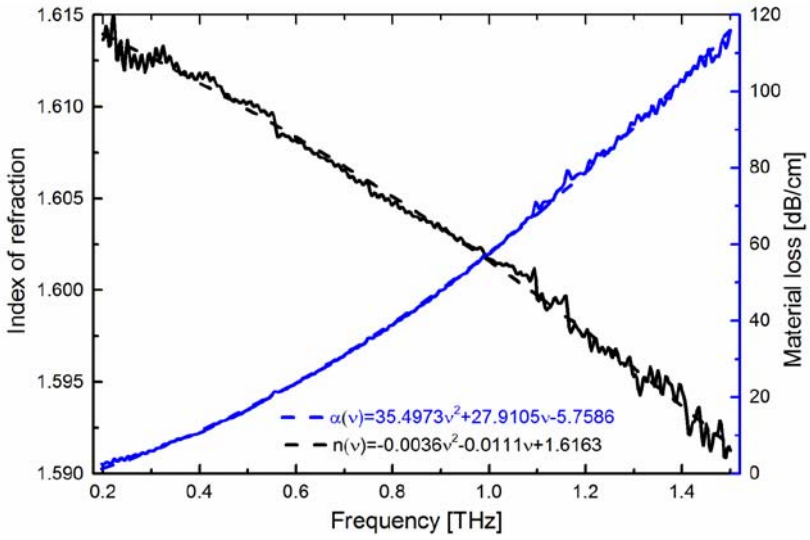

Figure 5.2 Refractive index (black curve) and material loss (blue curve) of the PMMA polymer experimentally measured on a disk with thickness of 1.02 mm. Dashed curve is a phenomenological quadratic fit to refractive index ($n(\nu)=-0.0036\nu^2-0.0111\nu+1.6163$) and loss ($\alpha(\nu)=35.4973\nu^2+27.9105\nu-5.7586$), respectively, used in the simulations.

In order to make a precise and quantitative comparison between experiment and simulation, the bulk dielectric properties (absorption coefficient and refractive index) of PMMA are characterized via THz-TDS using a disk with a thickness of 1.02 mm. The frequency-dependent absorption coefficient and index of refraction are shown in Fig. 5.2. We observe a monotonically increasing absorption coefficient and monotonically decreasing index of refraction with increasing frequency. For the purpose of numerical modeling, a simple polynomial fits to the experimental data (dashed curves in Fig. 5.2 with fit parameters indicated in the caption) are used for representation of the dielectric properties. As can be seen, the material loss of PMMA is significant (approximately 60 dB/cm at 1 THz). 2nd order pulse, and higher-order reflections from the cladding that experience *n* times F-P reflection is defined as the pulse of order (n-1).

5.2.2 Simulations of straight tube waveguides.

We now investigate the transmission properties of straight THz tubes. Our numerical results are based on two methods. We find the effective index of the fundamental mode and the

transmission spectrum using the Finite Element (FEM) method and the overlap of the mode with the lossy material (see methods). Correspondingly, we also simulated the transmission properties of the THz tubes using the F-P model and the effective index n_{eff} found from the FEM modeling. Results obtained from the two methods agree well with each other.

Following Lai *et al.* [109], for each polarization component (TE and TM) of the fundamental, hybrid waveguide mode, the F-P model uses the reflection coefficient from the cladding,

$$R = \left| r_{12} - \frac{t_{12} r_{23} t_{21} e^{i 2\omega n_2 t \cos\theta_2 / c} e^{-\alpha_2 t / \cos\theta_2}}{1 - r_{23} t_{21} e^{i 2\omega n_2 t \cos\theta_2 / c} e^{-\alpha_2 t / \cos\theta_2}} \right|^2 , \quad (5.1)$$

Where ω is the angular frequency, t_{12}, r_{23}, t_{21} are the standard complex-valued Fresnel coefficients for transmission from air core (medium 1) to cladding (medium 2), reflection at the outer interface of the cladding (medium 3 is the surrounding air), and transmission back into the air core, respectively, n_2 and α_2 are the bulk refractive index and absorption coefficient of the cladding, respectively (see Fig. 5.2), $\theta_2 = (1 / n_2)\sin^{-1}\theta_1$, and the incident angle, defined from the effective index, is $\theta_1 = \sin^{-1}(n_{eff})$ for an air core fiber (n_1 = 1). The effective loss is then calculated as

$$\alpha = -\frac{\ln R}{D \tan\theta_1} . \quad (5.2)$$

The total loss is calculated as the average of the TE and TM losses.

In order to demonstrate the effect of cladding material loss on the THz tube transmission, Fig. 5.3(a) shows the fundamental mode for various values of cladding material absorption. Specifically, we numerically vary the cladding material loss (the imaginary part of the refractive index) while keeping the real part of the refractive index constant. As can be seen in Fig. 5.3(a) the transmission loss maxima and minima positions, are determined mainly by the real part of the refractive index of the cladding through the relation

$$f_m = \frac{mc}{2t\sqrt{n_2^2 - 1}} , \quad (5.3)$$

and remain almost constant, whereas the overall oscillation amplitude decrease with increasing material loss of the cladding. The F-P model explains this behavior in physics terms. The bouncing cladding field passes through the more lossy cladding material and thus less power is transmitted back to the core to interfere with the direct transmitted field. Figure 5.3(b) shows three examples of the calculated effective index of the tube from Fig. 5.3(a), and it can be seen that the slope (absolute value) of the effective index becomes smaller with increasing cladding loss, especially in the vicinity of the resonant loss maxima. Consequently, the corresponding group velocity dispersion (GVD), shown in Fig. 5.3(d), becomes much smaller with increasing cladding loss. Particularly, extremely low dispersion over the full frequency range can be obtained for a highly absorptive cladding material, effectively eliminating all the fields propagating through the cladding part. The tube dimensions in Fig. 5.3(a), (b) and (d) are constant with core diameter D = 4 mm and cladding thickness t = 1.29 mm.

Alternatively, a similar effect can also be achieved by increasing the thickness of the lossy cladding. Figure 5.3(c) shows the transmission loss of the tube with three different cladding thicknesses, together with the calculated loss for an infinite cladding. In addition to the trivial observation that the loss maxima and minima shift toward lower frequencies with increasing cladding thickness (see Eq. (3)), the oscillation amplitudes display the same trend as the results shown in Fig. 5.3(a) and become smaller.

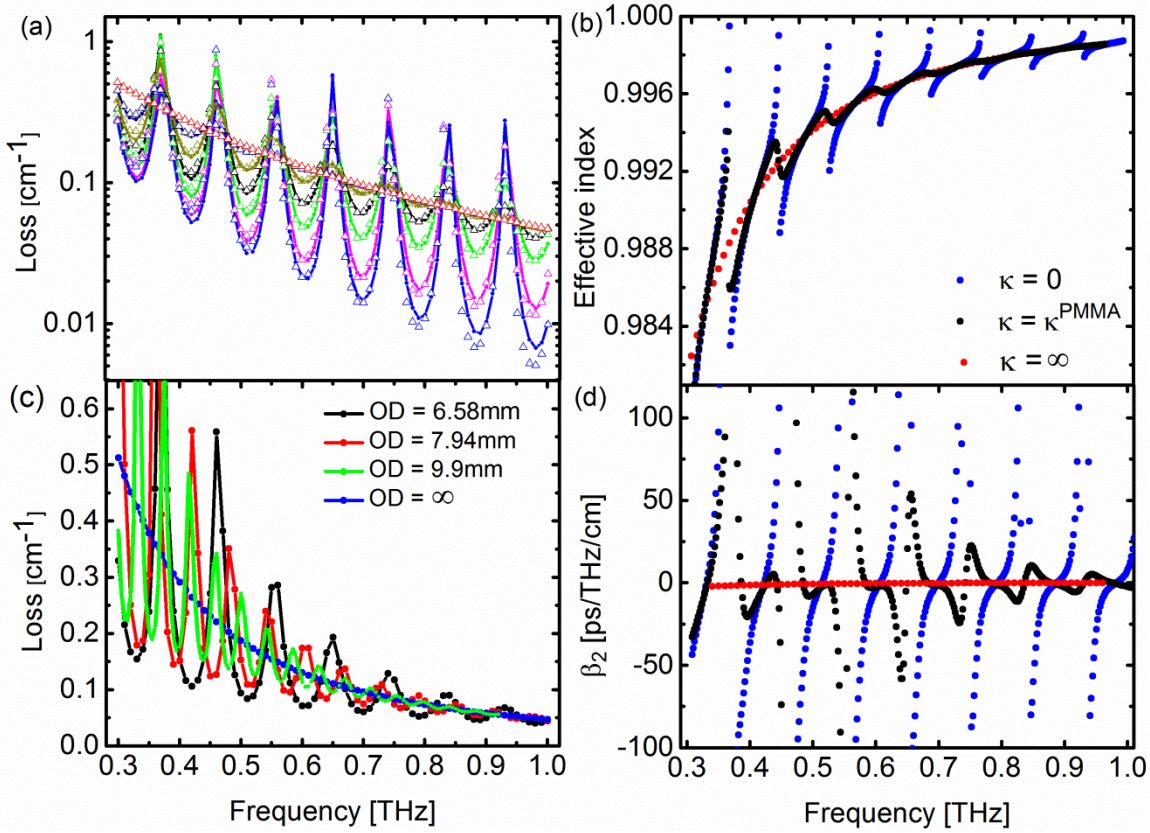

Figure 5.3 (a) Simulated propagation loss of the fundamental core mode with constant real part of index of refraction and different loss values κ/κ^{PMMA} (0 – blue; 1/8 – magenta; 1/2 – green; 1 – black; 2 – brown; 4 – navy; ∞ - red). Lines and symbols represent FEM simulation and F-P model, respectively. (b) Calculated effective index of the fundamental mode for the tube with three different loss values κ/κ^{PMMA}. (c) Simulated propagation loss of the fundamental core mode with different cladding thicknesses and constant core size. (d) Calculated group velocity dispersion for the effective indices in (b). Core diameter of all tubes is D = 4 mm.

5.2.3 Experimental characterization of straight tube waveguides

We perform transmission measurements on straight segments of PMMA tube waveguides using a commercial fiber-coupled THz-TDS system (see methods). We label the tubes with three different cladding thicknesses t = 1.29, 1.97, 2.95 mm as tube 1, 2 and 3, respectively. Measurements are performed on tubes with different lengths (10, 20, 30, 40 cm for tube 1 and 2, and 20, 30, 40 cm for tube 3).

Figures 5.4(a-c) show the temporal traces of the THz pulses guided through three PMMA tubes with the same air core size (D = 4 mm) and different cladding thicknesses t = 1.29,

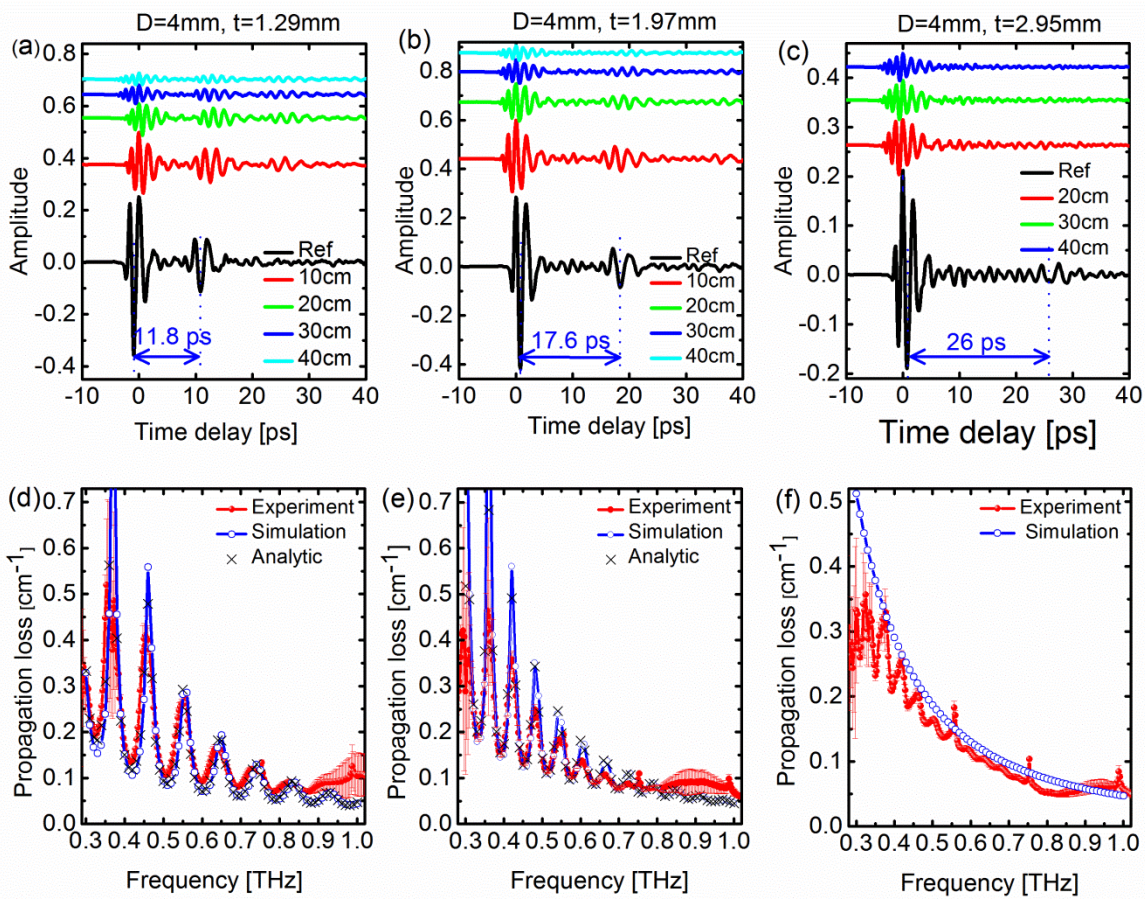

Figure 5.4 (a) (b) (c) Measured time-domain THz signals, and (d) (e) (f) propagation loss averaged over the different propagation lengths of three PMMA tubes (D = 4mm) with various cladding thicknesses t. For tube 1 (t = 1.29 mm) and tube 2 (t = 1.97 mm), using transmission through a 5 cm tube as reference (black curves in (a) and (b), respectively). For tube 3, the transmitted THz signal through 10 cm tube is used as reference. Blue arrows indicate the time delay between the first and second order pulses of each tube. Red error bars in (d) (e) (f) represent the standard deviation between several scans of each tube with different lengths. The blue curve with circle symbols represents FEM simulations, and crosses represent the analytic F-P model.

1.97, 2.95 mm. Several pulses are visible in the temporal traces for each tube, corresponding to different orders of the pulses reflected in the cladding. For each tube with different lengths, the temporal delay between adjacent orders is constant, with a time difference proportional to the cladding thickness. This behavior is attributed to the same transmitted path difference between the adjacent orders of pulses in the cladding, which can be expressed as $\delta L = AB + BC - AC' = 2n_2 t\cos\theta_2$ (see Fig. 5.1(b)). The time delay between the first and second-order pulses in tube 1, 2 and 3, indicated with blue arrows in Figs. 5.4(a), (b) and (c), are 11.8 ps, 17.6 ps and 26.0 ps, respectively, in agreement with the theoretical value

$\Delta t = 2n_2 t \cos\theta_2 / c$, which is constant within less than 0.2 ps in the frequency range considered here due to the very low dispersion of the refractive index of PMMA. Figures 5.4(d), (e), and (f) show the corresponding propagation loss of the three tubes. Red symbols represent the average value of the experimentally determined loss, based on several measurements on each tube with different lengths. The red error bars indicate the standard deviation of the measurements. The simulated losses, based on the FEM simulation (blue circle + line) and the F-P model (black cross), are shown for direct, quantitative comparison. Within the frequency range from 0.3 to 0.85 THz we find a very close agreement between experiment and simulation, except at the loss maxima where the experimental noise is significant due to low transmitted signal strength. The slight deviation between experiment and simulation at the highest frequencies above 0.9 THz is in part caused by low signal-to-noise ratio in the experiments, but may also be caused by reduced coupling efficiency from the reference tube to the measured tubes at large frequencies. As predicted by simulations, the experimental results clearly show that the oscillation amplitudes decrease with increasing cladding thickness. For the 2.95-mm thick cladding, the F-P oscillations in the loss spectrum are almost completely suppressed, resulting in a smooth loss curve very close to the simulated loss for an infinite cladding. However, the outer diameter of this waveguide is 9.9 mm, which for some practical purposes may be too bulky. As an alternative method, the cladding fields can be further suppressed by adding a thin, strongly absorbing layer to the outside of a tube with a thinner cladding.

5.2.4 Bend loss.

Another important parameter associated with THz waveguides is bending loss. The numerical analysis of the bending is performed by employing an equivalent index profile[59] given by $n'(x,y) = n(x,y)e^{x} / R_{bend}$. Here $n(x,y)$ is the index profile of the straight tube waveguide and R_{bend} is the bend radius. In the following, x represents the bending direction. Figures 5.5(a) and (b) show the geometry and refractive index profile, respectively, of the bent tube. Figures 5.5(c) and (d) show the simulated transmission loss of tube 1 using the same value for the real part of the refractive index but three different values for the imaginary part ($\kappa = 0$, $\kappa = \kappa^{PMMA}$, and infinite cladding) at three different bending radii

($R_{bend} = \infty$, $R_{bend} = 30$ cm, $R_{bend} = 10$ cm, respectively) and with polarizations perpendicular (Fig. 5.5(c)) and parallel (Fig. 5.5(d)) to the bend direction. The general trend is the expected behavior that the bend loss increases with decreasing bend radius. We also see that the frequency positions of loss minima and maxima are the same for the tubes with and without bend loss, and that the loss minima and maxima shift towards lower frequencies as the bend radius is decreased, due to the increased effective cladding thickness after bending. Losses are higher for the parallel polarization than for the perpendicular one, with the higher frequencies being more sensitive to bending than the lower frequencies. Similar to the straight tube transmission loss, the oscillatory features in the bend loss spectrum can also be suppressed if perfectly matched boundary conditions are applied to the outer surface of the cladding, thereby mimicking an infinite cladding. Figure 5.6 shows the intensity profiles of the fundamental mode at 0.740 and 0.805 THz, corresponding to resonant (low loss) and anti-resonant (high loss) frequencies for the straight tube 1, respectively, for straight and bent ($R_{bend} = 10$ cm) tubes at two polarizations, and with and without inclusion of loss. To illustrate the phenomenon of the shift of the maxima and minima of the loss curve, we focus on the simulation without cladding loss, as the visual difference between the intensity distributions for the resonant and anti-resonant cases is most clear. The sub-figures in first and third columns of Fig. 5.6(a) show that when the tube is bent, the resonance (0.740 THz) of the straight tube experiences a shift towards the anti-resonance frequency region, and the anti-resonance (0.805 THz) becomes a resonant frequency region. The simulations with cladding loss included show that the guided intensity becomes more concentrated in the tube core, thereby reducing the cladding interference behavior and thus resulting in a less pronounced difference in the power distribution between the resonance and anti-resonance case.

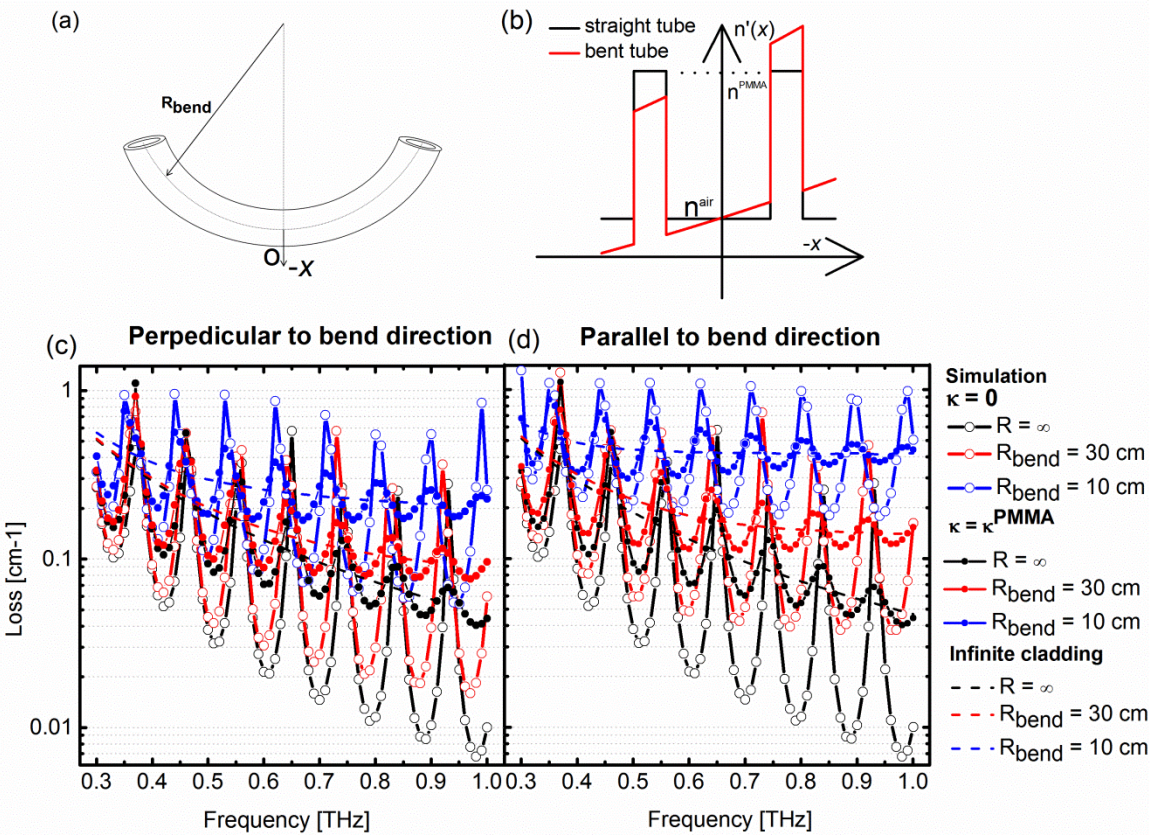

Figure 5.5 (a) Geometry and (b) effective refractive index profile of the bent tube. Simulation of propagation loss of tubes (ID = 4 mm, OD = 6.58 mm) with different bending radii for two polarizations (perpendicular (c) and parallel (d) to bend direction) at various values of κ.

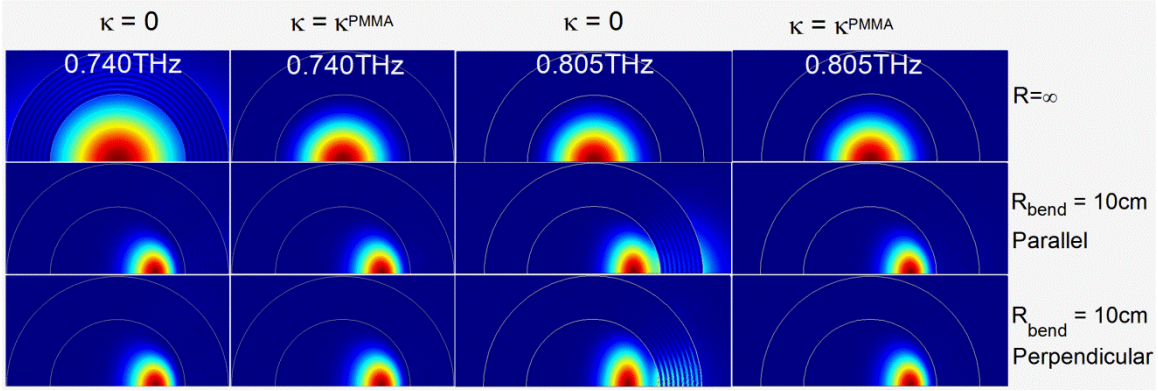

Figure 5.6 Calculated intensity distribution of fundamental mode of straight tube and bent tube for the tube with two different loss values for the two polarizations.

Figures 5.7 (a) (b) and (c) (d) present the experimental temporal scans of guided THz pulses and the corresponding propagation loss through three tubes with different bending radii ($R_{bend} = \infty$, $R_{bend} = 30$ cm, $R_{bend} = 10$ cm , respectively) and with polarizations parallel and

perpendicular to the bending direction, respectively. Figures 5.8(c) and (d) show the bend losses, calculated as the ratio of the transmitted spectrum through the bent and the straight tube. The solid curves are experimental results for the two polarizations. Together with the experimental results we show the simulated bend losses (solid dots) and in general see excellent agreement. The bend losses are negative at some frequencies. This is because the maxima and minima of the loss curves shift slightly with bend radius, as discussed above, leading to oscillations in the bend loss spectra.

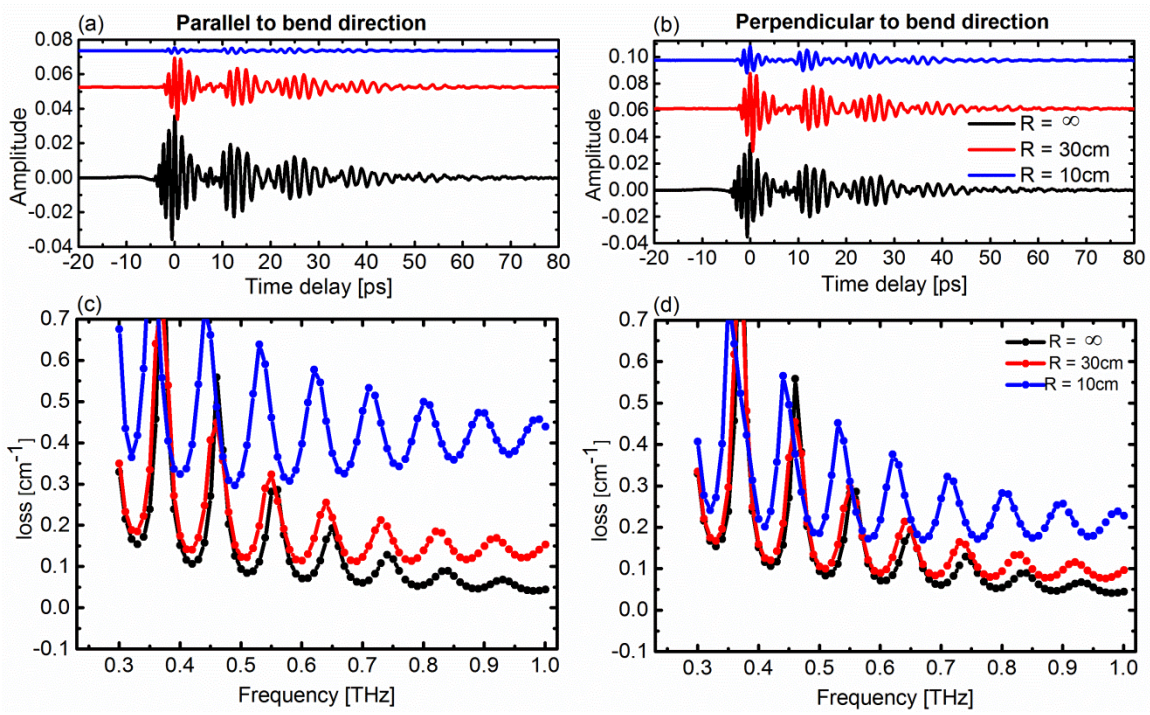

Figure 5.7 (a) (b) Measured time-domain THz signals, and (c) (d) propagation losses of 30 cm tube sample (ID = 4 mm, OD = 6.58 mm) with 18 cm bend length for different bending radii for two polarizations, parallel and perpendicular to the bend direction.

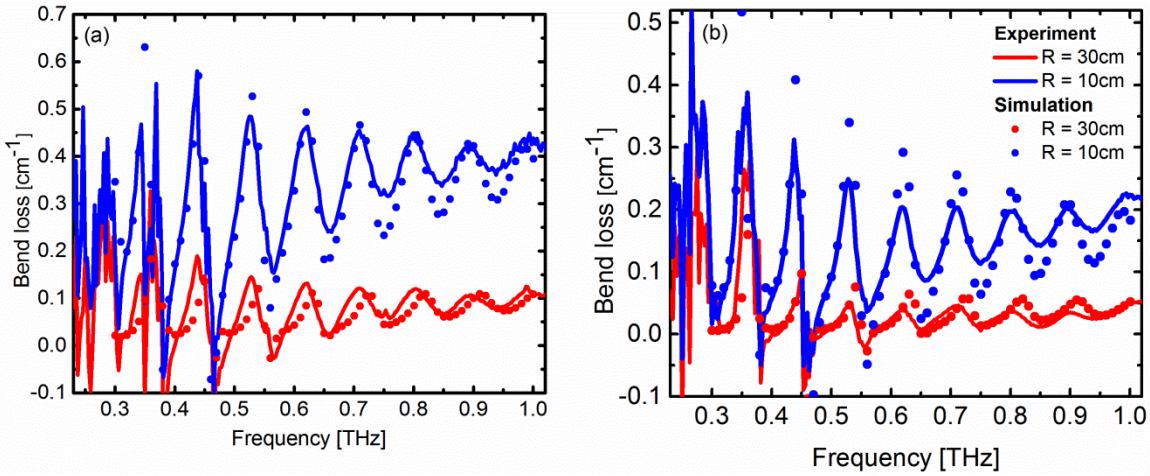

Figure 5.8 (a) (b) Measured bend losses of 30 cm tube sample (ID = 4 mm, OD = 6.58 mm) with 18 cm bend length for different bending radii for two polarizations, parallel and perpendicular to the bend direction, with the simulated bend losses overlaid on the experimental values.

5.3 Added water effect around the tube surface

For the 2.95-mm thick cladding, the F-P oscillations in the loss spectrum are almost completely suppressed, resulting in a smooth loss curve very close to the simulated loss for an infinite cladding. However, the outer diameter of this waveguide is 9.9 mm, which for some practical purposes may be too bulky. As an alternative method, the cladding fields can be further suppressed by adding a thin, strongly absorbing layer to the outside of a tube with a thinner cladding. To investigate this idea, we performed an experiment where a thin layer of liquid water was added around the thinnest tube waveguide. Water has a very strong absorption in the THz range ($\alpha \approx 225$ cm^{-1} at 1 THz) and a refractive index matched reasonably well with the PMMA cladding ($n \approx 2.05$ at 1 THz)[141] for high transmission of the THz. These properties make a water layer around the tube a close experimental analog to perfectly absorbing layers in simulations, and thus the water layer should mimic an infinite cladding. In addition to the trivial index-matching properties, the introduction of a high-index, absorptive layer outside the cladding introduces a sign reversal of the reflection coefficient between the TE- and TM components of the THz field, leading to effective cancellation of the F-P oscillations in the fundamental waveguide mode which is a hybrid between the TE and TM modes. For these reasons we therefore repeat the transmission

experiment on tube 1 with lengths 20 and 40 cm and with a 1.7-mm thick water layer surrounding the tube external surface. The temporal scans of the guided THz pulses in this situation are shown in Fig. 5.9(a) and they show a prominent suppression of higher-order pulses. The suppression increases with pulse order due to the absorption at each of the multiple reflections at the outer surface of the cladding. In contrast to this behavior we observe that the main pulse, propagating in the core of the tube, is virtually uninfluenced by the added absorptive layer surrounding the cladding. Figure 5.9(b) shows the measured propagation loss for the two tube lengths with and without water jacket, together with the result of an F-P calculation using the dielectric function of water. We see a good agreement between the measurements and the calculations.

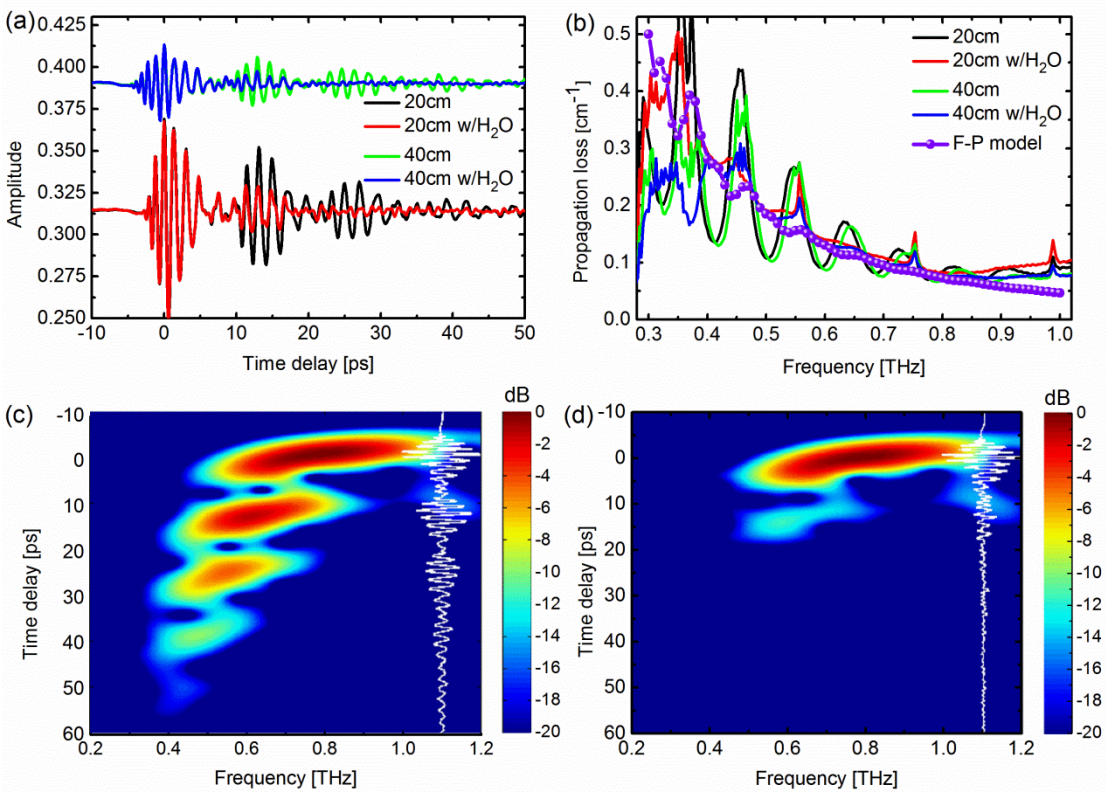

Figure 5.9 Measured (a) transmitted pulses and (b) propagation loss for 20 and 40 cm tubes (using transmission through 5 cm tube as reference) with and without water around the tube surface. (c) and (d) show spectrograms (short-time Fourier transforms) of the time traces through 40 cm tube without and with water around the tube surface, respectively, with overlaid time traces of the transmitted pulses.

Further insight is obtained by performing a short-time Fourier transform (STFT) of the time-domain traces of 40 cm tube without and with water around the tube external surface, resulting in the spectrograms shown in Fig. 5.9(c) and (d), respectively. In Fig. 5.9(c), both the high and low frequency edges of each subsequent higher-order pulse shift toward progressively lower frequencies. The high-order pulses experience longer interaction with the lossy cladding material, resulting in increased loss especially at the higher frequencies. The red-shift of the low-frequency edge of the higher-order pulses is due to high coupling from the core to the cladding, combined with relatively low propagation loss in the cladding material at the lowest frequencies. Again it is observed that after adding water, the main pulse is virtually unaffected while strong attenuation occurs for high order pulses.

5.3.1 Effective index and group velocity dispersion

The frequency-dependent phase and effective index information are determined by the measured data from THz-TDS measurements (see Methods). The simulated (black curve) and experimental (blue dash) effective index for tube 1 without and with water around the cladding are shown in Fig. 5.10(a) and Fig. 5.10(b), respectively. The experimentally determined effective index in Fig. 5.10(a) is obtained by taking the average of the four individual measurements of the index on different lengths of tube 1 (without water around cladding), and in Fig. 5.10(b) are the average of the two individual measurements of the index on different lengths of tube 1 (with water around cladding). We find excellent agreement between simulation and experimental results.

The group velocity dispersion (GVD), $\beta_2 = (\nu \partial^2 n_{eff} / \partial \nu^2 + 2\partial n_{eff} / \partial \nu) / 2\pi c$, is obtained from the experimental effective index for tube 1 without and with water around the tube external surface. The results are also shown as red symbols in Fig. 5.10(a) and (b), respectively. Since the calculation of β_2 involves the second derivative of the effective index, the calculated results are sensitive to experimental noise, and thus the GVD data shown here are averages over result for tubes with different lengths, and a running average of 5 data points has been applied. The GVD data from experiments follows the pattern of the simulated values (black symbols). We observe that much lower GVD values can be obtained after adding water around the tube external surface, with only slight deviations from the

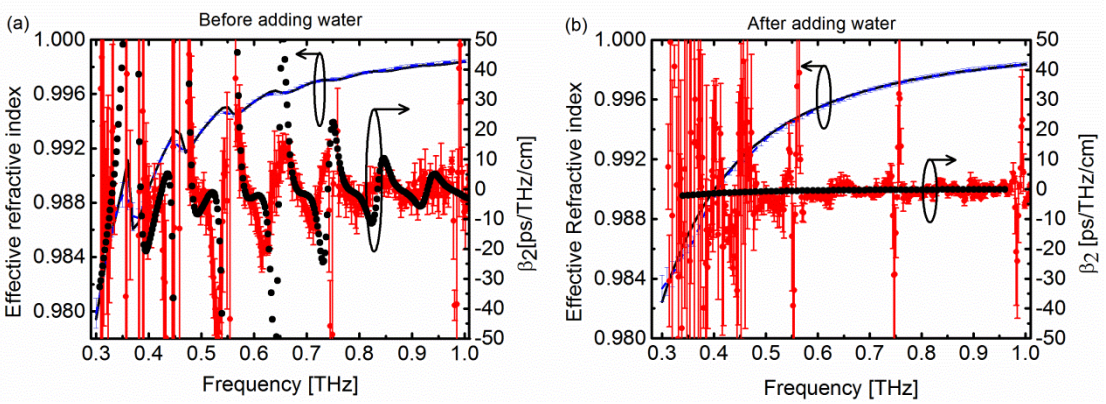

Figure 5.10 Simulated (symbols) and measured (curves) effective refractive index and GVD parameter β_2 of tube 1 (a) before and (b) after adding water around the surface. The measured indices in (a) and (b) are the average indices of four different lengths of the tube (before adding water) and two different lengths of the tube (after adding water) and β_2 is the average value of the running average of 5 frequency data points for each length of tube.

ideal simulation scenario with an infinite cladding, mainly due to the incomplete absorption of the second and third order pulses in the cladding.

5.3.2 Explanation of added water effect

In order to more clear about the effect of the added water around the tube surface to the transmission, we calculate the attenuation of the tube waveguides with respect to TE, TM and fundamental Hybrid modes by using F-P model. Fig. 5.11(a) and (b) shows the loss information of the tube waveguides before and after adding the water layer. For the tube waveguide without water jacket, TM and TE modes have the same resonant and anti-resonant frequencies due to the fact that TE mode related s-polarized light and TM mode related p-polarized light experience the same phase shift after experiencing specific times F-P reflections, resulting in same period loss dip and peak frequency positions. Situation is different for the waveguide with water jacket around its surface, TE mode related s-polarized light experience π phase shift at the interface between the cladding and outside medium, while TE related p-polarized light experience no phase shift, and this can be known from the basic Fresnel co-efficiency. Converted to frequency domain, frequency positions with respect to dips and peaks are reversed for TE mode while are kept the same for TM mode. For fundamental hybrid mode, which is calculated by the average of TE and TM

modes, the loss curve will become very smooth, this can be seen from the green curve in Fig. 5.11(a) and (b).

Since water has a very strong absorption in the THz range ($\alpha \approx 225$ cm^{-1} at 1 THz) and the imaginary part of the added water cannot be neglected during the calculation to the tube waveguides transmission. To see the effect of the water imaginary part value to the tube transmission, we repeat the F-P model calculation with the consideration of the imaginary part of surrounded water, the loss dips and peaks with respect to TE and TM modes shift towards to higher frequency region but almost the same shift, thus the loss curve of fundamental hybrid mode can be still kept smooth, which can be seen green curve from Fig. 5.11(c). Such phenomenon can be explained by the fact that both the TE related s-polarized and TM related p-polarized light experience the same phase shift after the consideration of the added water with its imaginary part value.

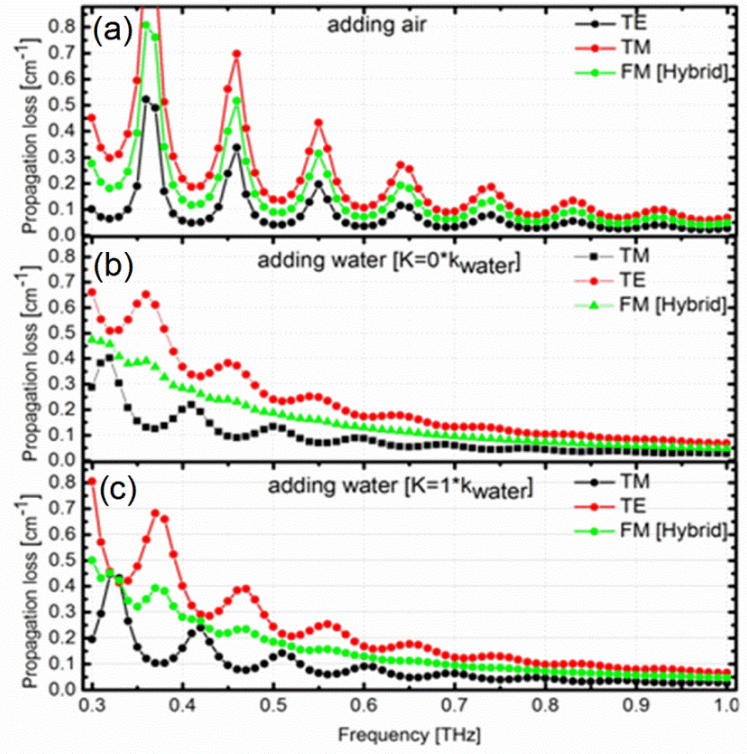

Figure 5.11. Loss spectra of the tube waveguides based on F-P model calculation without and with adding water for the lowest order group modes. (a) before adding water and after adding water (b) without and (c) with the consideration of imaginary part of water.

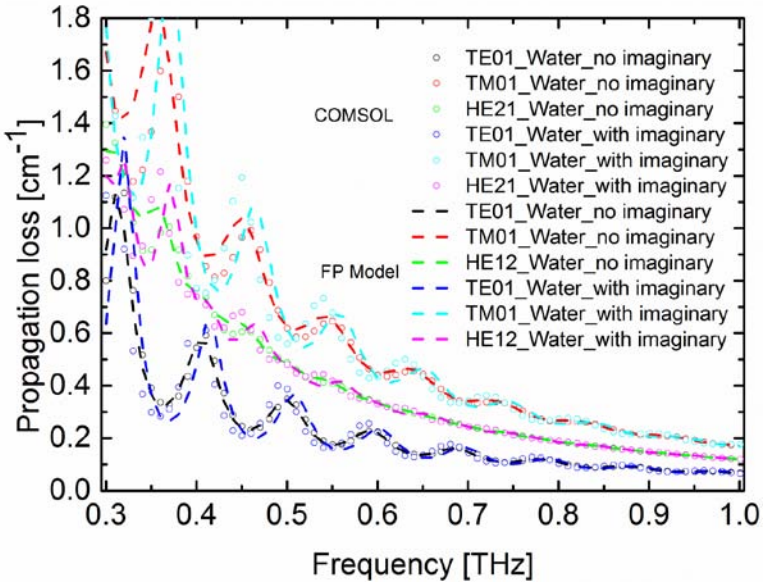

Figure 5.12. Loss spectra of the tube waveguides without and with adding water (with and without the consideration of water imaginary part value, respectively), for the TE01, TM01 and HE21 modes, by using F-P model and FEM method.

The validity of the F-P calculation is also checked by using commercial available FEM solver (COMSOL 3.5a). Noted that the lowest order group modes of the tube waveguides [The modes with similar effective index] only have hybrid modes, they are hybrid modes at two polarizations. So simulation is focused on the second lowest group modes involved TE TM and hybrid modes (TE_{01}, TM_{01} and HE_{21}). The results are shown in Fig. 5.12 with the F-P calculations overlaid. Not surprisingly, agreement between each other is perfect, which means the F-P calculation is valid.

5.4 Tapered tube waveguides

For the above proposed tube waveguides, we have to employ highly absorbing cladding material or add another medium so that can highly suppressed the echoes, which result in broadband guidance. To break this limitation, a novel class of tube waveguides consist of a uniform air-core and a cladding layer with tapered thickness are designed and demonstrated. Thanks to the introduction of taper cladding, even though low material loss of the cladding have been employed, echoes can be suppressed thus weaken Fabry-Perot (F-P) interference, thus the same effect of the highly absorbing cladding material can also be obtained. Properties such as broadband, generally low loss and low dispersion can be also

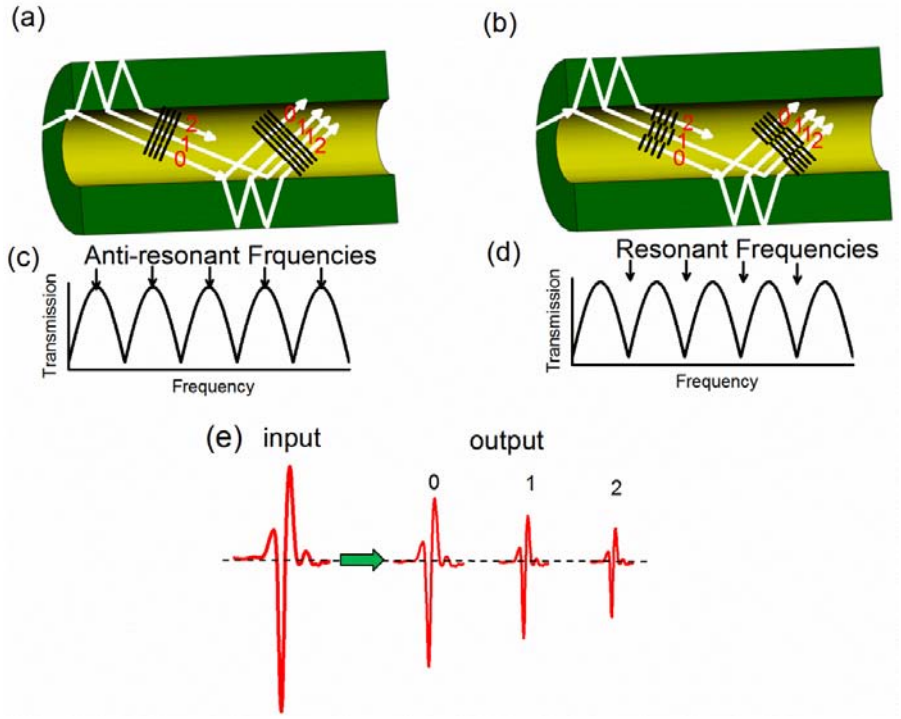

Figure 5.13 Profiles of the uniform tube waveguides at anti-resonant (a) and resonant (c) frequencies. Spectrum schemes are shown in (b) and (d). Ray-optic model are also overlapped on the cross-section of the tube waveguides. (e) THz transmission through uniform tube waveguides. Note that the rays corresponding to different order pulses have the same propagation angles in the air-core.

obtained owing to the fact that most power are still propagating inside the air-core. Experiments verify our finding, which may pave a way for the further development of compact, reliable and flexible THz systems.

5.4.1 Waveguide structure.

Figures 5.13(a) and (b) show the structure of the tube waveguides with uniform cladding. Ray-optic model are also overlapped on the cross-section of the tube waveguides and the rays corresponding to different order pulses have the same propagation angles to the normal of the core-cladding boundary in the air-core. For some certain frequencies, main pulse and echoes are in/out phase ($2m\pi$ / $(m+1)/2\pi$ phase shift), that is anti-resonant/resonant frequencies for the cladding, thus high/low transmission can be observed. Spectrum schemes are shown in 5.13(c) and (d). The scheme of the THz transmission through the uniform tube waveguides in time domain are also shown in fig. 5.13(e).

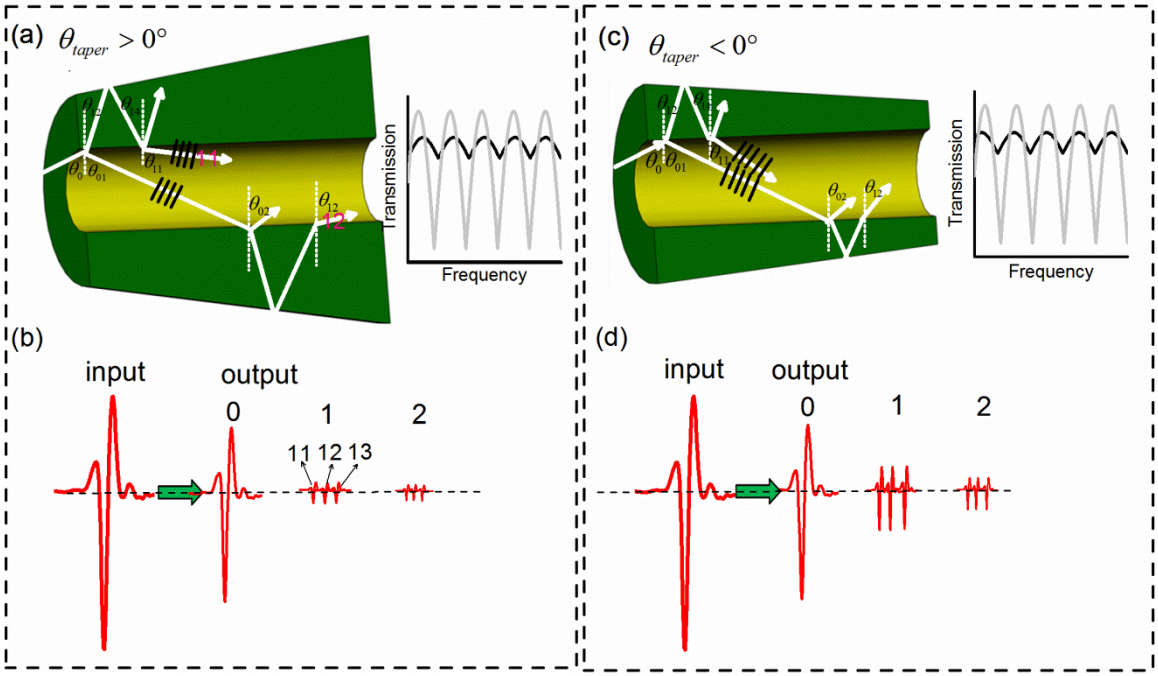

Figure 5.14 Profiles of the taper tube waveguides with (a) positive and (c) negative taper angles. Ray-optic model are also overlapped on the cross-section of the tube waveguides. THz transmission through tube waveguide with (b) positive and (d) negative tapered cladding, respectively. Note here that for the uniform tube waveguide, the rays corresponding to different order pulses have the same propagation angles in the air-core. While for the tube waveguides with positive and negative tapered cladding, the former propagation angles increased until the incident angle (from cladding refract to air-core) is larger than critical angles, and propagation angles in the latter decreased. E.g., $\theta_{11} < \theta_{01}$ for the waveguides in Fig. 5.14(a) and $\theta_{11} < \theta_{01}$ for the waveguides in Fig. 5.14(c), respectively.

Figure 5.14(a) shows the structure of the tube waveguides with tapered cladding. It has an air-core with uniform diameter ID surrounded by a cladding layer with gradually changed thickness t(z), t(z) is a linear function of position z and can be expressed by $t(z) = t(0) + z\tan\theta_{taper}$, where θ_{taper} is the tapered angle, which is calculated by $\theta_{taper} = \frac{t(L) - t(0)}{L}$, L is the length of the tube waveguides, t(0) and t(L) are the input-end and output-end cladding thickness respectively. In order to avoid the large absorption of the cladding layer, one of the lowest polymer (Topas) materials absorption in THz region is selected as cladding layer.

5.4.2 Simulation and principle of the taper tube waveguides.

First, let us look at the effect of the tapered cladding to the tube waveguides transmission. In order to simplify the simulation process, we simulated the transmission loss based on the 1-D slab-type waveguide structure, which is shown in Figs. 5.15(b) and (d). It should be noted that although this structure corresponding to the slab-type taper plates rather than real taper tubes, the effect of tapered cladding can also be observed, thus can used to explain the effect of the tapered cladding to the tube waveguides transmission. Numerical simulations are carried out by using the commercially available FEM solver (COMSOL4.3b). In the simulation, the parameters are set as following: $ID = 4\ \mathrm{mm}$, $t(0) = 3\ \mathrm{mm}$, and $L = 50\ \mathrm{mm}$, while gradually changing the $t(L)$ which result in the tube waveguides with different tapered cladding angles ($\theta_{taper} = \frac{t(L) - t(0)}{L}$). The frequency-dependent losses for the tube waveguides with four selected tapered cladding angles (0.29°, 1.15°, -0.29° and 1.15°) are shown in Fig (2) and also with the loss of uniform tube waveguides $t(0) = t(L) = 3\ \mathrm{mm}$ overlaid. Figs. 2(a) (c) and (b) (d) represent losses of the slab-type waveguides with positive ($\theta_{taper} > 0$) and negative ($\theta_{taper} < 0$) tapered cladding, respectively. both TM (a) (b) and TE (c) (d) modes clearly demonstrate that the overall oscillation amplitude decrease with the increasing absolute tapered cladding angles ($\left|\theta_{taper}\right|$). The oscillation are almost totally suppressed for the waveguides with $t(L) = 4\ \mathrm{mm}$ ($\theta_{taper} = 1.1458°$) or $t(L) = 2\ \mathrm{mm}$ ($\theta_{taper} = -1.1458°$). This indicates that this kind tube waveguides can obtain broad bandwidth with the introduction of just small tapered cladding angles.

In order to understand the physics behind the concept, we explain the uniform tube firstly. Cross section profiles of the uniform tube waveguides are shown in Figs. 5.15(a) and (b). The light propagates with initial angle θ_0, which are calculated based on $\sin\theta_{01} = \mathrm{n}_{\mathrm{eff}} / \mathrm{n}_{\mathrm{core}}$, to the normal of the inner cladding boundary in the air-core, where $\mathrm{n}_{\mathrm{eff}}$ is the effective index of the uniform tube waveguide. Both reflection and transmission occur at inner cladding boundary. The wave corresponding to reflection part continues to propagate inside the core

and that corresponding to refraction part keeps propagation along the cladding and gradually leak to outside and back to the core. Here the propagated light experience no F-P reflection, which means the light always propagated inside the core, is defined as main pulse. The remained are defined as echoes. E.g., Propagated light experience 1 time F-P reflection is defined as 1st order echoes. To this analogizes the propagated light experience n times F-P reflection is defined as echoes order N. Note that for the uniform tube waveguide, the rays corresponding to main pulse and different order echoes have the same propagation angles to the normal of the inner cladding boundary in the air-core. While situation is different for the tube waveguides with positive and negative tapered cladding angles, propagation angles to the normal of the inner cladding boundary in the air-core changed for the rays corresponding to the echoes are not kept the same.

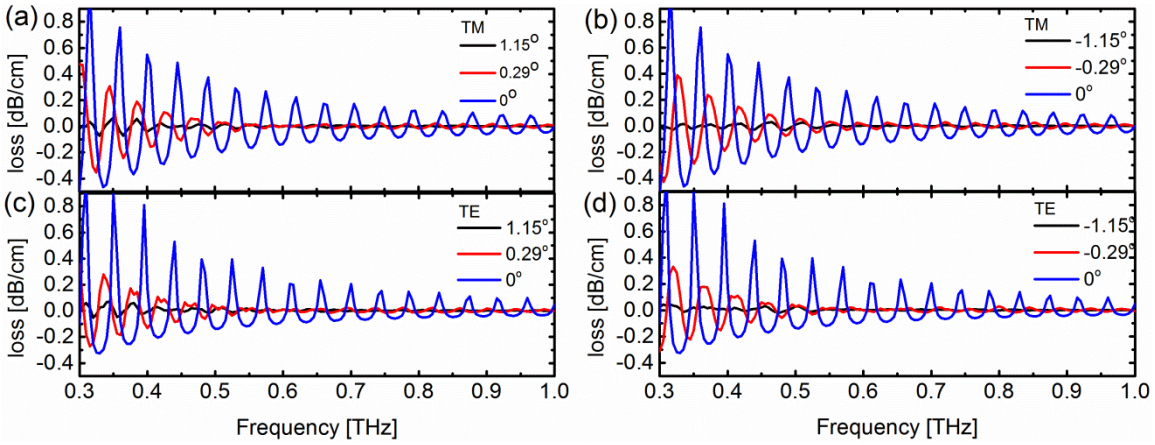

Figure 5.15 Effect of the introduced tapered cladding ($\theta_{taper}=0$, $\theta_{taper}=0.15°$, $\theta_{taper}=0.29°$ for (a) (c) and $\theta_{taper}=0$, $\theta_{taper}=-0.15°$, $\theta_{taper}=-0.29°$ for (b) (d)) on the normalized propagation loss for TM (a)(b) and TM (c)(d), which are calculated as the propagation loss of each tube waveguides subtract that of uniform tube with infinite cladding thickness.

Now, let us try to understand interesting physics behind the concept of tube waveguides with tapered cladding. Cross section profiles of the tube waveguides with positive and negative tapered cladding angles are shown in Figs. 5.15(a) and (c). We explain it by using geometric optics approach, which is similar with F-P model of the uniform tube. Similar with uniform tube waveguides, the tube waveguides with tapered cladding also have main pulse and different order echoes and the incident ray are also defined as $\theta_{01}=\sin^{-1}(n_{eff}/n_{core})$, where n_{eff} is the effective index of the uniform tube waveguides with the same dimension as

the input end. Under such condition, the introduction of tapered cladding has not any effect on the rays corresponding to the main pulse. However, the situation is totally different for echoes, the rays corresponding to different order echoes will propagate along the core with changed angles due to the introduction of the tapered cladding.

As mentioned above, the main pulse experiences no change with the introduction of the tapered cladding. Here we mainly investigate the tapered cladding on echoes. The propagated rays refract through the cladding and hit the outer cladding boundary, and then hit the cladding-core boundary. According to the traditional Fresnel laws, the incident angle θ_{14} at this boundary becomes $\theta_{14}^{0}+2\theta_{taper}$ (θ_{14}^{0} is the incident angle for the uniform tube waveguides), then the refraction part of the light come back to the core and becomes the 1st order echoes. Rays corresponding to 1st order echoes in the air-core, which experience 1 time F-P reflection, propagate in the core with the angle of to the normal of the core-cladding boundary. $\theta_{11}=\sin^{-1}(n_{clad}\sin(\theta_4+2\theta_{taper}))$. Similarly, rays corresponding to echoes order of N, which experience N times F-P reflection, the propagated angles to the normal of the core-cladding boundary become $\theta_{N1}=\sin^{-1}(n_{clad}\sin(\theta_4+2N\theta_{taper}))$.

Here we divide the situations into two cases, the tube waveguides with positive ($\theta_{taper}>0$) and negative ($\theta_{taper}<0$) tapered cladding, respectively. The incident angle at cladding-core boundary from cladding to core corresponding to order echoes N become $\theta_4+2N\theta_{taper}$.

For the former case, the incident angle at cladding-core boundary from cladding to core becomes larger for higher order echoes. Consequently, we can predict that it will experience total reflection if $\theta_4+2N\theta_{taper}$ is larger than the critical angle ($\theta_4+2N\theta_{taper}>\sin^{-1}(n_{core}/n_{clad})$) at cladding-core boundary, total reflection occur and result in suppressed echoes. Extremely case is that if the tapered cladding angles is large enough and satisfies $\theta_4+2\theta_{taper}>\sin^{-1}(n_{core}/n_{clad})$, thus only main pulse propagates in the waveguides air-core.

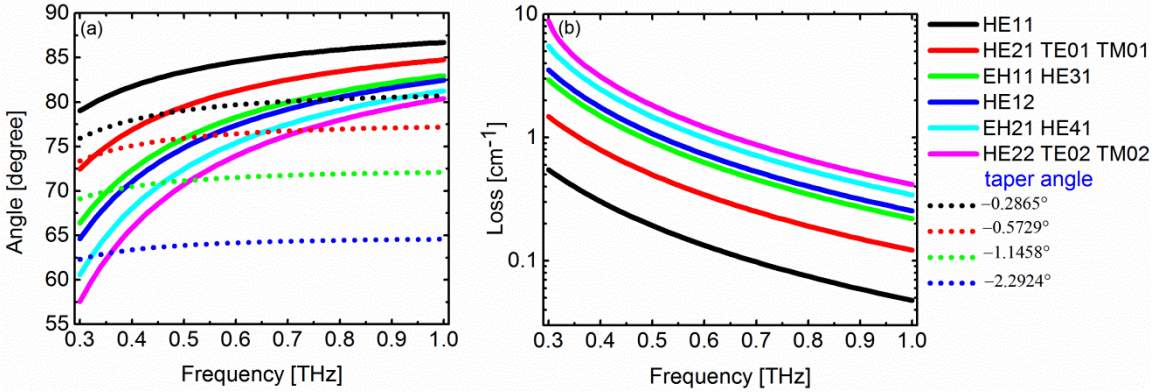

Figure 5.16 propagation (a) angles to the normal core-cladding boundary and (b) losses corresponding to different modes of infinite cladding tube waveguides. Dot lines in (a) represent the calculated propagation angles to the normal core-cladding boundary corresponding to 1st order echoes.

For the latter case, the incident angle at cladding-core boundary from cladding to core becomes smaller for higher order echoes and thus smaller propagation angles in the air-core. Figs. 5.16(a) and (b) show the propagation angles in the air-core and losses corresponding to different modes, which are calculated based on $\sin\theta_{01} = \mathrm{n}_{\mathrm{eff}}(m)/\mathrm{n}_{\mathrm{core}}$, where m are related to different modes. It shows that the higher the mode order, the smaller the propagation angles to the normal core-cladding boundary. In Fig. 5.16(a), the propagation angles corresponding to 1st order echoes are also calculated based on shell laws and represented as dot lines, indicating that the propagation angles in the air-core become smaller as the tube waveguides with larger taper angles. Note that small tapered cladding angles can lead to generally large change of the propagation angles normal to the core-cladding boundary corresponding to echoes. E.g., the introduced cladding with tapered angle of 0.29°, the propagation angles change corresponding to 1st order echoes are generally larger than $5°$, which can be seen from the comparison between the black dot and solid line curves in Fig. 5.16(a). The black dot line curve are far away from the fundamental mode curve and more nearby high order modes curve, which probably means large part of this ray will be converted to high order modes. The larger the tapered cladding angles (dot lines in Fig. 5.16(a)), the more far away to fundamental mode curve and more nearby the higher order modes, which means fewer part of 1st order echoes will be converted to fundamental mode and larger part of this ray will be converted to higher order modes, thus less and less signal will remain due to the fact that larger attenuation for the higher order

modes. Such phenomenon is more obvious for higher order echoes. Therefore, for the tube waveguides with larger taper angles, the less echoes signal will remain. Moreover, different from the uniform tube waveguides (each order echoes are the sum of pulses experience the same time F-P reflection due to all these pulses have the same phase), there has some phase difference for these pulses related to each same order echoes for the tube waveguides with tapered cladding, which result in weakening echoes signal. These two factors weaken the interference and will contribute to the broadband transmission for such kind of tube waveguides.

5.4.3 Experiment of taper tube waveguides.

In order to experimentally demonstrate the effect of the introduction of tapered cladding into tube waveguides, we deliberately design several different tube waveguides. They have the same air-core diameter $ID = 4\ \mathrm{mm}$ and input cladding thickness $t(0) = 3\ \mathrm{mm}$ but several different output-end cladding thickness ($t(L) = 5\ \mathrm{mm},\ 4\ \mathrm{mm},\ 3.5\ \mathrm{mm},\ 3.25\ \mathrm{mm},\ 3\ \mathrm{mm},\ 2.75\ \mathrm{mm},\ 2.5\ \mathrm{mm},\ 2\ \mathrm{mm},\ 1\ \mathrm{mm}$), the cladding thickness is linear changed along the tube length direction and thus corresponding to different tapered cladding angles. The length of all tube waveguides are chosen $L = 50\ \mathrm{mm}$.

We perform transmission measurements via THz-TDS. Figs. 5.17(a) and (b) present the time scans of the guided THz pulses for aforesaid tube waveguides. There exists only one main pulse for reference tube (not shown here). Here we divide the taper tube waveguide into two groups (positive [$\theta_{taper} > 0$] and negative [$\theta_{taper} < 0$] tapered cladding angles) shown in Figs. 5.17(a) and (b) respectively. For each measured tube waveguides, there exist several echoes beside main pulse. Since the signal related to the echoes is small especially for the tube waveguides with large absolute taper angles ($\left|\theta_{taper}\right|$), some of these echoes are difficult to be distinguished from the system signals. In order to see the results more clearly, we also measured thick tube with the same dimension as reference tube and then overlaid with each measured tube results for comparison. Note that there have no echoes for this thick tube waveguide, so the signals except main pulse can be seen as system signal. For the main pulse of all measured tube waveguides, all of them are completely overlap with each other, which

can be seen from Figs. 5.17(a) and (c). This is because the wave corresponding to main pulse experience no F-P reflection, which means there has no influence by the outside cladding-air interface and the results are only related to the air-core diameter and cladding index (the same for all waveguides). The echoes, which are determined from the difference between the signals of tapered tube waveguides and the thick tube waveguides, are noted by dashed circle. Results show that the echoes become smaller as the absolute taper cladding angle ($\left|\theta_{taper}\right|$) increase. For the

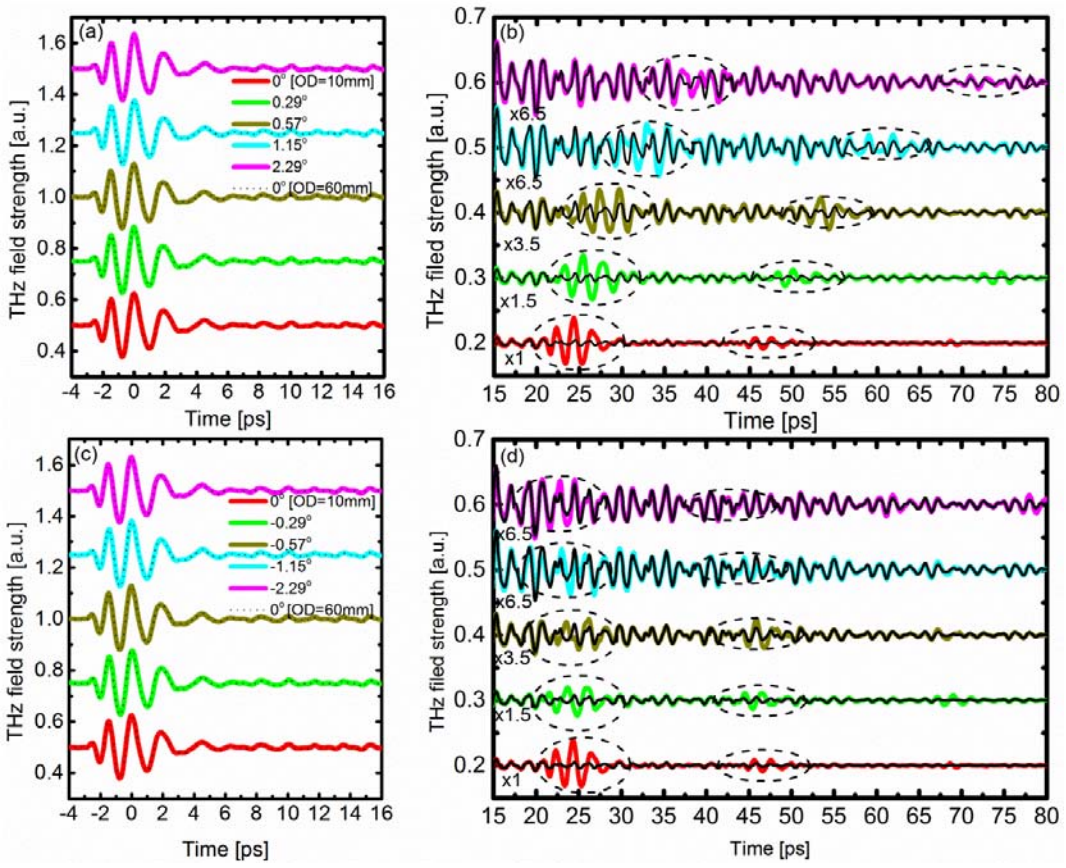

Figure 5.17 Measured time-domain THz signals of 5 cm tube waveguides with the same air-core diameter [ID=4 mm] and input-end cladding thickness ($OD_2 = 3\ \mathrm{mm}$) but with different output-end cladding thickness ($OD_2 = 5\ \mathrm{mm},\ 4\ \mathrm{mm},\ 3.5\ \mathrm{mm},\ 3.25\ \mathrm{mm},\ 3\ \mathrm{mm},\ 2.75\ \mathrm{mm},\ 2.5\ \mathrm{mm},\ 2\ \mathrm{mm},\ 1\ \mathrm{mm}$), which result in different taper angles. Main pulse and echoes corresponding to the tube waveguides with positive (a) (b) and negative (c) (d) tapered cladding angles are separately shown, Echoes signal are magnified for easy observation. In order to see the results more clearly, measured results of thick tube ($OD_1 = OD_2 = 60\ \mathrm{mm}$) are also overlaid with each measured tube results for comparison.

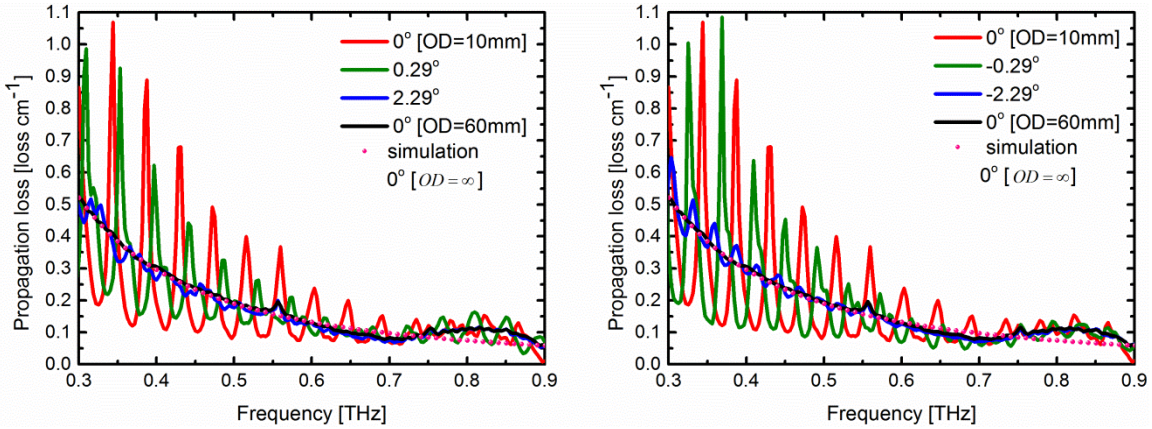

Figure 5.18 Measured propagation loss for the tube waveguides with (a) positive and (b) negative tapered cladding angles corresponding to time domain signal in Fig. 4.

tube waveguides with positive/negative tapered angles ($\theta_{taper} > 0$), the time delay between adjacent order echoes (e.g., 1st order echoes and the main pulse) become longer/shorter. Such behavior can be attributed to the different transmitted path difference between the adjacent order pulses. As predicted, the echoes can be almost totally suppressed with the introduction of general small cladding tapered angle. It can be seen from Fig. 5.17 that all of these echoes are almost disappear when the absolute tapered angle is larger than 1.15^{o}.

The propagation loss of the selected tube waveguides, in which positive and negative tapered angles, are shown in Figs. 5.18(a) and (b), respectively. The propagation loss curve of the thick uniform tube waveguide ($\mathrm{ID} = 4$ mm and $\mathrm{t}(0) = \mathrm{t}(\mathrm{L}) = 28$ mm) are also overlaid and there has no oscillation as only main pulse exist in the time domain signal. As predicted, the overall amplitude oscillations of the tapered tube waveguides become generally smaller with the increasing absolute taper angle ($|\theta_{taper}|$) due to the less echoes shown in time domain signal. They oscillate around the propagation loss of thick tube waveguide. Simulated loss, based on FEM solver (red dot), of the tube waveguides with infinite cladding are also overlaid on the experiment loss. Within the frequency range from 0.3 to 0.8 THz, near-perfect agreement between experiment and simulation is achieved. deviation at large frequencies maybe caused by the bad coupling from the reference tube to measured tubes at large frequencies, at which are more sensitive to alignment between the reference tube and measured tubes.

5.5 Summary

We at first have numerically and experimentally demonstrated a tube waveguide, which guides THz pulses with low loss (0.05-0.2 dB/cm) and low dispersion ($|\beta_2| < 10$ ps/THz/cm) in the 0.3-1 THz range, with a bandwidth much larger than a classical ARROW waveguide. The smooth transmission profile and the associated low dispersion is obtained by deliberately introducing material loss to the cladding material, thus efficiently removing the interfering fields that bounce through the cladding and back into the core in a traditional low-loss ARROW tube waveguide. The absorptive cladding is also effective for reducing the bend loss of the fiber, which remains below 0.2 cm^{-1} for s-polarized light even for tight bending radii down to 10 cm. We have also demonstrate that adding a thin layer of a suitable absorber, here exemplified with water, the dispersion can be even further reduced ($|\beta_2| < 1$ ps/THz/cm in the 0.3-1 THz range) for fundamental hybrid mode, without increasing the overall loss. We detailed investigate the physics mechanism of the loss curve oscillation for the tube waveguide with water jacket. Finally, we have investigate another kind of tube waveguides consist of a uniform air-core and a cladding layer with tapered thickness are designed and demonstrated. Results show that the same effect of the highly absorbing cladding material tube waveguides can also be obtained, thus breaking the cladding material limitation. The proposed waveguides are with the attractive broadband optical properties in the low THz range, where future communication systems will operate, makes this new twist on the classical tube waveguide very attractive.

6 Mechanically down-doped terahertz fiber directional couplers

6.1 Introduction

As the progress in THz fibers and waveguides, it has now become possible to develop THz devices, such as fiber Bragg gratings (FBGs) [79, 80, 142], filters [79, 142], couplers [66, 73, 87, 115, 143, 144], and polarization splitters [65, 144]. Here, we focus on the investigation of THz directional couplers, which have been reported based on dielectric sub-wavelength fibers [73, 87] and pipes [115, 143]. The directional coupler based on sub-wavelength fibers was achieved by placing two sub-wavelength rods in close proximity. Since most of the power is localized outside of the rods, a short coupling length and low loss can then be achieved. However, sub-wavelength couplers are very susceptible to external disturbances, which make them unpractical in many applications. In [115], a pipe waveguide-based directional coupler was achieved by placing two identical square pipe waveguides close to each other and using the mechanism of anti-resonant reflecting optical waveguiding (ARROW) [145]. The proposed directional coupler was shown to work efficiently with low loss by choosing a proper cladding thickness of the pipe waveguides. However, pipe-based couplers usually require large core dimensions to achieve low loss, which makes these waveguides highly multi-moded. Both the sub-wavelength and pipe directional couplers have in common that they only have a constant coupling length over a narrow bandwidth.

In the optical regime, dual-core PCFs have been studied extensively due to their inherent design flexibility. Several PCF dual-core couplers have already been reported over the past years [146-150]. Normally, the dual-core coupler is strongly wavelength dependent, because the coupling strength increases monotonously with the wavelength, which means that the bandwidth is very limited.

For removing the bandwidth limitation, a dual-core coupler with chemical down-doped (e.g., fluorine-doping) cores has been proposed [146], based on an idea put forward earlier in [151], where they demonstrated experimentally that a PCF with a down-doped core has a guided mode whose mode field area initially contracts with decreasing wavelength but at a certain threshold begins to expand again until a short-wavelength cut-off for mode guidance is reached. The reason for this behavior is that the effective index of the PCF cladding tends

toward the index of the pure background material at short-wavelengths. Therefore, at a certain threshold wavelength, the effective cladding index exceeds the index of the down-doped core, which then ceases to support a guided mode [151]. For directional fiber couplers with down-doped cores the existence of a minimum in the mode field area means that the coupling length will show a maximum at some wavelength, at which the coupler will be unusually broadbanded because of the vanishing first derivative of the coupling length [146]. However, most materials have high loss in the THz region and chemical down-doping is complicated, which means that it is not advisable to directly scale this kind of design of directional couplers from the optical region into the THz region.

In this chapter, we investigate a novel kind of broadband THz directional coupler that uses mechanical down-doping (or air down-doping) instead of chemical down-doping (fluorine doping) in the two cores. The air down-doping is using a triangular array of air holes, which can be easily achieved by drill-and-draw technology [63]. Due to the air-hole structure in both the cladding and the down-doped core this type of coupler has considerable design freedom in a huge parameter space, we also present a thorough numerical design optimization of the structure parameters (diameter and pitch of the cladding and core air-hole structures) using a figure of merit (FOM) proposed in [66], which takes both the 3-dB bandwidth and device loss into account. We use simple scaling arguments to extend the regime of considered parameters. Our simulations show that at 1THz a structure with suitable parameters can have a large bandwidth of 0.25 THz and relative low device loss of 9.2dB. Moreover, we verify that the optimum coupler is single-moded and we investigate the robustness of its performance to structural changes.

6.2 The Coupler structure description

Figure 6.1(a) shows the cross section of the proposed air-doped dual-core coupler, where Λ and d are the pitch and hole diameter in the cladding, respectively. The purple regions represent air-doped cores with a triangular array of air-holes with a pitch Λ_c and hole diameter d_c. D_c is the effective core diameter and the center-to-center distance between the

two cores is two pitches. An enlarged view of the doped-core is shown in the left top of Fig. 6.1(a). The coupler is considered to be made of TOPAS.

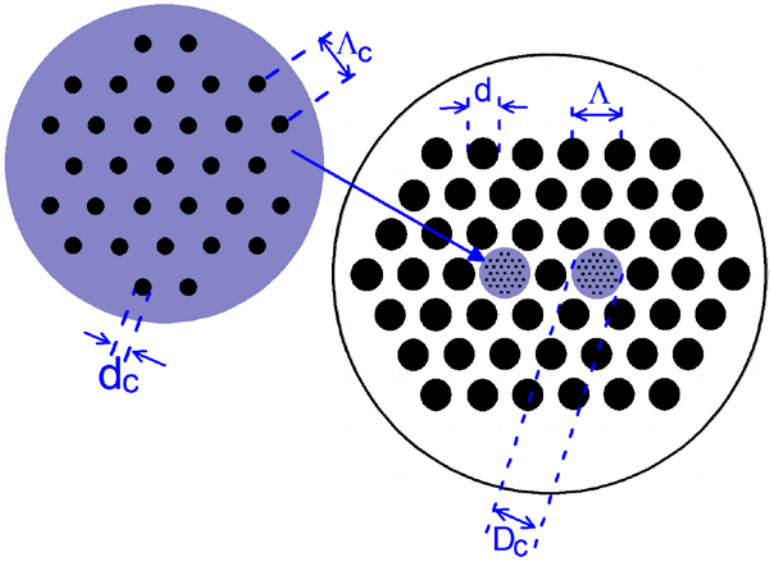

Figure 6.1 Cross section of the air-doped dual-core coupler. Dark regions represent air and purple regions represent air-doped cores. Λ, d and Λ_c, d_c represent the pitch and hole diameter of the cladding and two cores, respectively. D_c is the effective core diameter.

6.3 Coupling characteristic

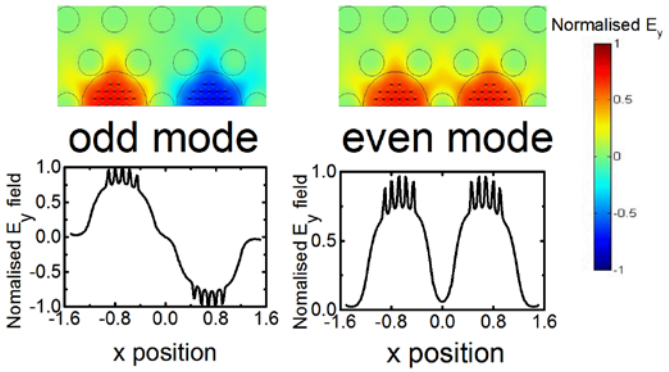

Figure 6.2 Electric field profiles at 0.9 THz (y polarization) of even and odd super-modes in the x-y plane (top two figures) and along the x axis with y=0 (bottom two figures).

The coupler can support two fundamental super-modes, an even mode and an odd mode. Their electrical field profiles (y polarization) are shown in Fig. 6.2. From Fig. 6.2, it can be seen that an enhancement of the electric field appears inside the sub-wavelength air holes of the two cores, which is due to the boundary conditions in the electric flux density. More specifically, According to

the boundary condition, for the electrical field with y-polarization, the electrical field should be continuous along the x-axis while the electrical displacement should be continuous along the y-axis. Thus the terms that are continuous in the air-topas boundary should be E_y (y-component of electrical field) and D_x (x component of electric flux density). However, since the holes are very small and the E_y discontinuity along the y axis extends to the center of the sub-wavelength hole and the well-known phenomenon of field enhancement in sub-wavelength holes is observed [81, 84, 86, 87]. To further verify this explanation, electrical filed profiles at two polarizations for even and odd super-modes in the x-y plane are provided in Fig.6.3.

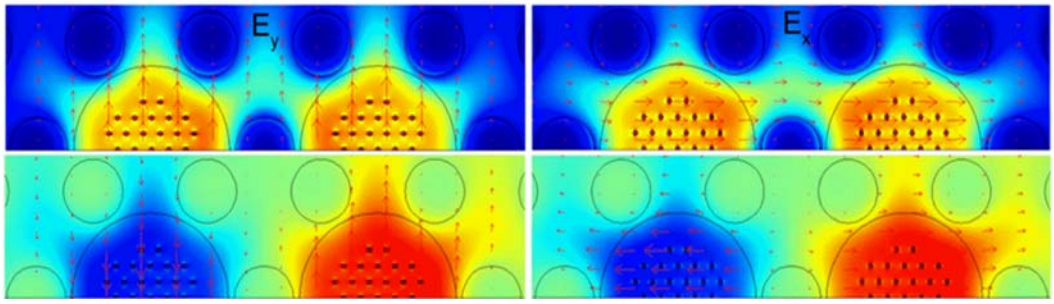

Figure 6.3. Electrical filed profiles (two polarizations) for even and odd super-modes in the x-y plane.

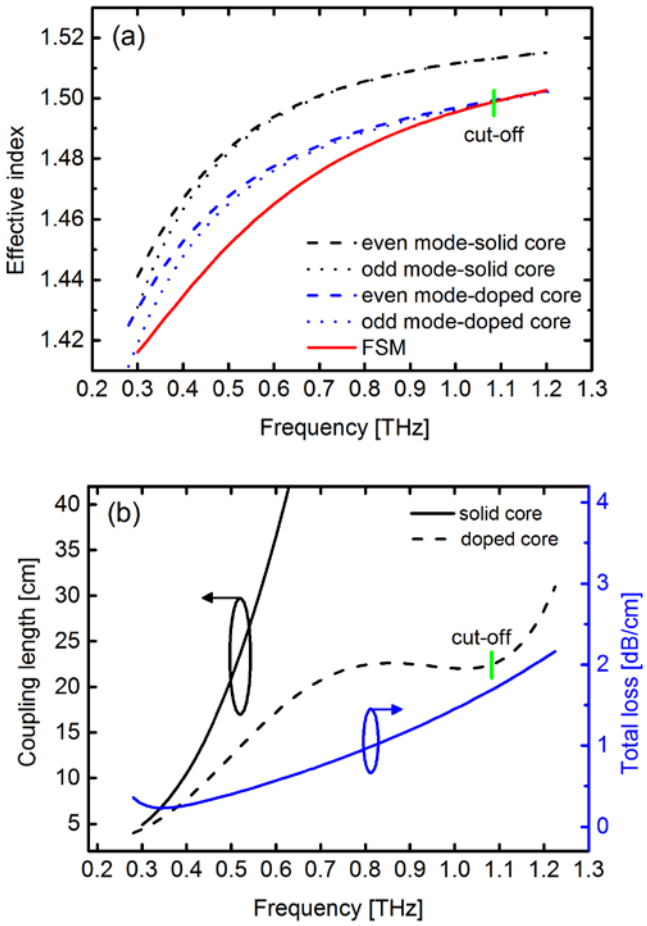

Figure 6.4 Effective index of the even and odd modes versus frequency for the air-doped coupler (Λ=682.5 µm, d/Λ=0.52, Λ_c=102.375 µm, d_c/Λ_c=0.25) and un-doped solid-core coupler (Λ=682.5 µm, d/Λ=0.52). Solid red curve is the calculated FSM. Green short vertical solid line represent the cross point between the odd mode and cladding mode of the air-doped coupler, corresponding to the fundamental-mode cut-off frequency. (b) Coupling lengths of the air-doped (black dashed line) and un-doped solid-core (black solid line) coupler versus frequency. Blue solid curve represents the frequency dependent total loss of the air-doped coupler.

Figure 6.4 (a) shows the calculated frequency-dependent effective index of the even and odd super-modes of the air-doped (blue dashed and dotted curves) and solid-core (black dashed and dotted curves) coupler, respectively. Red solid curve is the fundamental space-filling mode (FSM) calculated using the unit cell approach [152]. Fig. 6.4 (a) shows that the index of even supermodes is always slightly higher than that of the odd supermodes. The effective index of the guided modes is reduced due to the air-doping in the two cores. The predicted cut-off frequency for the air-doped coupler is clearly observed, located at the crossing of the odd supermodes and FSM curve (short vertical green line).

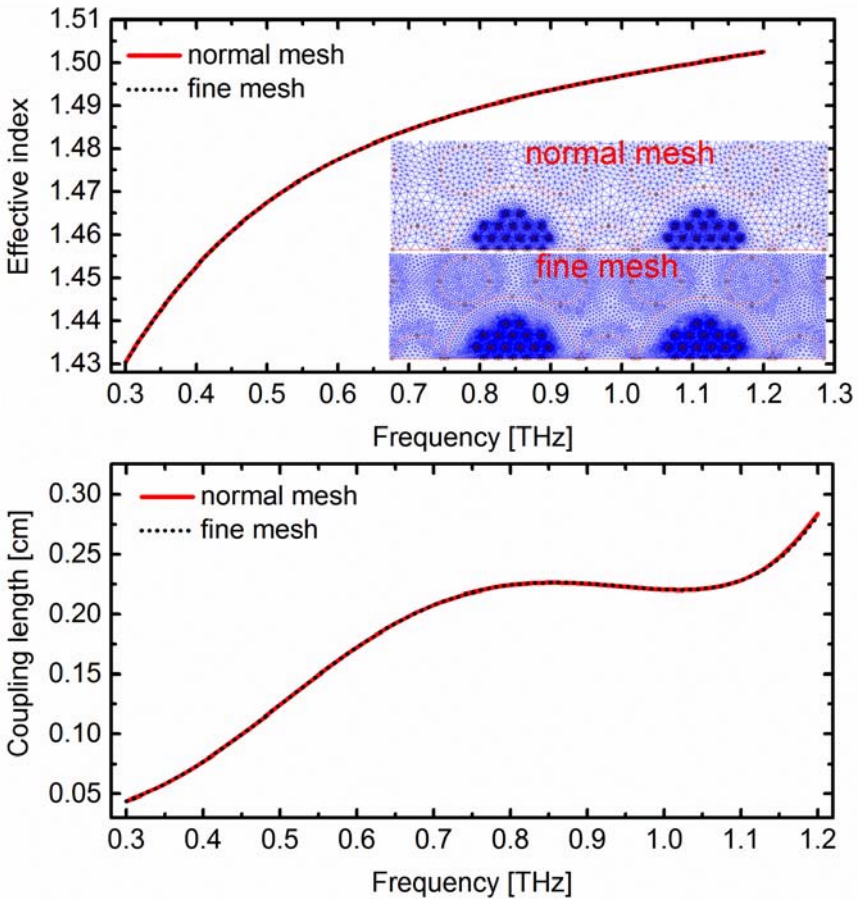

Figure 6.5. Comparison between the air-doped coupler (Λ=682.5 μm, d/Λ=0.52, Λ_c=102.375 μm, d_c/Λ_c=0.25) based on normal mesh (36593 elements) and fine mesh (137636 elements).

In Fig.6.4 we show the coupling length L_C of the undoped (solid-core) and air-doped coupler versus frequency. The coupling length of the solid-core coupler is seen to increase monotonically with frequency, which is due to the monotonically decreasing mode-field diameter. In contrast, it is seen that by down-doping the cores, the L_C-curve becomes non-monotonic and a flat coupling length can be obtained over a broad bandwidth. The propagation loss α, defined as the material absorption loss multiplied by the percentage of the mode field in the background material plus the confinement loss, is also shown as in Fig. 6.4 (b) (blue curve). The total loss is necessary to take into account in the design of any THz waveguide device and we see it monotonically increases with increasing frequency, except close to the low frequency edge, where confinement losses dominate. Since the confinement loss and field distribution are different for even and odd modes, we use the average loss of even and odd modes for all simulations in this paper. Mesh quality is checked by repeating the calculations with a finer mesh. We compared typical results for the

effective index and coupling length found with the 36593 element mesh with the results found with a finer 137636 element mesh. As can be seen in Fig. 6.5 the results are nearly identical, which means that the mesh is good enough. However, the number of elements and the element size varies with the coupler parameters, which is why we don't provide actual mesh data in the paper. We note that this is absolutely standard in the literature using the commercial COMSOL tool.

6.4 Optimization of the 3-dB coupler

In order to realize a 3-dB coupler with the best trade-off of both bandwidth (B) and total device loss (αL_D), we define the FOM=B/(αL_D), measured in THz. Here the bandwidth B is defined as the frequency range over which the coupling length is the same within ±1% and $L_D=L_C/2$ is the device length, which is half the coupling length, because we consider a 3-dB coupler.

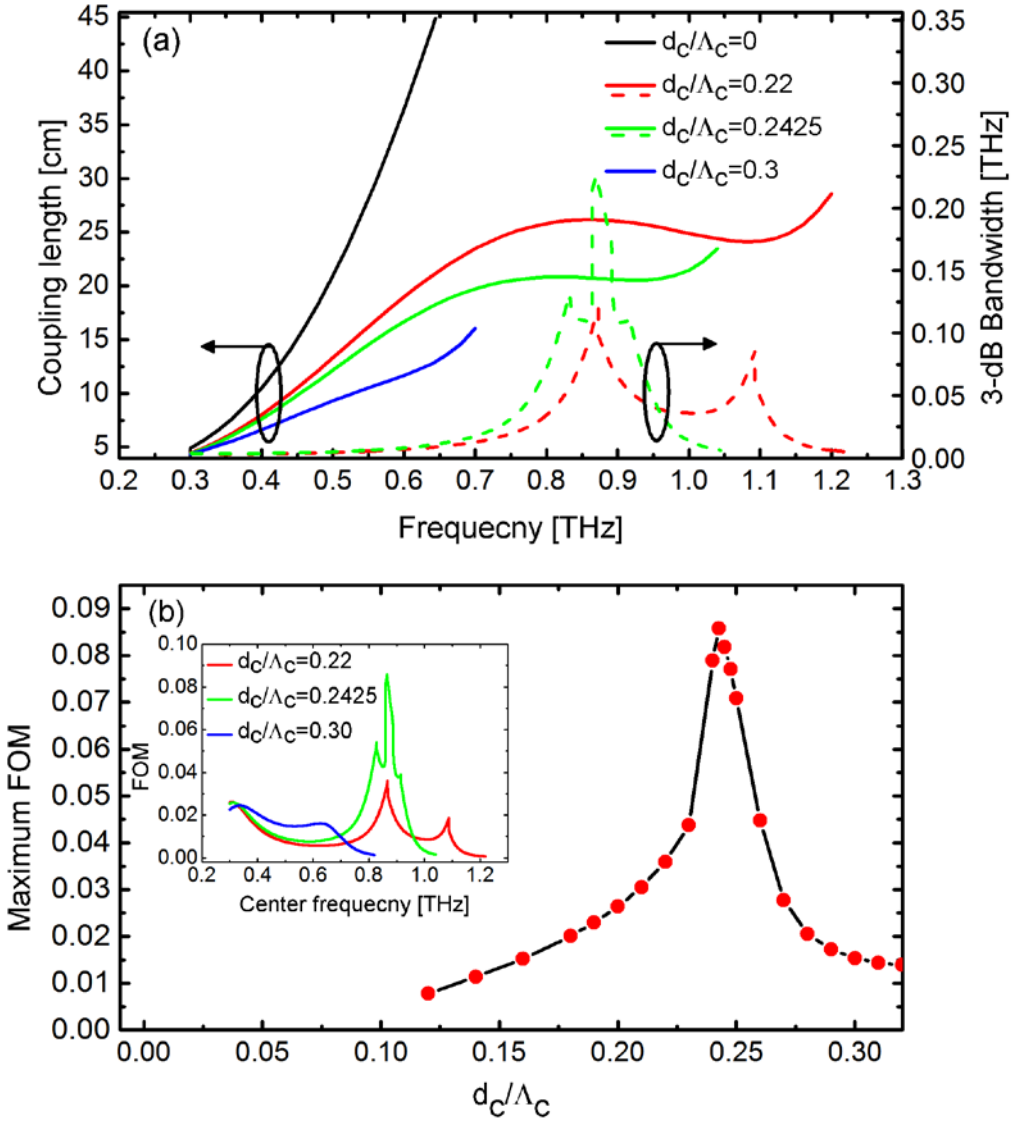

Figure 6.6 (a) Coupling length versus frequency for fixed d/Λ=0.52, Λ=682.5 μm, and Λ_c=112.875 μm and varying degree of down-doping d_c/Λ_c. Red and green dashed lines represent the 3-dB bandwidth of the coupler with d_c/Λ_c=0.22 and 0.2425, respectively. (b) Maximum FOM as a function of d_c/Λ_c (only cases with B>0.01 THz are plotted). Inset is FOM versus frequency for the different d_c/Λ_c.

We initially optimize the structure by changing only the core hole diameter d_c, while keeping Λ_c=112.875 μm, d/Λ=0.52, and Λ=682.5 μm fixed. This allows us to focus on the effect of down-doping. In Fig. 6.6(a) we show the coupling length versus frequency of the un-doped coupler (d_c/Λ_c=0) and the down-doped coupler for 3 values of d_c/Λ_c, i.e., 3 degrees of down-doping. We see that the more the core is down-doped the smaller the coupling length becomes and the lower the cut-off frequency becomes (sharp rise at high frequencies). It is

also evident that a region with a flat coupling length will exist for a certain optimum value of d_c/Λ_c, i.e., a certain degree of down-doping.

The frequency-dependent FOM is shown in the inset of Fig. 6.6(b), displaying local maxima related to the extrema of the L_C-curve. In Fig. 6.6(b) we track the maximum FOM versus d_c/Λ_c, with a resolution of 0.0025, from which we can determine the maximum FOM = 0.086 THz to be at d_c/Λ_c =0.2425. Only couplers with a bandwidth larger than 0.01 THz were tracked.

We now turn to optimize also the cladding hole diameter d, while keeping the two pitches fixed at Λ_c=112.875 µm and Λ=682.5 µm. For each value of d/Λ we find the optimum degree of down-doping d_c/Λ_c with a resolution of 0.0025 as in Fig. 6.6(a) shows the frequency profile of the FOM at optimum down-doping d_c/Λ_c, for selected values of d/Λ. Given the underlying optimization the profile now looks more complicated, but a maximum can be identified. The maximum is tracked in Fig. 6.7(b), from which we see that the optimum value FOM = 0.105 THz occurs at a relative cladding hole diameter of d/Λ=0.65. From Fig. 6.7(b-c) we see that the bandwidth at optimum d_c/Λ_c is in fact not maximum at d/Λ=0.65, the optimum is obtained due to a low device loss because of a simultaneous low center frequency and device length.

The coupler performance is summarized in Fig. 6.8(a-b) versus d/Λ and d_c/Λ_c for fixed pitched Λ = 682.5 µm and Λ_c = 112.875 µm, which can be used as useful design guides. The difference in optimizing for bandwidth only and taking the loss into account through the FOM is evident. From Fig. 6.8(a) we see that the ±1% bandwidth has the optimum value B=0.349 THz at a very low level of down-doping d_c/Λ_c =0.15 and a small relative hole diameter of the cladding d/Λ=0.44, where the two cores in isolation would be endlessly single-moded. One thing to note is that the ±5% bandwidth of this optimum bandwidth coupler would be 0.822 THz, which is significantly higher than the non-optimized 0.6 THz found in xx. However, the white loss contour lines show that the maximum bandwidth coupler has a high center frequency of 1.1 THz and very high device loss of about 25dB, as was also found in [66] when only optimizing for maximum bandwidth.

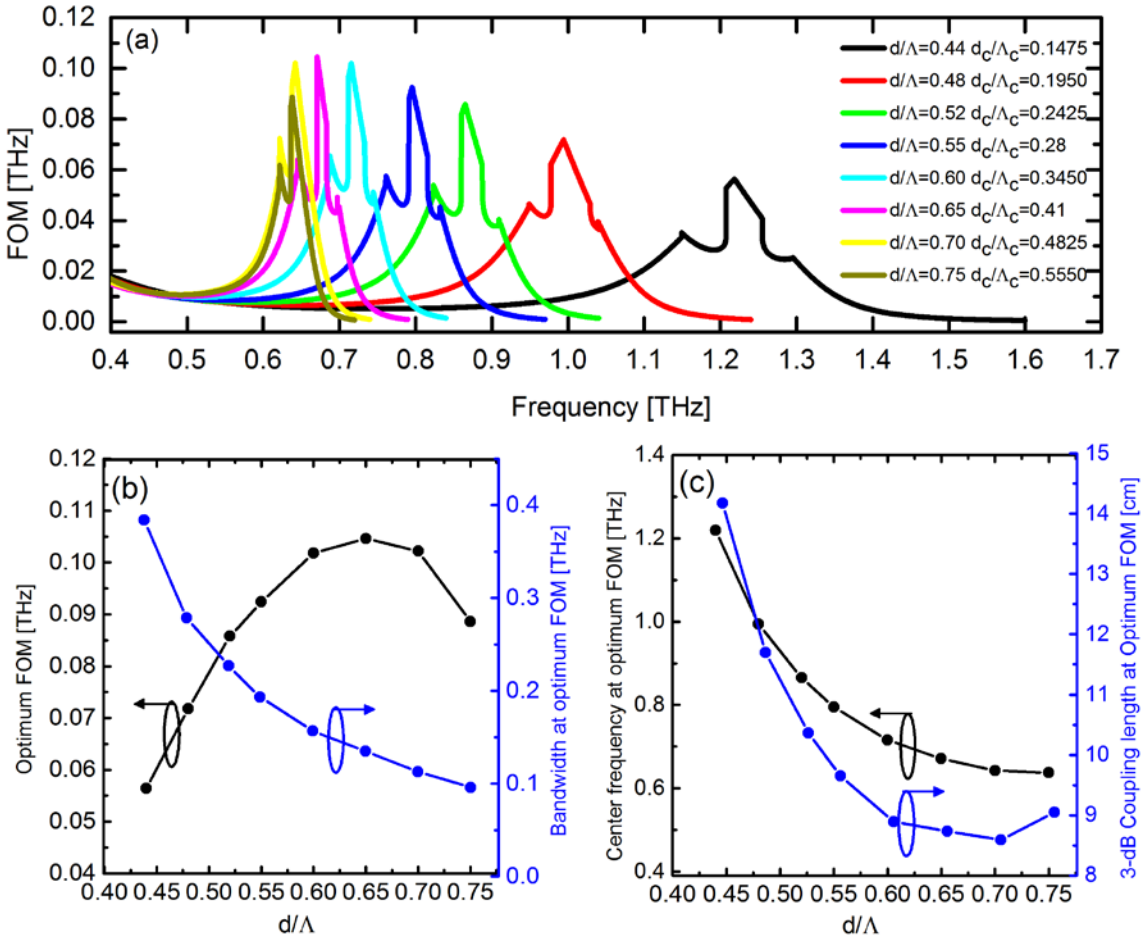

Figure 6.7. Characteristics of the coupler with optimum down-doping d_c/Λ_c (found with resolution 0.0025 as in Fig. 3) for fixed Λ_c=112.875 µm and Λ=682.5 µm. (a) Frequency profile of the FOM at optimum d_c/Λ_c, for selected values of d/Λ (b) Maximum FOM and bandwidth B at optimum d_c/Λ_c (c) Center frequency and 3-dB coupling length at optimum d_c/Λ_c.

In contrast, Fig. 6.8(b) shows that the optimum FOM coupler with FOM=0.1059 THz has a reduced bandwidth of 0.1365 THz and center frequency of 0.67 THz, in exchange for a much reduced device loss of only 5.6 dB. The optimum FOM coupler is seen to require a much higher level of down-doping d_c/Λ_c=0.41 and higher relative hole diameter of the cladding d/Λ=0.65, which means that the two cores in isolation would be multi-moded. However, as we will show later, the optimum FOM coupler is still single-moded.

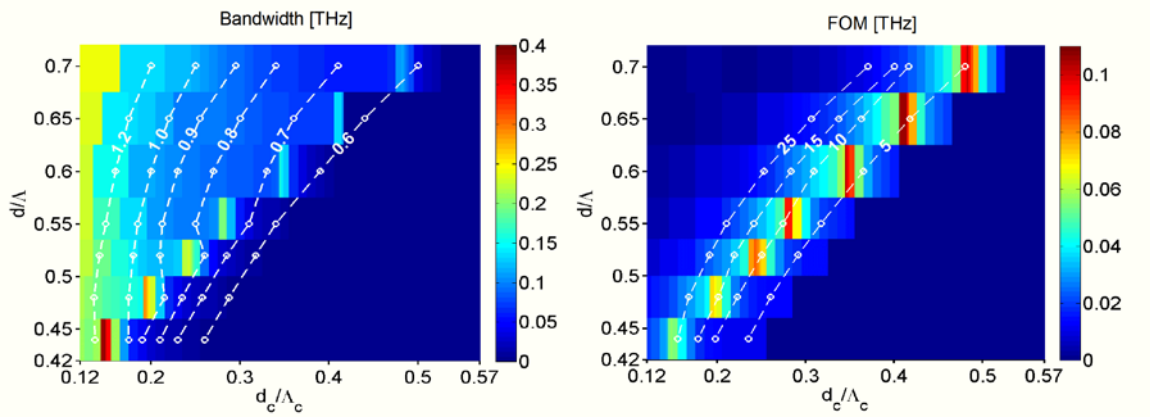

Figure 6.8 (a) Maximum Bandwidth and (b) Maximum FOM (B>0.01 THz) of the coupler with different values of d/Λ (Λ = 682.5 μm) as a function of d_c/Λ_c (Λ_c = 112.875 μm). Six white dashed lines in (a) are center frequency at 1.2, 1.0, 0.9, 0.8, 0.7 and 0.6 THz respectively. Four white dashed lines in (b) are device loss of 3-dB coupler at 25, 15, 10, 5 dB, respectively.

Next step is to investigate the relation between Λ_c and coupler performance. We keep only Λ=682.5 μm fixed and optimize the hole diameters (d and d_c) as in Fig.6.7, but now for five different values of Λ_c. From the results in Fig. 6.9 we see the qualitative same picture as in Fig. 6.7(b), with a clear global maximum in the FOM around d/Λ=0.65, at which the 3-dB bandwidth is not the largest, but the device loss (average attenuation of even and odd modes at a center frequency multiply the 3-dB coupling length) is close to a minimum. The coupler with Λ_c = 102.375 μm (red line) has the highest FOM=0.1094 THz due to a small device loss of 7.3 dB and a bandwidth of 0.183 THz. The value of d_c is 44.53 μm, giving a level of down-doping of d_c/Λ_c =0.4350.

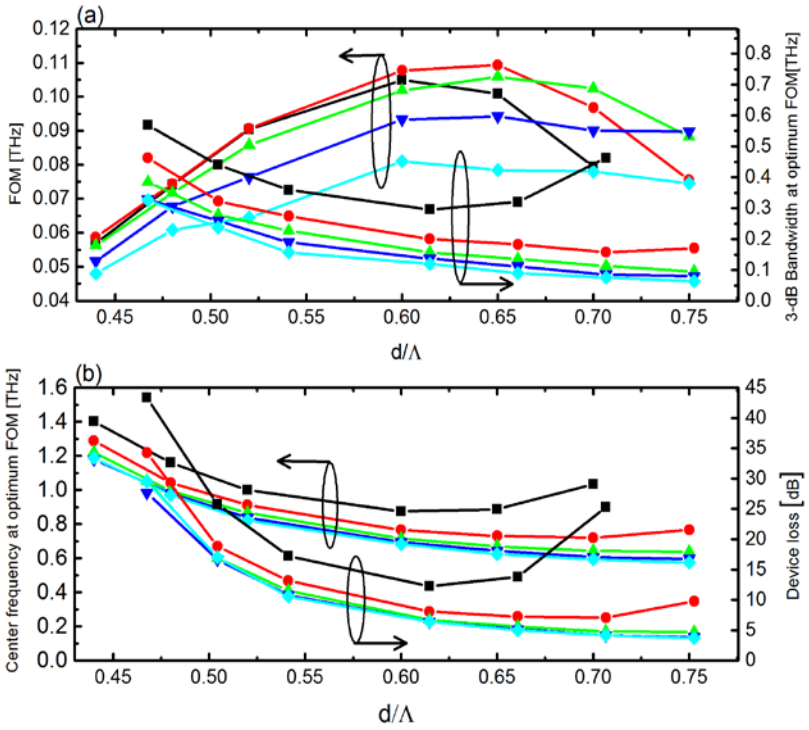

Figure 6.9. Characteristics of the coupler with optimum down-doping d_c/Λ_c (found with resolution 0.0025 as in Fig. 3) versus relative cladding hole diameter d/Λ for fixed Λ=682.5 µm. (a) Optimum FOM and 3-dB bandwidth at optimum FOM, and (b) Center frequency and device loss at optimum FOM for Λ_c =91.875 µm (black lines), 102.375 µm (red lines), 112.875 µm (green lines), 123.375 µm (dark blue lines) and 133.875 µm (light blue lines).

6.5 Scaling of the optimum coupler

To extend the optimization to include all 4 design parameters we use that the material dispersion of TOPAS is very weak in the considered frequency range 0.2-2 THz, the refractive index being approximately equal to 1.5235. We can therefore to a good approximation neglect material dispersion, which allows us to use the inherent scaling properties of the vectorial Helmholtz equation describing the modal properties of the fiber.

We introduce the spatial scaling parameter m, so that the new scaled spatial coordinates (denoted by prime) are $(x',y') = m(x,y)$. The scaled design parameters and device length will then increase with m as $(d',\Lambda',d_c',\Lambda_c') = m\cdot(d,\Lambda,d_c,\Lambda_c)$, and $L_D'=m\cdot L_D$, respectively. This means that the ratios d/Λ and d_c/Λ_c will not change during such a scaling, whereas the new bandwidth and center frequency will decrease with m as $(B',f')=(B,f)/m$.

The scaled FOM can now be found to be $FOM'=B'/(\alpha' L_D')=B/(m^2\alpha' L_D)$, which we can write as $FOM'=FOM\cdot[\alpha/(m^2\alpha')]$. To determine exactly how the FOM changes with the scaling parameter we therefore need to evaluate how the propagation loss α varies with m. As described above the propagation loss is given by $\alpha(f) = p_{MAT}(f)\alpha_{TOPAS}(f)+\alpha_{CONF}(f)$, where the confinement loss, $\alpha_{CONF}(f)$, the fraction of power located in the material, $p_{MAT}(f)$, and the material loss of TOPAS, $\alpha_{TOPAS}(f)$, are all frequency dependent. Here it is important that both the power distribution and the confinement loss are unchanged under the scaling when evaluated at the scaled center frequency, i.e., $p'_{MAT}(f')=p_{MAT}(f)$ and $\alpha'_{CONF}(f')=\alpha_{CONF}(f)$. The change in the propagation loss under the scaling is then solely because the TOPAS material loss must be evaluated at the new scaled center frequency. The scaled propagation loss is therefore $\alpha'=\alpha'(f')=p_{MAT}(f)\alpha_{TOPAS}(f/m) +\alpha_{CONF}(f)$. The material loss of TOPAS was found to increase quadratically with frequency in the range 0.2-2 THz, which means that α_{TOPAS} decreases with increasing m. Nevertheless the exact dependence of the ratio $\alpha/(m^2\alpha')$ on m is not easy to evaluate analytically, because it depends on the relative strength of the different terms in $m^2\alpha'$.

To get an idea of the dependence we neglect confinement loss and use the quadratic fit of Topas data to obtain $\alpha/(m^2\alpha')=[-0.13+0.63v+v^2]/[-0.13m^2+0.63mv+v^2]$, where v=f/(1 THz) is the frequency measured in THz. This approximation should in fact be a good approximation, except at very low frequencies, i.e. for large values of m. At for example 1 THz the ratio then becomes (1.17, 1, 0.91) when evaluated at m=(0.5, 1, 1.5), showing that the FOM is decreasing with m. In other words, couplers with smaller structures have a higher FOM.

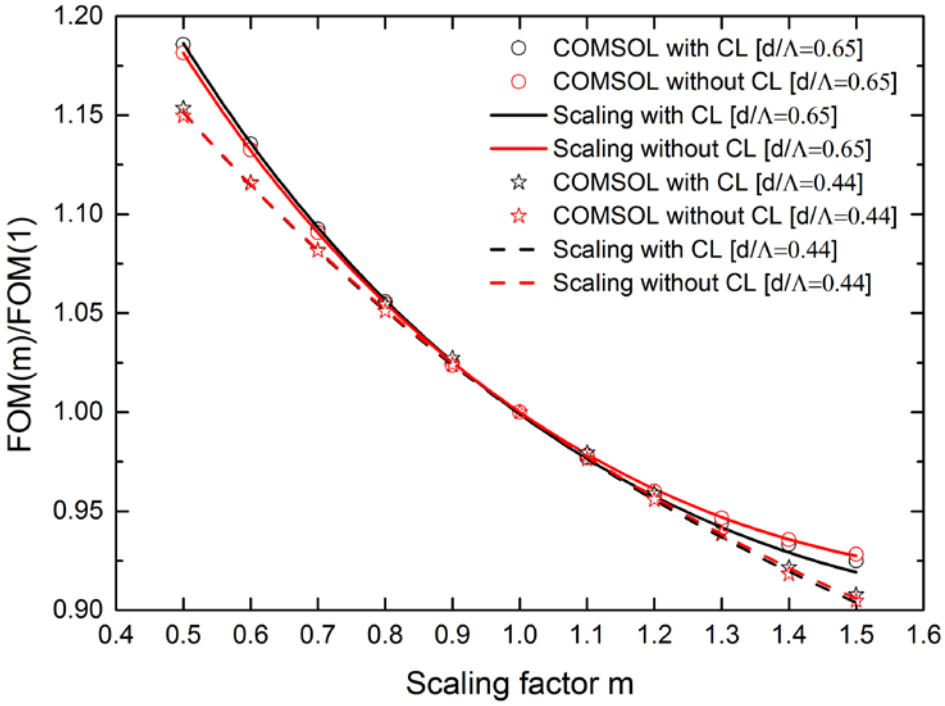

Figure 6.10 Ratio FOM(m)/FOM(1) versus scaling factor m for optimum coupler with Λ=682.5 μm and Λ_c = 102.375 μm (red curves in Fig. 6.9) and two different relative hole sizes d/Λ=0.44 and 0.65. Data represented by open circles and stars are calculated by using COMSOl, while data represented by solid and dashed lines are calculated based on the scaling method. Black color represents calculations taking into account the total device loss, while red color represents calculations where confinement loss has been neglected.

In Fig. 6.10 we evaluate the validity of the simple scaling expression for the FOM by plotting FOM(m)/FOM(1) calculated analytically using scaling from the m=1 solution with and without the assumption of neglecting the confinement loss, and calculated using COMSOL with and without confinement loss. We see that both for d/Λ=0.44 and 0.65 all 4 curves are nearly on top of each other, with only a slight deviation for the largest value of m=1.5, as anticipated. In both cases we have fixed Λ=682.5μm as in Fig. 6.8 and Fig. 6.9, and used the optimum core pitch Λ_c =102.375 μm found in Fig. 6.9 (red curves). The 4 curves have the same nice overlap for all considered values of d/Λ.

The confirmed validity of the scaling $FOM'=FOM\cdot[-0.13+0.63v+v^2]/[-0.13m^2+0.63mv+v^2]$, where v is the original center frequency for m=1, significantly expands the easily accessible space of design parameters. The optimum FOM is thus simply seen to be obtained still for d/Λ=0.65 and d_c/Λ_c =0.4350, but with the lowest allowable value of m. For the lowest value of m=0.5 we consider here the optimum FOM is 0.13. Because the bandwidth and center

frequency have doubled to B=0.3658 THz and 1.46 THz, respectively, whereas the device loss has increased to 12.22 dB. The optimum geometrical parameters with m=0.5 are Λ=341.25μm and Λ_c =51.1875 μm.

The scaling could also allow one to for example find m to fix the center frequency to 1 THz for all considered designs. The scaling properties are summarized in Fig. 6.11, from which we for example see that the optimum device with a center frequency of 1 THz is still the one with d/Λ=0.65, but for m=0.7308, which means that the structural parameters are Λ=498.7369 μm, Λ_c=74.8157 μm, and d_c=32.5426 μm, and the bandwidth and device loss are 0.2503 THz and 9.1737 dB, respectively.

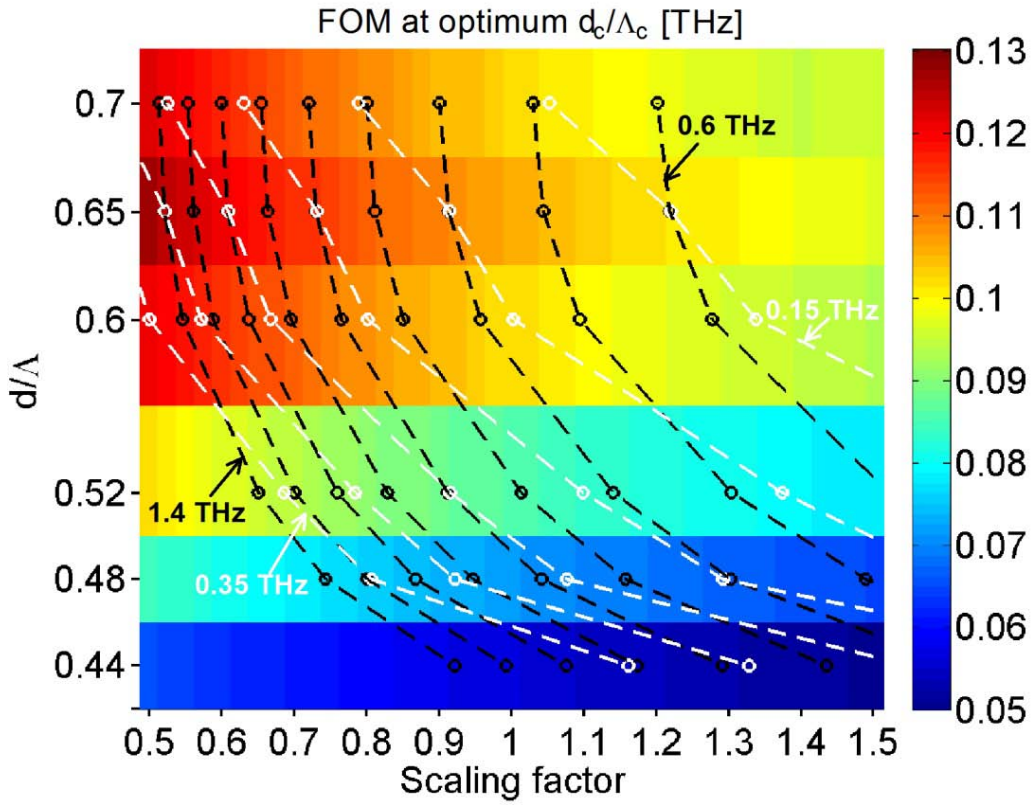

Figure 6.11 Optimum FOM versus d/Λ (Λ=682.5 μm and Λ_c=102.375 μm at m=1) and scaling factor m, calculated using the scaling method with confinement loss taken into account. Black dashed lines have fixed center frequency from 0.6 to 1.4 THz with a step of 0.1 THz. White dashed lines have fixed 3-dB bandwidth from 0.15 to 0.4 THz with a step of 0.05 THz (right to left).

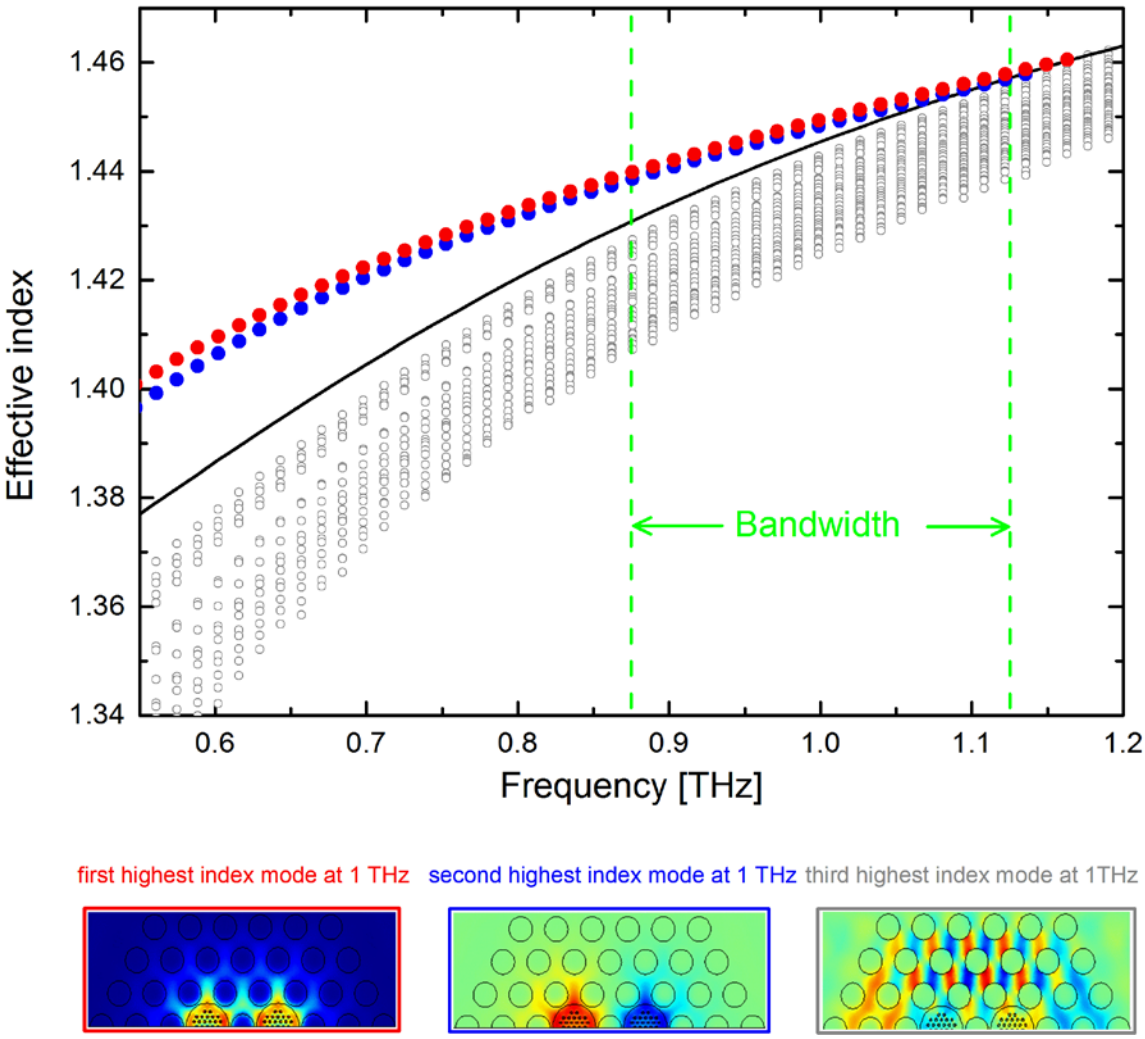

Figure 6.12 Red and blue dots and gray circles show the effective index of all calculated modes with a core power ratio larger than 2% (y polarization) for the optimum coupler with a center frequency of 1 THz, for which d/Λ=0.65, Λ=498.7369 µm, Λ_c=74.8105 µm, and d_c=32.5426. Red dots represent even superrmodes and blue dots represent odd supermodes. The solid black curve shows the index of the FSM. The three insets in the bottom show the electric field profiles at 1 THz (y polarization) of the first three highest effective index modes.

6.6 Single-mode guidance and robustness of optimum coupler operating at 1 THz

Single-mode guidance is an important feature for operation of a coupler. In order to check whether the optimum coupler with center frequency at 1 THz is working under single-mode guidance within the desired frequency region, we calculate all modes of the coupler (y polarization) that have a fraction of power in the two cores that is larger than 2%. The results are shown in Fig. 6.12. Red and blue dots and gray circles are all calculated modes

with more than 2% of power in the cores, the black curve is the FSM (found using the unit cell approach) and the region between two green dashed lines is the bandwidth. The three insets between two green lines show the electric field profiles at 1 THz (y polarization) of the first three highest effective index modes. It can be seen from the figure that there have only two guided modes with an effective index above the index of the FSM and these are the two fundamental supermodes (an even mode and an odd mode). This means that the optimum coupler is single-moded even though the cores in isolation would be multi-moded because d/Λ=0.65 is higher than the endlessly single-mode threshold 0.45.

Table 1. Performance of the coupler with optimum geometric structure parameters (d_c, Λ_c, d, Λ) with and without fabrication errors of ±1%

d_c (μm)	Λ_c (μm)	d_c (μm)	Λ_c (μm)	Cf (THz)	CL (cm)	DLoss (dB)	B (THz)
32.5426	74.8105	324.1790	498.7369	1	6.92	9.1737	0.2503
-1%	0	0	0	0.9606	7.21	8.8091	0.1412
+1%	0	0	0	0.9866	6.70	8.6667	0.2134
0	-1%	0	0	1.0066	6.93	9.3229	0.2446
0	+1%	0	0	0.9999	6.90	9.1513	0.2394
0	0	-1%	0	0.9729	6.44	8.1358	0.1714
0	0	+1%	0	0.9544	7.56	9.0823	0.1217
0	0	0	-1%	0.9539	7.23	8.6444	0.1225
0	0	0	+1%	0.9826	6.72	8.6818	0.1992

For an optimization as we have performed here it is important to investigate the robustness of the found optimum performance towards small deviation in the structural parameters from the optimum values. In Table 1 we therefore show the coupler performance when the optimum geometric structure parameters (d_c, Λ_c, d, Λ) are changed by ±1%. From the table, we see that the center frequency, coupling length and device loss of the optimum coupler are largely insensitive to fluctuations of the diameter and pitch of cladding (d and Λ) and core air-hole structure (d_c and Λ_c), respectively given that the resulting relative changes are less than 10%. The bandwidth of the coupler is also seen to be insensitive to changes in the core pitch Λ_c, but it is found to be very sensitive to fluctuations in (d_c, d, Λ) under which it can deviate by more than 50%.

6.7 Summary

In Summary, we have demonstrated a novel kind of broadband THz directional coupler that uses mechanical down-doping (or air down-doping) instead of chemical down-doping (fluorine doping) in the two cores. A thorough numerical design optimization has also been performed. In the optimization we have used an FOM, which takes both the 3-dB bandwidth and loss of the coupler into account. Our results show that the optimum parameters of the coupler are dependent on the desired center frequency. Simple scaling relations for the performance parameters have been used to expand the regime of optimization and fix the center frequency of the device to be 1 THz. For a center frequency of 1 THz, the coupler with Λ = 498.7369 µm, d = 324.1790, Λ_c= 74.8105 µm, d_c = 32.5426 µm is found to have the optimum performance with a bandwidth of 0.25 THz and a device loss of 9.1737 dB. We have demonstrated that this optimum coupler is single-moded and that its center frequency, device loss and coupling length are largely insensitive to ±1% fluctuations in all the structural parameters, whereas the bandwidth is very sensitive to ±1% changes in the three parameters (d_c, d, Λ), under which it can deviate by more than 50%.

7 Conclusion and outlook

The area of Terahertz (THz) radiation has been proved to be a very promising utility for a wide range of applications. However, since current THz systems predominantly utilize free-space propagation, the large size and requirement of careful alignment thus increasing the complexity are the drawbacks on using such systems. Consequently, it is in urgent need to develop waveguides/devices, similar with the fiber waveguides in infrared region, in THz region, which holds great promise for driving this technology further. In this thesis, we have investigated several different dielectric waveguides/devices that rely on different wave-guiding mechanism.

We first focus on Photonic bandgap gap (PBG) THz fibers. To overcome the fabrication problems of traditional PBG type fibers, which caused by the imbalance of hole dimensions, we investigate a novel porous-core honeycomb bandgap type THz fiber. The fabrication and experimental characterization of such a PBG THz fiber are also performed. The fiber is made of polymer TOPAS and confirm that it allows to fabricate long lengths of fiber with a near-perfect periodic structure and thus very clear bandgap guidance. The fundamental bandgap at 0.75-1.05 THz is found to have losses lower than 1.5 dB/cm, whereas the loss is below 1.0 dB/cm in the reduced bandgap 0.78-1.02 THz. The particular fiber we present has an outer diameter of 3.65 mm, and is thus already flexible. The outer diameter can be further reduced and thus these fibers may also be bent and cleaved.

We then focus on tube waveguides. Three different methods are used to improve the transmission bandwidth and dispersion properties, while the propagation loss can be kept generally low. The first way is to deliberately introduce high material absorption to the cladding material, thus efficiently removing the interfering fields that bounce through the cladding and back into the core in a traditional low-loss ARROW tube waveguide. The same effect has been obtained by adding a thin layer of a suitable absorber around the tube surface, here exemplified with water. We also designed and demonstrated another kind of tube waveguides consist of a uniform air-core and a cladding layer with tapered thickness. Results show that the same effect of the highly absorbing cladding material tube waveguides can also be obtained, thus breaking the cladding material limitation.

Finally, we investigate a special design of a broadband THz fiber directional coupler, which uses mechanical down-doping of the two cores. We show how the proposed coupler provides a broad bandwidth with relative low device loss and perform detailed optimizations of the coupler design to maximize bandwidth and minimize loss. Our simulations show that at 1THz a structure with suitable parameters can have a large bandwidth of 0.25 THz and relative low device loss of 9.2dB. Moreover, we verify that the optimum coupler is single-moded and we investigate the robustness of its performance to structural changes.

Future works could be:

(a) Numerical simulations in Chapter 6 indicate that the coupler can provides a broad bandwidth with relative low device loss. It is interesting to fabricate it and experimentally demonstrate the proposed broadband property of 3-dB coupler.
(b) In the Chapter 5, we present a new class of THz tube waveguides where we deliberately introduce a high absorbing cladding to achieve extremely broad bandwidth, low dispersion and generally low loss. It is interesting to check whether the high order modes can be suppressed due to the introduction of highly absorbing cladding, if this is a case, it can alleviate multimode problem of the tube waveguides.
(c) Non-linear THz fibers in THz region could be an interesting work. Very recently, the possibility to integrate Chalcogenide glass inside polymer PCF in visible regime has been demonstrated for the development of nonlinear fibers [153, 154]. Chalcogenide materials have been proved to have highly nonlinear property and at the same time with the generally low loss [155]. I believe that the same approach can be applied to THz region.

8 Bibliography

[1] B. T. King, M. S. Sherwin, B. E. Cole, J. B. Williams, and C. R. Stanley, "Coherent manipulation of semiconductor quantum bits with terahertz radiation," *Nature,* vol. 410, pp. 60-63, 2001.

[2] R. Huber, F. Tauser, A. Brodschelm, M. Bichler, G. Abstreiter, and A. Leitenstorfer, "How many-particle interactions develop after ultrafast excitation of an electron-hole plasma," *NATURE,* vol. 414, pp. 286-289, 2001.

[3] M. Walther, B. M. Fischer, and P. U. Jepsen, "Noncovalent intermolecular forces in polycrystalline and amorphous saccharides in the far infrared," *Chemical Physics,* vol. 288, pp. 261-268, 2003.

[4] M. Schall, M. Walther, and P. U. Jepsen, "Fundamental and second-order phonon processes in CdTe and ZnTe," *Physical Review B,* vol. 64, 2001.

[5] C. Ronne, L. Thrane, P. O. Astrand, A. Wallqvist, K. V. Mikkelsen, and S. R. Keiding, "Investigation of the temperature dependence of dielectric relaxation in liquid water by THz reflection spectroscopy and molecular dynamics simulation," *JOURNAL OF CHEMICAL PHYSICS,* vol. 107, pp. 5319-5331, 1997.

[6] S. E. Whitmire, D. Wolpert, A. G. Markelz, J. R. Hillebrecht, J. Galan, and R. R. Birge, "Protein flexibility and conformational state: A comparison of collective vibrational modes of wild-type and D96N bacteriorhodopsin," *BIOPHYSICAL JOURNAL,* vol. 85, pp. 1269-1277, 2003.

[7] D. Cooke, A. N. MacDonald, A. Hryciw, J. Wang, Q. Li, A. Meldrum*, et al.*, "Transient terahertz conductivity in photoexcited silicon nanocrystal films," *Physical Review B (condensed Matter and Materials Physics),* vol. 73, 2006.

[8] M. Schall and P. U. Jepsen, "Photoexcited GaAs surfaces studied by transient terahertz time-domain spectroscopy," *OPTICS LETTERS,* vol. 25, pp. 13-15, 2000.

[9] K. Iwaszczuk, D. G. Cooke, M. Fujiwara, H. Hashimoto, and P. U. Jepsen, "Simultaneous reference and differential waveform acquisition in time-resolved terahertz spectroscopy," *OPTICS EXPRESS,* vol. 17, pp. 21969-21976, 2009.

[10] C. A. Schmuttenmaer, "Exploring dynamics in the far-infrared with terahertz spectroscopy," *CHEMICAL REVIEWS,* vol. 104, pp. 1759-1779, 2004.

[11] K. I. Zaytsev, K. G. Kudrin, S. A. Koroleva, I. N. Fokina, S. I. Volodarskaya, E. V. Novitskaya*, et al.*, "Medical diagnostics using terahertz pulsed spectroscopy," *Journal of Physics: Conference Series,* vol. 486, 2014.

[12] A. P. Shkurinov, V. V. Tuchin, and M. M. Nazarov, "Tooth study by terahertz time-domain spectroscopy," *Progress in Biomedical Optics and Imaging - Proceedings of SPIE,* vol. 6791, 2008.

[13] A. J. Fitzgerald, R. J. Pye, J. Cluff, R. M. Woodward, V. P. Wallace, D. D. Arnone*, et al.*, "Terahertz pulsed imaging and spectroscopy for biomedical and pharmaceutical applications," *Faraday Discussions,* vol. 126, pp. 255-263, 2004.

[14] C. J. Strachan, T. Rades, D. A. Newnham, K. C. Gordon, M. Pepper, and P. F. Taday, "Using terahertz pulsed spectroscopy to study crystallinity of pharmaceutical materials," *CHEMICAL PHYSICS LETTERS,* vol. 390, pp. 20-24, 2004.

[15] J. F. Federici, B. Schulkin, and F. Huang, "THz imaging and sensing for security applications—explosives, weapons and drugs," *Semiconductor Science and Technology,* vol. 20, 2005.

[16] N. Krumbholz, T. Hochrein, N. Vieweg, T. Hasek, K. Kretschmer, M. Bastian*, et al.*, "Monitoring polymeric compounding processes inline with THz time-domain spectroscopy," *POLYMER TESTING,* vol. 28, pp. 30-35, 2009.

[17] N. Vieweg, N. Krumbholz, T. Hasek, R. Wilk, V. Bartels, C. Keseberg*, et al.*, "Fiber-coupled THz spectroscopy for monitoring polymeric compounding processes," *Proceedings of the SPIE - the International Society for Optical Engineering,* vol. 6616, 2007.

[18] K. Fukunaga, I. Hosako, Y. Ogawa, and S. Hayashi, "THz spectroscopy for art conservation science," pp. 678-679, 2007.

[19] T. Nagatsuma, T. Kurner, and D. M. Britz, "Special issue on THz communications," *Journal of Communications and Networks,* vol. 15, pp. 543-546, 2013.

[20] H.-J. Song and T. Nagatsuma, "Present and Future of Terahertz Communications," *IEEE TRANSACTIONS ON TERAHERTZ SCIENCE AND TECHNOLOGY,* vol. 1, pp. 256-263, 2011.

[21] R. W. McGowan, G. Gallot, and D. Grischkowsky, "Propagation of ultrawideband short pulses of terahertz radiation through submillimeter-diameter circular waveguides," *OPTICS LETTERS,* vol. 24, pp. 1431-1433, 1999.

[22] G. Gallot, S. P. Jamison, R. W. McGowan, and D. Grischkowsky, "Terahertz waveguides," *JOURNAL OF THE OPTICAL SOCIETY OF AMERICA B-OPTICAL PHYSICS,* vol. 17, pp. 851-863, 2000.

[23] Marcatili and Schmeltzer, "Hollow metallic and dielectric waveguides for long distance optical transmission and lasers," *Bell System Technical Journal,* vol. 43, pp. 1783-1809, 1964.

[24] T. Ito, Y. Matsuura, M. Miyagi, H. Minarnide, and H. Ito, "Flexible terahertz fiber optics with low bend-induced losses," *JOURNAL OF THE OPTICAL SOCIETY OF AMERICA B-OPTICAL PHYSICS,* vol. 24, pp. 1230-1235, 2007.

[25] J. A. Harrington, R. George, P. Pedersen, and E. Mueller, "Hollow polycarbonate waveguides with inner Cu coatings for delivery of terahertz radiation," *Optics Express,* vol. 12, 2004.

[26] J. A. Harrington, *Infrared fibers and their applications*: SPIE press Bellingham, 2004.

[27] B. Bowden, J. A. Harrington, and O. Mitrofanov, "Silver/polystyrene-coated hollow glass waveguides for the transmission of terahertz radiation," *OPTICS LETTERS,* vol. 32, pp. 2945-2947, 2007.

[28] X.-L. Tang, Y.-W. Shi, Y. Matsuura, K. Iwai, and M. Miyagi, "Transmission characteristics of terahertz hollow fiber with an absorptive dielectric inner-coating film," *OPTICS LETTERS,* vol. 34, pp. 2231-2233, 2009.

[29] Y. Matsuura and E. Takeda, "Hollow optical fibers loaded with an inner dielectric film for terahertz broadband spectroscopy," *JOURNAL OF THE OPTICAL SOCIETY OF AMERICA B-OPTICAL PHYSICS,* vol. 25, pp. 1949-1954, 2008.

[30] M. Navarro-Cia, C. M. Bledt, M. S. Vitiello, H. E. Beere, D. A. Ritchie, J. A. Harrington*, et al.*, "Modes in silver-iodide-lined hollow metallic waveguides mapped by terahertz near-field time-domain microscopy," *JOURNAL OF THE OPTICAL SOCIETY OF AMERICA B-OPTICAL PHYSICS,* vol. 30, pp. 127-135, 2013.

[31] O. Mitrofanov, R. James, F. A. Fernandez, T. K. Mavrogordatos, and J. A. Harrington, "Reducing Transmission Losses in Hollow THz Waveguides," *IEEE TRANSACTIONS ON TERAHERTZ SCIENCE AND TECHNOLOGY,* vol. 1, pp. 124-132, 2011.

[32] O. Mitrofanov and J. A. Harrington, "Dielectric-lined cylindrical metallic THz waveguides: mode structure and dispersion," *OPTICS EXPRESS,* vol. 18, pp. 1898-1903, 2010.

[33] B. Bowden, J. A. Harrington, and O. Mitrofanov, "Low-loss modes in hollow metallic terahertz waveguides with dielectric coatings," *APPLIED PHYSICS LETTERS,* vol. 93, 2008.

[34] B. Bowden, J. A. Harrington, and O. Mitrofanov, "Fabrication of terahertz hollow-glass metallic waveguides with inner dielectric coatings," *JOURNAL OF APPLIED PHYSICS,* vol. 104, 2008.

[35] R. Mendis and D. M. Mittleman, "Comparison of the lowest-order transverse-electric (TE1) and transverse-magnetic (TEM) modes of the parallel-plate waveguide for terahertz pulse applications," *OPTICS EXPRESS,* vol. 17, pp. 14839-14850, 2009.

[36] D. Grischkowsky and R. Menais, "THz interconnect with low-loss and low-group velocity dispersion," *IEEE Microwave and Wireless Components Letters,* vol. 11, pp. 444-446, 2001.

[37] D. Grischkowsky and R. Mendis, "Undistorted guided-wave propagation of subpicosecond terahertz pulses," *Optics Letters,* vol. 26, pp. 846-848, 2001.

[38] S. Coleman, D. Grischkowsky, and A. A. Sawchuk, "Parallel-plate THz transmitter," 2004.

[39] D. Grischkowsky, Y. Zhao, and A. Bingham, "THz parallel plate photonic waveguides," *Applied Physics Letters,* vol. 87, 2005.

[40] D. Grischkowsky and A. L. Bingham, "High Q, one-dimensional terahertz photonic waveguides," *Applied Physics Letters,* vol. 90, 2007.

[41] Z. P. Jian, J. Pearce, and D. M. Mittleman, "Two-dimensional photonic crystal slabs in parallel-plate metal waveguides studied with terahertz time-domain spectroscopy," *SEMICONDUCTOR SCIENCE AND TECHNOLOGY,* vol. 20, 2005.

[42] R. Mendis and D. M. Mittleman, "An ultra low loss THz waveguide," in *Conference on Lasers and Electro-Optics*, 2008, p. CPDA5.

[43] K. L. Wang and D. M. Mittleman, "Metal wires for terahertz wave guiding," *NATURE,* vol. 432, pp. 376-379, 2004.

[44] H. Cao and A. Nahata, "Coupling of terahertz pulses onto a single metal wire waveguide using milled grooves," *OPTICS EXPRESS,* vol. 13, pp. 7028-7034, 2005.

[45] Q. Cao and J. Jahns, "Azimuthally polarized surface plasmons as effective terahertz waveguides," *OPTICS EXPRESS,* vol. 13, pp. 511-518, 2005.

[46] M. Wachter, M. Nagel, and H. Kurz, "Frequency-dependent characterization of THz Sommerfeld wave propagation on single-wires," *OPTICS EXPRESS,* vol. 13, pp. 10815-10822, 2005.

[47] T.-I. Jeon, J. Zhang, and D. Grischkowsky, "THz Sommerfeld wave propagation on a single metal wire," *Applied Physics Letters,* vol. 86, 2005.

[48] J. A. Deibel, K. Wang, M. D. Escarra, and D. M. Mittleman, "Enhanced coupling of terahertz radiation to cylindrical wire waveguides," *Optics Express,* vol. 14, 2006.

[49] K. Wang and D. M. Mittleman, "Guided propagation of terahertz pulses on metal wires," *NATO Science for Peace and Security Series B: Physics and Biophysics,* pp. 55-68, 2007.

[50] H. Pahlevaninezhad, T. E. Darcie, and B. Heshmat, "Two-wire waveguide for terahertz," *OPTICS EXPRESS,* vol. 18, pp. 7415-7420, 2010.

[51] H. Pahlevaninezhad and T. E. Darcie, "Coupling of terahertz waves to a two-wire waveguide," *OPTICS EXPRESS,* vol. 18, pp. 22614-22624, 2010.

[52] P. Tannouri, M. Peccianti, P. L. Lavertu, F. Vidal, and R. Morandotti, "Quasi-TEM mode propagation in twin-wire THz waveguides," *CHINESE OPTICS LETTERS,* vol. 9, 2011.

[53] A. Markov and M. Skorobogatiy, "Two-wire terahertz fibers with porous dielectric support," *OPTICS EXPRESS,* vol. 21, pp. 12728-12743, 2013.

[54] N. Yudasari, J. Anthony, and R. Leonhardt, "Terahertz pulse propagation in 3D-printed waveguide with metal wires component," *Optics Express,* vol. 22, pp. 26042-26054, 2014.

[55] A. Markov, S. Gorgutsa, H. Qu, and M. Skorobogatiy, "Practical Metal-Wire THz Waveguides," 2012.

[56] A. Markov and M. Skorobogatiy, "Hybrid plasmonic terahertz fibers for sensing applications," *Applied Physics Letters,* vol. 103, 2013.

[57] J. Anthony, R. Leonhardt, and A. Argyros, "Hybrid hollow core fibers with embedded wires as THz waveguides," *OPTICS EXPRESS,* vol. 21, pp. 2903-2912, 2013.

[58] N. Yudasari, D. Vogt, J. Anthony, and R. Leonhardt, "Hollow Core Terahertz Waveguide Fabricated using a 3D Printer."

[59] M. Mbonye, R. Mendis, and D. M. Mittleman, "A terahertz two-wire waveguide with low bending loss," *APPLIED PHYSICS LETTERS,* vol. 95, 2009.

[60] A. Markov, H. Guerboukha, and M. Skorobogatiy, "Hybrid metal wire–dielectric terahertz waveguides: challenges and opportunities [Invited]," *JOSA B,* vol. 31, pp. 2587-2600, 2014.

[61] J. Anthony, R. Leonhardt, A. Argyros, and M. C. J. Large, "Characterization of a microstructured Zeonex terahertz fiber," *JOURNAL OF THE OPTICAL SOCIETY OF AMERICA B-OPTICAL PHYSICS,* vol. 28, pp. 1013-1018, 2011.

[62] K. Nielsen, H. K. Rasmussen, A. J. L. Adam, P. C. M. Planken, O. Bang, and P. U. Jepsen, "Bendable, low-loss Topas fibers for the terahertz frequency range," *Optics Express,* vol. 17, pp. 8592-8601, 2009.

[63] H. Han, H. Park, M. Cho, and J. Kim, "Terahertz pulse propagation in a plastic photonic crystal fiber," *APPLIED PHYSICS LETTERS,* vol. 80, pp. 2634-2636, 2002.

[64] M. Goto, A. Quema, H. Takahashi, S. Ono, and N. Sarukura, "Teflon Photonic Crystal Fiber as Terahertz Waveguide," *Japanese Journal of Applied Physics,* vol. 43, 2004.

[65] S. Li, H. Zhang, Y. Hou, J. Bai, W. Liu, and S. Chang, "Terahertz polarization splitter based on orthogonal microstructure dual-core photonic crystal fiber," *Applied optics,* vol. 52, pp. 3305-3310, 2013.

[66] K. Nielsen, H. K. Rasmussen, P. U. Jepsen, and O. Bang, "Broadband terahertz fiber directional coupler," *Optics letters,* vol. 35, pp. 2879-2881, 2010.

[67] H. Bao, K. Nielsen, H. K. Rasmussen, P. U. Jepsen, and O. Bang, "Design and optimization of mechanically down-doped terahertz fiber directional couplers," *Optics express,* vol. 22, pp. 9486-9497, 2014.

[68] L. J. Chen, H. W. Chen, T. F. Kao, J. Y. Lu, and C. K. Sun, "Low-loss subwavelength plastic fiber for terahertz waveguiding," *OPTICS LETTERS,* vol. 31, pp. 308-310, 2006.

[69] H.-W. Chen, Y.-T. Li, C.-L. Pan, J.-L. Kuo, J.-Y. Lu, L.-J. Chen*, et al.*, "Investigation on spectral loss characteristics of subwavelength terahertz fibers," *OPTICS LETTERS,* vol. 32, pp. 1017-1019, 2007.

[70] S. Jamison, R. McGowan, and D. Grischkowsky, "Single-mode waveguide propagation and reshaping of sub-ps terahertz pulses in sapphire fibers," *Applied Physics Letters,* vol. 76, pp. 1987-1989, 2000.

[71] R. Mendis and D. Grischkowsky, "Plastic ribbon THz waveguides," *Journal of Applied Physics,* vol. 88, pp. 4449-4451, 2000.

[72] A. Mazhorova, A. Markov, B. Ung, A. Ng, R. Chinnappan, M. Zourob*, et al.*, "Label-free bacteria detection using evanescent mode of a suspended core terahertz fiber," 2012.

[73] H.-W. Chen, C.-M. Chiu, C.-H. Lai, J.-L. Kuo, P.-J. Chiang, Y.-J. Hwang*, et al.*, "Subwavelength Dielectric-Fiber-Based THz Coupler," *JOURNAL OF LIGHTWAVE TECHNOLOGY,* vol. 27, pp. 1489-1495, 2009.

[74] J.-Y. Lu, C.-C. Kuo, C.-M. Chiu, H.-W. Chen, C.-L. Pan, and C.-K. Sun, "THz interferometric imaging using subwavelength plastic fiber based THz endoscopes," pp. 1-2, 2008.

[75] J.-Y. Lu, C.-M. Chiu, C.-C. Kuo, C.-H. Lai, H.-C. Chang, Y.-J. Hwang*, et al.*, "Terahertz scanning imaging with a subwavelength plastic fiber," *APPLIED PHYSICS LETTERS,* vol. 92, 2008.

[76] C.-M. Chiu, H.-W. Chen, Y.-R. Huang, Y.-J. Hwang, W.-J. Lee, H.-Y. Huang*, et al.*, "All-terahertz fiber-scanning near-field microscopy," *OPTICS LETTERS,* vol. 34, pp. 1084-1086, 2009.

[77] G. Yan, A. Markov, Y. Chinifooroshan, S. M. Tripathi, W. J. Bock, and M. Skorobogatiy, "Resonant THz sensor for paper quality monitoring using THz fiber Bragg gratings," *Optics letters,* vol. 38, pp. 2200-2202, 2013.

[78] S. F. Zhou, L. Reekie, H. P. Chan, Y. T. Chow, P. S. Chung, and K. Man Luk, "Characterization and modeling of Bragg gratings written in polymer fiber for use as filters in the THz region," *Optics express,* vol. 20, pp. 9564-9571, 2012.

[79] S. F. Zhou, L. Reekie, H. P. Chan, K. M. Luk, and Y. T. Chow, "Terahertz filter with tailored passband using multiple phase shifted fiber Bragg gratings," *Optics letters,* vol. 38, pp. 260-262, 2013.

[80] G. Yan, A. Markov, Y. Chinifooroshan, S. M. Tripathi, W. J. Bock, and M. Skorobogatiy, "Low-loss terahertz waveguide Bragg grating using a two-wire waveguide and a paper grating," *OPTICS LETTERS,* vol. 38, pp. 3089-3092, 2013.

[81] A. Hassani, A. Dupuis, and M. Skorobogatiy, "Porous polymer fibers for low-loss terahertz guiding," *OPTICS EXPRESS,* vol. 16, pp. 6340-6351, 2008.

[82] S. Atakaramians, A. Shahraam, B. M. Fischer, D. Abbott, and T. M. Monro, "Porous fibers: a novel approach to low loss THz waveguides," *OPTICS EXPRESS,* vol. 16, pp. 8845-8854, 2008.

[83] S. Atakaramians, S. Afshar V, B. M. Fischer, D. Abbott, and T. M. Monro, "Low loss, low dispersion and highly birefringent terahertz porous fibers," *OPTICS COMMUNICATIONS,* vol. 282, pp. 36-38, 2009.

[84] S. Atakaramians, S. Afshar V, H. Ebendorff-Heidepriem, M. Nagel, B. M. Fischer, D. Abbott*, et al.*, "THz porous fibers: design, fabrication and experimental characterization," *OPTICS EXPRESS,* vol. 17, pp. 14053-14062, 2009.

[85] S. Atakaramians, V. Afshar, M. Nagel, H. K. Rasmussen, O. Bang, T. M. Monro*, et al.*, "Direct probing of evanescent field for characterization of porous terahertz fibers," *Applied Physics Letters,* vol. 98, pp. 121104-121104-3, 2011.

[86] M. Skorobogatiy, A. Dupuis, and A. Hassani, "Low loss porous terahertz fibers containing multiple subwavelength holes," *Applied Physics Letters,* vol. 92, 2008.

[87] A. Dupuis, J.-F. Allard, D. Morris, K. Stoeffler, C. Dubois, and M. Skorobogatiy, "Fabrication and THz loss measurements of porous subwavelength fibers using a directional coupler method," *OPTICS EXPRESS,* vol. 17, pp. 8012-8028, 2009.

[88] M. Nagel, A. Marchewka, and H. Kurz, "Low-index discontinuity terahertz waveguides," *Optics Express,* vol. 14, 2006.

[89] M. Roze, B. Ung, A. Mazhorova, M. Walther, and M. Skorobogatiy, "Suspended core subwavelength fibers: towards practical designs for low-loss terahertz guidance," *OPTICS EXPRESS,* vol. 19, pp. 9127-9138, 2011.

[90] C. S. Ponseca, R. Pobre, E. Estacio, N. Sarukura, A. Argyros, M. C. J. Large*, et al.*, "Transmission of terahertz radiation using a microstructured polymer optical fiber," *OPTICS LETTERS,* vol. 33, pp. 902-904, 2008.

[91] J.-Y. Lu, C.-P. Yu, H.-C. Chang, H.-W. Chen, Y.-T. Li, C.-L. Pan*, et al.*, "Terahertz air-core microstructure fiber," *Applied Physics Letters,* vol. 92, 2008.

[92] Y. Geng, X. Tan, P. Wang, and J. Yao, "Transmission loss and dispersion in plastic terahertz photonic band-gap fibers," *Applied Physics B,* vol. 91, pp. 333-336, 2008.

[93] G. Ren, Y. Gong, P. Shum, X. Yu, and J. Hu, "Polarization Maintaining Air-Core Bandgap Fibers for Terahertz Wave Guiding," *IEEE JOURNAL OF QUANTUM ELECTRONICS,* vol. 45, pp. 506-513, 2009.

[94] Z. Wu, W. R. Ng, M. E. Gehm, and H. Xin, "Terahertz electromagnetic crystal waveguide fabricated by polymer jetting rapid prototyping," *OPTICS EXPRESS,* vol. 19, pp. 3962-3972, 2011.

[95] L. Vincetti, "HOLLOW CORE PHOTONIC BAND GAP FIBER FOR THz APPLICATIONS," *MICROWAVE AND OPTICAL TECHNOLOGY LETTERS,* vol. 51, pp. 1711-1714, 2009.

[96] A. Dupuis, K. Stoeffler, B. Ung, C. Dubois, and M. Skorobogatiy, "Transmission measurements of hollow-core THz Bragg fibers," *JOURNAL OF THE OPTICAL SOCIETY OF AMERICA B-OPTICAL PHYSICS,* vol. 28, pp. 896-907, 2011.

[97] B. Ung, A. Dupuis, K. Stoeffler, C. Dubois, and M. Skorobogatiy, "High-refractive-index composite materials for terahertz waveguides: trade-off between index contrast and absorption loss," *JOURNAL OF THE OPTICAL SOCIETY OF AMERICA B-OPTICAL PHYSICS,* vol. 28, pp. 917-921, 2011.

[98] M. Skorobogatiy and A. Dupuis, "Ferroelectric all-polymer hollow Bragg fibers for terahertz guidance," *APPLIED PHYSICS LETTERS,* vol. 90, 2007.

[99] R.-J. Yu, B. Zhang, Y.-Q. Zhang, C.-Q. Wu, Z.-G. Tian, and X.-Z. Bai, "Proposal for ultralow loss hollow-core plastic Bragg fiber with cobweb-structured cladding for terahertz waveguiding," *IEEE PHOTONICS TECHNOLOGY LETTERS,* vol. 19, pp. 910-912, 2007.

[100] K. Nielsen, H. K. Rasmussen, P. U. Jepsen, and O. Bang, "Porous-core honeycomb bandgap THz fiber," *Optics Letters,* vol. 36, pp. 666-668, 2011.

[101] B. Ung, A. Mazhorova, A. Dupuis, M. Roze, and M. Skorobogatiy, "Polymer microstructured optical fibers for terahertz wave guiding," *OPTICS EXPRESS,* vol. 19, pp. 848-861, 2011.

[102] L. Vincetti and V. Setti, "Waveguiding mechanism in tube lattice fibers," *OPTICS EXPRESS,* vol. 18, pp. 23133-23146, 2010.

[103] L. Vincetti, V. Setti, and M. Zoboli, "Terahertz Tube Lattice Fibers With Octagonal Symmetry," *IEEE PHOTONICS TECHNOLOGY LETTERS,* vol. 22, pp. 972-974, 2010.

[104] L. Vincetti, "Single-mode propagation in triangular tube lattice hollow-core terahertz fibers," *OPTICS COMMUNICATIONS,* vol. 283, pp. 979-984, 2010.

[105] M. Masruri, A. Cucinotta, S. Selleri, and L. Vincetti, "Circular Tube lattice fibers for terahertz applications," pp. 1-4, 2014.

[106] L. Vincetti and V. Setti, "Extra loss due to Fano resonances in inhibited coupling fibers based on a lattice of tubes," *OPTICS EXPRESS,* vol. 20, pp. 14350-14361, 2012.

[107] J. Anthony, R. Leonhardt, S. G. Leon-Saval, and A. Argyros, "THz propagation in kagome hollow-core microstructured fibers," *OPTICS EXPRESS,* vol. 19, pp. 18470-18478, 2011.

[108] C.-H. Lai, Y.-C. Hsueh, H.-W. Chen, Y.-j. Huang, H.-c. Chang, and C.-K. Sun, "Low-index terahertz pipe waveguides," *OPTICS LETTERS,* vol. 34, pp. 3457-3459, 2009.

[109] C.-H. Lai, B. You, J.-Y. Lu, T.-A. Liu, J.-L. Peng, C.-K. Sun*, et al.*, "Modal characteristics of antiresonant reflecting pipe waveguides for terahertz waveguiding," *OPTICS EXPRESS,* vol. 18, pp. 309-322, 2010.

[110] J.-T. Lu, Y.-C. Hsueh, Y.-R. Huang, Y.-J. Hwang, and C.-K. Sun, "Bending loss of terahertz pipe waveguides," *Optics express,* vol. 18, pp. 26332-26338, 2010.

[111] C.-H. Lai, T. Chang, and Y.-S. Yeh, "Characteristics of bent terahertz antiresonant reflecting pipe waveguides," *OPTICS EXPRESS,* vol. 22, pp. 8460-8472, 2014.

[112] E. Nguema, D. Ferachou, G. Humbert, J.-L. Auguste, and J.-M. Blondy, "Broadband terahertz transmission within the air channel of thin-wall pipe," *OPTICS LETTERS,* vol. 36, pp. 1782-1784, 2011.

[113] M. Miyagi and S. Nishida, "A proposal of low-loss leaky waveguide for submillimeter waves transmission," *IEEE Transactions on Microwave Theory and Techniques,* vol. MTT-28, pp. 398-401, 1980.

[114] B. You, J.-Y. Lu, C.-P. Yu, T.-A. Liu, and J.-L. Peng, "Terahertz refractive index sensors using dielectric pipe waveguides," *OPTICS EXPRESS,* vol. 20, pp. 5858-5866, 2012.

[115] J.-T. Lu, C.-H. Lai, T.-F. Tseng, H. Chen, Y.-F. Tsai, Y.-J. Hwang, *et al.*, "Terahertz pipe-waveguide-based directional couplers," *OPTICS EXPRESS,* vol. 19, pp. 26883-26890, 2011.

[116] A. Yariv, *Optical electronics in modern communications*: Oxford University Press, 1997.

[117] G. Agrawal, "Nonlinear Fiber Optics," *Nonlinear Fiber Optics,* 2012.

[118] E. Hecht, *Optics*: Addison Wesley, 2002.

[119] G. W. Barton, L. Poladian, M. A. Van Eijkelenborg, and M. C. J. Large, "Microstructured polymer optical fibres," *Microstructured Polymer Optical Fibres,* pp. 1-232, 2008.

[120] D. Auston, K. Cheung, and P. Smith, "Picosecond photoconducting Hertzian dipoles," *Applied Physics Letters,* vol. 45, pp. 284-286, 1984.

[121] Y. S. Lee, "Principles of terahertz science and technology," *Principles of Terahertz Science and Technology,* pp. 1-340, 2009.

[122] X. C. Zhang and J. Xu, "Introduction to THz wave photonics," *Introduction To THz Wave Photonics,* pp. 1-246, 2010.

[123] D. H. Auston, "PICOSECOND OPTOELECTRONIC SWITCHING AND GATING IN SILICON," *APPLIED PHYSICS LETTERS,* vol. 26, pp. 101-103, 1975.

[124] D. H. Auston, K. P. Cheung, and P. R. Smith, "PICOSECOND PHOTOCONDUCTING HERTZIAN DIPOLES," *APPLIED PHYSICS LETTERS,* vol. 45, pp. 284-286, 1984.

[125] D. H. Auston, K. P. Cheung, J. A. Valdmanis, and D. A. Kleinman, "CHERENKOV RADIATION FROM FEMTOSECOND OPTICAL PULSES IN ELECTRO-OPTIC MEDIA," *PHYSICAL REVIEW LETTERS,* vol. 53, pp. 1555-1558, 1984.

[126] P. R. Smith, D. H. Auston, and M. C. Nuss, "SUBPICOSECOND PHOTOCONDUCTING DIPOLE ANTENNAS," *IEEE JOURNAL OF QUANTUM ELECTRONICS,* vol. 24, pp. 255-260, 1988.

[127] C. Fattinger and D. Grischkowsky, "Point source terahertz optics," *Applied Physics Letters,* vol. 53, pp. 1480-1482, 1988.

[128] C. Fattinger and D. Grischkowsky, "TERAHERTZ BEAMS," *APPLIED PHYSICS LETTERS,* vol. 54, pp. 490-492, 1989.

[129] M. Vanexter, C. Fattinger, and D. Grischkowsky, "HIGH-BRIGHTNESS TERAHERTZ BEAMS CHARACTERIZED WITH AN ULTRAFAST DETECTOR," *APPLIED PHYSICS LETTERS,* vol. 55, pp. 337-339, 1989.

[130] M. Bertolotti, "Terahertz Spectroscopy: Principles and Applications, edited by S.L. Dexheimer," *Contemporary Physics,* vol. 51, 2010.

[131] P. C. Upadhya, W. Fan, A. Burnett, J. Cunningham, A. G. Davies, E. H. Linfield*, et al.*, "Excitation-density-dependent generation of broadband terahertz radiation in an asymmetrically excited photoconductive antenna," *OPTICS LETTERS,* vol. 32, pp. 2297-2299, 2007.

[132] P. U. Jepsen, R. H. Jacobsen, and S. R. Keiding, "Generation and detection of terahertz pulses from biased semiconductor antennas," *JOURNAL OF THE OPTICAL SOCIETY OF AMERICA B-OPTICAL PHYSICS,* vol. 13, pp. 2424-2436, 1996.

[133] D. Grischkowsky, S. Keiding, M. v. Exter, and C. Fattinger, "Far-infrared time-domain spectroscopy with terahertz beams of dielectrics and semiconductors," *JOSA B,* vol. 7, pp. 2006-2015, 1990.

[134] V. Lucarini, *Kramers-Kronig relations in optical materials research*: Springer, 2005.

[135] P. U. Jepsen, D. G. Cooke, and M. Koch, "Terahertz spectroscopy and imaging - Modern techniques and applications," *LASER and PHOTONICS REVIEWS,* vol. 5, pp. 124-166, 2011.

[136] H. Bao, K. Nielsen, H. K. Rasmussen, P. U. Jepsen, and O. Bang, "Fabrication and characterization of porous-core honeycomb bandgap THz fibers," *OPTICS EXPRESS,* vol. 20, pp. 29507-29517, 2012.

[137] J. Broeng, S. E. Barkou, A. Bjarklev, J. C. Knight, T. A. Birks, and P. S. Russell, "Highly increased photonic band gaps in silica/air structures," *OPTICS COMMUNICATIONS,* vol. 156, pp. 240-244, 1998.

[138] V. Setti, L. Vincetti, and A. Argyros, "Flexible tube lattice fibers for terahertz applications," *Optics express,* vol. 21, pp. 3388-3399, 2013.

[139] N. Litchinitser, A. Abeeluck, C. Headley, and B. Eggleton, "Antiresonant reflecting photonic crystal optical waveguides," *Optics letters,* vol. 27, pp. 1592-1594, 2002.

[140] M. Navarro-Cía, M. S. Vitiello, C. M. Bledt, J. E. Melzer, J. A. Harrington, and O. Mitrofanov, "Terahertz wave transmission in flexible polystyrene-lined hollow metallic waveguides for the 2.5-5 THz band," *Optics express,* vol. 21, pp. 23748-23755, 2013.

[141] U. Møller, D. G. Cooke, K. Tanaka, and P. U. Jepsen, "Terahertz reflection spectroscopy of Debye relaxation in polar liquids [Invited]," *JOSA B,* vol. 26, pp. A113-A125, 2009.

[142] S. F. Zhou, L. Reekie, H. P. Chan, Y. T. Chow, P. S. Chung, and K. M. Luk, "Characterization and modeling of Bragg gratings written in polymer fiber for use as filters in the THz region," *OPTICS EXPRESS,* vol. 20, 2012.

[143] C.-H. Lai, C.-K. Sun, and H.-C. Chang, "Terahertz antiresonant-reflecting-hollow-waveguide-based directional coupler operating at antiresonant frequencies," *OPTICS LETTERS,* vol. 36, pp. 3590-3592, 2011.

[144] C. Joerdens, K. L. Chee, I. A. I. Al-Naib, I. Pupeza, S. Peik, G. Wenke*, et al.*, "Dielectric Fibres for Low-Loss Transmission of Millimetre Waves and its Application in Couplers and Splitters," *JOURNAL OF INFRARED MILLIMETER AND TERAHERTZ WAVES,* vol. 31, pp. 214-220, 2010.

[145] N. M. Litchinitser, S. C. Dunn, B. Usner, B. J. Eggleton, T. P. White, R. C. McPhedran*, et al.*, "Resonances in microstructured optical waveguides," *OPTICS EXPRESS,* vol. 11, pp. 1243-1251, 2003.

[146] J. Laegsgaard, O. Bang, and A. Bjarklev, "Photonic crystal fiber design for broadband directional coupling," *OPTICS LETTERS,* vol. 29, pp. 2473-2475, 2004.

[147] J. Laegsgaard, "Directional coupling in twin-core photonic bandgap fibers," *OPTICS LETTERS,* vol. 30, pp. 3281-3283, 2005.

[148] Z. Wang, T. Taru, T. A. Birks, and J. C. Knight, "Coupling in dual-core photonic bandgap fibers: theory and experiment," *OPTICS EXPRESS,* vol. 15, pp. 4795-4803, 2007.

[149] T.-F. Tseng, C.-H. Lai, J.-T. Lu, Y.-F. Tsai, Y.-J. Hwang, and C.-K. Sun, "Investigation on Strong Coupling Behaviors of THz Subwavelength Directional Couplers," *IEEE PHOTONICS JOURNAL,* vol. 4, pp. 2307-2314, 2012.

[150] S. Zhang, X. Yu, Y. Zhang, P. Shum, Y. Zhang, L. Xia*, et al.*, "Theoretical Study of Dual-Core Photonic Crystal Fibers With Metal Wire," *IEEE PHOTONICS JOURNAL,* vol. 4, pp. 1178-1187, 2012.

[151] B. J. Mangan, J. C. Knight, T. A. Birks, J. Arriaga, and P. S. J. Russell, "Fundamental-mode cutoff in a photonic crystal fiber with a depressed-index core," *Optics Letters,* vol. 26, pp. 1469-1471, 2001.

[152] T. A. Birks, J. C. Knight, and P. S. Russell, "Endlessly single-mode photonic crystal fiber," *OPTICS LETTERS,* vol. 22, pp. 961-963, 1997.

[153] C. Markos, I. Kubat, and O. Bang, "Hybrid polymer photonic crystal fiber with integrated chalcogenide glass nanofilms," *Scientific reports,* vol. 4, 2014.

[154] H. Bao, C. Markos, K. Nielsen, H. K. Rasmussen, P. U. Jepsen, and O. Bang, "THz Waveguides, Devices and Hybrid Polymer-chalcogenide Photonic Crystal Fibers," *Proceedings of Piers 2014,* pp. 2047-2051, 2014.

[155] M. Zalkovskij, A. Strikwerda, K. Iwaszczuk, A. Popescu, D. Savastru, R. Malureanu*, et al.*, "Terahertz-induced Kerr effect in amorphous chalcogenide glasses," *Applied Physics Letters,* vol. 103, p. 221102, 2013.

List of publications

1. **Design and optimization of mechanically down-doped terahertz fiber directional couplers**

   H. Bao, K. Nielsen, H.K. Rasmussen, P.U. Jepsen, O. Bang,

   Optics Express 22(8), 9486-9497 (2014)

2. **Fabrication and characterization of porous-core honeycomb bandgap THz fibers**

   H. Bao, K. Nielsen, H.K. Rasmussen, P.U. Jepsen, O. Bang

   Optics Express 20(28), 29507–29517 (2012)

3. **Dielectric tube waveguides with absorptive cladding for broadband, low-dispersion and low loss THz guiding**

   H. Bao, K. Nielsen, O. Bang, P.U. Jepsen

   Scientific Reports (minor revision)

4. **THz waveguides, devices and hybrid polymer – chalcogenide photonic crystal fibers**

   H. Bao, C. Markos, K. Nielsen, H.K. Rasmussen, P.U. Jepsen, O. Bang

   Invited oral in Progress In Electromagnetics Research Symposium (PIERS 2014), 2014, Guangzhou, China

5. **Tube Waveguides With Low Loss, Low Dispersion, and High Bandwidth**

   H. Bao, K. Nielsen, O. Bang, P.U. Jepsen

   Oral presentation in Conference on Lasers and Electro-Optics 2014 (CLEO US 2014), 2014, San Jose, CA

6. **Design and Optimization of Air-Doped 3-dB Terahertz Fiber Directional Couplers**

   H. Bao, K. Nielsen, H.K. Rasmussen, P.U. Jepsen, O. Bang,

   Oral presentation in Conference on Lasers and Electro-Optics 2014 (CLEO US 2014), 2014, San Jose, CA

7. **Fabrication and characterization of porous-core honeycomb bandgap THz fibers**

   H. Bao, K. Nielsen, H.K. Rasmussen, P.U. Jepsen, O. Bang

Poster presentation in International Workshop on Optical Terahertz Science and Technologies (OTST 2013). 2013, Kyoto, Japan